IPP-Report

Max-Planck-Institut
für Plasmaphysik

Mathias Martin Dibon

Fast Valves for Massive Gas Injection in Tokamaks

IPP 2017-04
Oktober 2017

Technische Universität München
Fakultät für Maschinenwesen

Fast Valves for Massive Gas Injection in Tokamaks

M. Sc. Mathias Martin Dibon

Vollständiger Abdruck der von der Fakultät Maschinenwesen der Technischen Universität München zur Erlangung des akademischen Grades eines

Doktor-Ingenieurs (Dr.-Ing.)

genehmigten Dissertation.

Vorsitzender:	Prof. Dr.-Ing. Hartmut Spliethoff
Prüfer der Dissertation:	1. Prof. Dr. Rudolf Neu
	2. Prof. Dr. Rafael Macian-Juan

Die Dissertation wurde am 17.5.2017 bei der Technischen Universität München eingereicht und durch die Fakultät Maschinenwesen am 13.9.2017 angenommen.

ISBN 978-3-00-058025-3

Acknowledgements

First of all I would like to thank my supervisors **Dr. Gabriella Pautasso** and **Prof. Dr. Rudolf Neu** for the great effort they put into this project. Their insight into the topic, their patience and their ongoing assistance has been vital for the success of this project. Their input for my publications and this dissertation contributed greatly to my understanding of disruption mitigation. They always had fantastic advice when I encountered challenges and they ensured that I could focus on my project. Still they managed to introduce me at new projects having my future in fusion research in mind. For all this, I am very grateful.

A special thanks go to the pellet group of ASDEX Upgrade with **Dr. Peter Lang**, **Bernhard Plöckl**, **Michael Beck** and **Wolfgang Weisbart**. They raised me at the Max-Planck-Institute for Plasma physics since I came here as intern. They guided me as trainee and as master student and worked closely with me during this project. Dr. Peter Lang taught me the principles of scientific work, how to write quality papers and theses, create conference presentations and how to find my way in the world of research. Bernhard Plöckl in his role as lead engineer of the pellet group introduced me to a large variety of technical disciplines. He taught me everything about vacuum and cryogenic engineering, electrical engineering and control system development, as well as construction and safety guidelines. His input for the construction of test beds, the design of testing procedures and for the implementation of the valves in ASDEX Upgrade has been essential. Michael Beck, the lead technician of the pellet group, has done an outstanding job in building the

valves and test beds with me, as well as the gas handing system. His input during the design and testing phases was crucial and during the installation of the valves in ASDEX Upgrade he managed to keep us always ahead of schedule. I also appreciate his open ear and humor very much which helped me a lot during tough times. Wolfgang Weisbart helped immensely with his knowledge of electrical engineering and his excellent documentations of the previous system.

Further, I want to thank the responsible scientists of ASDEX Upgrade **Dr. Vitus Mertens** and **Dr. Albrecht Herrmann** for their understanding and thorough guidance during this project. They always had an open ear, extremely valuable advice and they introduced me to the procedures at IPP.

I also want to thank all the technicians in the workshops at IPP. They have taught me a great deal about manufacturing techniques and they also had fantastic suggestions for the design of the valves. The team in the electrical department also did an outstanding job for which I am very grateful. They managed to develop and build the entire control electronics for the MGI system within a very short time. This also contributed largely to the success of the project. The ASDEX Upgrade team helped me immensely during the installation into the vacuum vessel. Their input made it possible that all valves could be installed on time and are fully operational.

I also want to express my grate gratitude to **Franz Stelzer** who was in charge of programming the control system for the valves. Even in his busy schedule he managed to develop and implement the entire program. From him I was able to learn very much about programming and this will be very valuable in my future.

Furthermore, I want to thank **Prof. Dr. Rafael Macian-Juan** who guided me through my studies of nuclear engineering at TUM. He taught me everything I needed to know about the design of nuclear devices, backed me during my Master thesis and also took responsibility during this project. Finally, I want to thank **Prof. Dr. Antonino Cardella**. He was the first person to introduce me to fusion research in his course at TUM. His lectures motivated me to go into this field of research and it was thanks to him, that I got my first internship in the pellet group. For that, I am sincerely grateful.

Abstract

Disruptions are a major issue for todays Tokamak fusion devices. Plasma instabilities and technical errors can lead to large magnetohydrodynamic modes, resulting in a sudden loss of the plasma thermal energy. This causes large heat loads on the plasma facing components. Additionally, the decaying plasma current produces a changing magnetic flux which induces eddy currents in the plasma vessel. Vertically moving plasmas can generate a large halo current. These eddy and halo currents can give rise to tremendous Lorenz forces when crossed with the stationary magnetic field of the tokamak. Finally, the cooling plasma can generate strong electric fields which accelerate electrons up to relativistic energies. A concentrated beam of these electrons can erode plasma facing components if deconfined. All these disruptive effects, large heat loads, strong forces and highly energetic electrons can cause severe damage to the machine and have to be mitigated. Massive gas injection (MGI) has proven to be an effective tool to mitigate disruptive effects. A strong pulse of noble gas is released onto the plasma, radiating the power and thereby controlling heat loads, forces and highly energetic electrons. High speed gas valves are used to deliver this gas pulse.

This thesis describes the development of two types of high speed gas valves and their implementation into the ASDEX Upgrade vacuum vessel. Based on the experimental findings of previous disruption mitigation experiments and on the technical state of the art, a spring-driven and a piezo-driven in-vessel valve have been developed. These valves were designed to withstand the conditions inside a fusion device especially concerning high temperatures,

ultra-high vacuum, strong magnetic fields and ionizing radiation. The spring-driven valve holds a maximal gas inventory of $640\,\mathrm{Pa\,m^3}$, has an opening time of 2.7 ms and a peak mass flow rate of $1.1\,\frac{\mathrm{kg}}{\mathrm{s}}$. The piezo-driven valve has a maximal gas inventory of $210\,\mathrm{Pa\,m^3}$, an opening time of 3.5 ms and a peak mass flow rate of $0.7\,\frac{\mathrm{kg}}{\mathrm{s}}$. The valves were developed in 2015, two spring-driven valves and one piezo-driven valve were build and tested in 2016, installed into the vacuum vessel of ASDEX Upgrade in October 2016 and went into operation in March 2017.

The first technical test of the valves was performed using the in-vessel manometers and proved full operability of the three new valves. A measurement of the delay times of the valves revealed delays of 0.63 ms and 0.82 ms for the spring-driven valves and 9.2 ms for the piezo-driven valve. Radiation asymmetry during MGI can be significantly reduced when two toroidally separated valves inject gas with a time delay smaller than 0.1 ms from one another.

Contents

Abstract v

List of Figures xv

List of Tables xvii

List of Symbols xix

1 Introduction 1

1.1 Motivation 1

1.2 Nuclear Fusion 2

1.3 Disruptions 7

2 Physics of Disruptions 9

2.1 Disruption Causes 9

2.2 Evolution of disruptions 13

2.3 Consequences of disruptions 15

3 Disruption mitigation technologies 19

3.1 Disruption prediction 19

3.2 Disruption mitigation 21

3.2.1 Pellet injection 21

3.2.2 Liquid jets 22

3.2.3 Massive gas injection 24

4 Previous experimental results of MGI **27**
4.1 Mitigation of forces . . . 27
4.2 Mitigation of thermal loads . . . 29
4.3 Mitigation of Runaway electrons . . . 31
4.4 Impurity assimilation during MGI . . . 32

5 Requirements for the new valves **37**

6 The spring-driven valve **41**
6.1 Working principle . . . 42
6.2 Valve components . . . 43
6.2.1 Disc springs . . . 43
6.2.2 Bellows . . . 44
6.2.3 Valve stem . . . 45
6.2.4 PE actuators . . . 46
6.2.5 Valve seal . . . 47
6.2.6 Nozzle . . . 48
6.2.7 Position detection . . . 49
6.2.8 Clamping mechanism . . . 50
6.2.9 Valve assembly . . . 51

7 The piezoelectric valve **57**
7.1 Working principle . . . 58
7.2 Valve components . . . 58
7.2.1 Actuator . . . 59
7.2.2 Valve seal . . . 79
7.2.3 Bellow . . . 82
7.2.4 Nozzle . . . 82
7.2.5 Position detection . . . 83
7.2.6 Valve assembly . . . 84

8 Testing the valves **87**
8.1 Description of the test bed . . . 87
8.2 Valve tests . . . 92

8.2.1 Opening time and stroke 92
8.2.2 Outgassing 94
8.2.3 Leak rate 96
8.2.4 Reliability 97
8.2.5 Gas flow 98

9 Installation in ASDEX Upgrade 109
9.1 In-vessel setup 109
9.2 Shielding 111
9.3 Suspensions 113
9.4 Gas supply 117
9.5 Control system 119

10 Test results in ASDEX Upgrade 121
10.1 Technical tests 121
10.2 Delay time measurement 127
10.3 Toroidal radiation asymmetry 132

11 Summary and outlook 137

List of Requirements 151

S7 programs for the durability tests 155

Valve trigger circuits 161
.1 Manual operation circuit for spring-driven valves 161
.2 Circuit for automated control of spring-driven valves 162
.3 Manual operation circuit for piezo-driven valves 163
.4 Circuit for automated control of piezo-driven valves 164

Assembly for leak check of viton seal 167

Calculation procedure for jxB forces 169

Explosion prevention document of the MGI system 179

Signal plan for the new MGI valves **187**

List of Figures

1.1 Operation principle of a Tokamak 6

1.2 Measures for disruption mitigation 8

2.1 Development of plasma/halo current, magnetic field, thermal energy, power to the divertor, vertical position of the plasma and vertical force on the vessel during a disruption in ASDEX Upgrade (#13647) 13

3.1 Scheme of the liquid jet device 23

3.2 Scheme of the JET EM valve 25

4.1 Current quench time normalized by the plasma cross-section as function of the injected gas amount and gas type at ASDEX Upgrade 28

4.2 Radiative cooling power for different impurities 30

4.3 Comparison of Φ_{eff} for HFS (left) and LFS (right) injection over different amounts of injected atoms 34

6.1 Principle sketch of the spring-driven valve 42

6.2 Force F of a single disc and of the whole stack as function of the stroke s (left) and configuration of the disc spring stack (right) 44

6.3 Development of the friction force for a new ceramic at $F_N = 690N$ (a) and the maximal friction force F_{max} as a function of the normal force F_N 46
6.4 Geometry of the attachment for position detection 50
6.5 Assembled valve with colored sub-assemblies and numbered active components according to Fig. 6.1 52
6.6 Assembly of the rear cap 53
6.7 Assembly of the valve block 53
6.8 Assembly of the spring unit 54
6.9 3D model of the assembled spring-driven valve 55

7.1 Principle sketch of the piezoelectric valve 58
7.2 Operating principle of the amplifier frame 61
7.3 Geometry of the legs and active forces in the frame 63
7.4 Framework model of the actuator 64
7.5 Comparison between results of the analytic model and the FEM simulations 66
7.6 Stress distribution in the FEM model and representation by the distribution function 67
7.7 Results of the characterization of the test actuator 70
7.8 Movement of the test actuator compared with the analytical model 72
7.9 Results of tensile tests for a milled sample with $12\,\mathrm{mm}^2$ and a wire eroded sample with $16\,\mathrm{mm}^2$ 74
7.10 Image of a metallographic sample of wire eroded Ti Grade5 from the electron microscope 75
7.11 Analytic investigation for the maximal displacement and the maximal displacement time for different PE stack sizes and leg angles 76
7.12 Scan at which parameters the requirements for opening time and stroke are fulfilled 77
7.13 Results of the characterization of the valve actuator 79

7.14 Comparison of leak rate progressions for 3 different forces on the seal at different seal conditions 81

7.15 Switch for determining the open position of the valve: Valve is closed, switch is open (a), Valve is open, switch is closed (b) . . 83

7.16 Assembled valve with colored components and numbered active parts consistent with figure 7.1 84

7.17 3D model of the assembled piezo-driven valve 86

8.1 Scheme of the valve test bed vacuum system 88

8.2 Carrier flange with the piezo-driven MGI valve 89

8.3 Scheme of the gas supply system for the valve test bed 90

8.4 Heating curve of the small tank 91

8.5 Calibrated signals of the laser displacement sensor for the spring-driven valve (a) and piezo-driven valve (b) 93

8.6 Mass spectra of the background and with heated valves for the spring-driven valve (a) and the piezo-driven valve (b) 95

8.7 New viton seal with sharp sealing edge (a) and seal after 1000 operational cycles with worn out sealing edge (b) 98

8.8 2D axisymmetric models of the flow domain with gas reservoir (blue), straight nozzle (orange) and vacuum space (green) for the spring-driven valve (a) and the piezo-driven valve (b) . . . 99

8.9 Comparison between divergent, convergent and straight nozzle geometries with respect to peak gas velocity and peak mass flow rate 102

8.10 Comparison between the analytical model and the CFD simulation concerning mass flow rate and reservoir pressure for the spring-driven valve (a) and the piezo-driven valve (b) 103

8.11 Time evolution of the velocity profile along the axis of symmetry for the spring-driven valve (a) and the piezo-driven valve (b) 104

8.12 Colored image of the expansion cloud (spring-driven valve) 0.28 ms after the valve was triggered (a) and the intensity distribution at various distances from the nozzle exit (b) and colored image of the expansion cloud (piezo-driven valve) 1.1 ms after the valve was triggered (c) and the intensity distribution at various distances from the nozzle exit (d) 106

9.1 Toroidal locations of the MGI valves in ASDEX Upgrade . . . 110
9.2 Installed valves in the vacuum vessel a) spring-driven valve Se6 LFS with carbon tile, b) piezo-driven valve Se13 HFS behind the heat shield suspension, c) spring-driven valve Se4 HFS in an opening of the heat shield suspension 112
9.3 Simplified model of the valve for Lorenz force calculation . . . 113
9.4 FEM stress analysis with the calculated force during disruptions a) spring-driven valve Se6 LFS, b) piezo-driven valve Se13 HFS, c) spring-driven valve Se4 HFS 116
9.5 Scheme of the gas handling system for all in-vessel MGI valves in ASDEX Upgrade 117
9.6 WinCC interface of the MGI control system 120

10.1 Toroidal locations of the manometers, new spring-driven valves (green), piezo-driven valve (blue) and old spring-driven valves (violet) 123
10.2 Pressure measurements after trigger in shot 33752 124
10.3 Pressure measurements after trigger in shot 33764 125
10.4 Pressure measurements after trigger in shot 33765 126
10.5 Used lines of sight of the bolometers, new spring-driven valves (green), piezo-driven valve (blue) and old spring-driven valves (violet) 128
10.6 Calibrated bolometer signals Se5 LFS 7.2 s after trigger in shot 33806 128
10.7 Calibrated bolometer signals Se5 HFS 6.5 s after trigger in shot 33807 130

10.8 Calibrated bolometer signals Se13 HFS 7.0084 s after trigger in shot 33818 131
10.9 Calibrated bolometer signals Se13 LFS 7 s after trigger in shot 33819 132
10.10 Asymmetry factors for different delay times, used valves and disruptive phases 135

1 Scheme of the control circuit for manual operation of the spring-driven valves 162
2 Scheme of the control circuit for automated operation of the spring-driven valves 163
3 Scheme of the manual capacitor circuit used to charge PE stacks abruptly 164
4 Scheme of the automated capacitor circuit used to charge PE stacks abruptly 165

5 Cross-section of the assembly used for leak rate investigations of the viton seal 167

List of Tables

3.1 Comparison between MGI valves at current Tokamak experiments concerning Type, gas reservoir volume, opening time, orifice diameter, maximal reservoir pressure, tested gas species and distance between valve and plasma edge 26

9.1 Dimensions of the valves with their orientation fitted to the model and the resulting forces and torques due to eddy currents 115

10.1 Locations and calibration factors for each ionization manometer 124

10.2 Valve parameters for the radiation asymmetry experiments and the reference shot with valve Se6 133

List of Symbols

Greek symbols

α	Angle	[$^\circ$]
β	Plasma pressure ratio	[-]
γ	Adiabatic constant	[-]
γ^*	fraction of dissipated energy	[-]
Γ	Particle flux density	[$\frac{\#}{m^2 s}$]
δ	Angle	[$^\circ$]
η	Specific electrical resistivity	[Ωm]
θ	energy impact	[$\frac{GJ}{m^2 * s^{0.5}}$]
λ	Debye length	[m]
μ	magnetic permeability	[-]
κ	Plasma elongation	[-]
τ	Time constant	[-]
Φ	Fueling efficiency	[-]

Latin symbols

a	Dimension, minor plasma radius	[m]
aa	calibration factor	[-]
ab	calibration factor	[-]
ac	calibration factor	[-]
A	Cross-sectional area	[m^2]
ASF	Asymmetry factor	[-]

b	Dimension	[m]
bb	calibration factor	[-]
B	Magnetic flux density	[T]
c	Dimension	[m]
cc	calibration factor	[-]
d	Diameter, joint thickness	[m]
dd	calibration factor	[-]
dist	Distance	[m]
dm	Dampening coefficient	[$\frac{Ns}{m}$]
D	Spring rate	[$\frac{N}{mm}$]
ee	calibration factor	[-]
E	Electric field	[$\frac{V}{m}$]
E^*	Young's modulus	[$\frac{N}{mm^2}$]
f	Bulk thickness	[m]
ff	calibration factor	[-]
F	Force	[N]
g	Bulk length	[m]
h	Height	[m]
H	Specific radiated Power	[Wm^3]
i	Length of leg inclination	[m]
I	Current	[A]
k	Stiffness	[$\frac{N}{mm}$]
k^g	correction factor gas	[-]
l	Length, leg length	[m]
L	Inductance	[H]
m	Mass	[kg]
M	Torque	[Nm]
n	Particle density	[$\frac{1}{m^3}$]
N	Number of particles	[-]
p	Pressure	[Pa]
q	Safety factor	[-]
R	Plasma major radius	[m]
R^g	Gas constant	[$\frac{J}{kg*K}$]

R^*	Electrical resistivity	[Ω]
s	Stroke	[m]
S	conversion factor	[-]
t	Time	[s]
th	Thickness	[m]
T	Temperature	[K]
v	Velocity	[$\frac{m}{s}$]
Vol	Volume	[m^3]
W	Energy	[J]
x	Coordinate	[m]
y	Coordinate	[m]
z	Coordinate	[m]
Z	Charge number	[-]

Indices

0	Initial state
4	Segment 4
6	Segment 6
13	Segment 13
95	95% of normalized plasma radius
act	Actuator
B	Blocking value
c	Critical
D	Debye
e	Electron
eff	Effective
E	Energy
F	Frame
G	Greenwald
i	Inner
lim	Limit

L	Leg
max	Maximal value
n	Nozzle
N	Normal direction
o	Outer
p	Plasma
P	Piezo
q	Quadratic
r	Current loop
rad	Radiated
rel	Relativistic
s	Specific
stat	static
S	Spring
t	Toroidal
tot	Total
v	Value

Constants

c	Vacuum speed of light	$299 \times 10^6 \, \frac{\mathrm{m}}{\mathrm{s}}$
e	Electron charge	$1.6 \times 10^{-19} \, \mathrm{C}$
k_B	Boltzmann constant	$1.38 \times 10^{-23} \, \frac{\mathrm{J}}{\mathrm{K}}$
ϵ_0	Electric field constant	$8.85 \times 10^{-12} \, \frac{\mathrm{A\,s}}{\mathrm{V\,m}}$
μ_0	Magnetic field constant	$1.26 \times 10^{-6} \, \frac{\mathrm{N}}{\mathrm{A}^2}$

Chapter 1

Introduction

1.1 Motivation

The global energy demand has increased enormously in the past few decades and it is predicted, that this trend will at least continue [1]. With emerging markets, like Brazil or India and fast moving economies in China, North America and the European Union it is likely, that the overall energy consumption will increase dramatically [2] [3]. A rapid growth of the world's population and higher living standards contribute to this development [4]. With respect to the global climate change due to large CO_2 emissions [5], diminishing reserves of fossil fuels [6] and the growing social unacceptance of nuclear fission power plants, other possibilities have to be explored to satisfy the immense demand for energy.

Renewable energy sources like wind, hydroelectric solar power are discussed as solutions and systems to exploit these sources are already operated successfully. But regarding the global energy demand, they leave some problems unresolved. The unsteady energy output of wind [7] and solar power plants [8] pose great difficulties for highly industrialized economies, which rely on a steady supply with electricity. The same applies to the power supply infrastructure. The net frequency varies according to the variation of the power that is fed into the electric grid. In order to keep the net frequency constant

at 50 Hz, all power plants have to able to increase or decrease their energy output in a range of 2 % of their nominal capacity within 30 seconds [9]. Thus, solar and wind energy systems have to be operated together with conventional power plants. Another difficulty concerning solar and wind power is the large area they require to operate efficiently. Hydroelectric power plants on the other hand fulfill most of the demands, but they share a common problem with the other renewable energy systems, which is their restriction to certain locations. This calls for an expensive expansion of the infrastructure and new methods for a more efficient current transport. As for hydroelectric power, about 64 % of the available potential in Europe is already being exploited, making it increasingly difficult and expensive to expand it further [10]. Eventually, renewable energy sources are and will be an important part of the global energy mix. Still, centralized base load power plants are required.

1.2 Nuclear Fusion

One of the most promising options for base load power plants is nuclear fusion. This technology offers several advantages in comparison with conventional power plants and renewable energy systems. Fusion power plants have a high energy output with respect to the required area. This would allow the use of the existing infrastructure by replacing conventional plants. Fusion doesn't create greenhouse gases and the fuels are abundant. Finally, only short lived nuclear waste is produced, eliminating the need for long term storage capacities. Hence, research on nuclear fusion has been conducted for nearly sixty years now.

Nuclear fusion describes the process of combining two nuclei to form a heavier nucleus and to release some of the binding energies that the former nuclei contained. It has been found, that iron has the lowest binding energy per nucleon [11], therefore lighter elements have to be chosen to fuse. Another restriction is the coulomb force, that repels the two nuclei from each other [12]. This force is caused by the electric charges inside the nuclei and is proportional to the number of protons; therefore light ions are more likely to fuse at lower temperatures as the Coulomb force between them is small

compared to heavy ions. The fusion of the hydrogen isotopes deuterium (D_2) and tritium (T_2) is expected to be the most promising candidate for future power plants, because of its large fusion cross-section.

$$ {}^{2}_{1}\mathrm{D} + {}^{3}_{1}\mathrm{T} \longrightarrow {}^{4}_{2}\mathrm{He} + n + 17.6\ MeV \tag{1.1} $$

On earth, a significant amount of fusion power created from D-T fusion reactions has only been observed during the JET DTE1 campaign (16 MW) [13] and in TFTR (6.2 MW) [14]. Controlled fusion processes prove to be difficult to establish, due to the extremely high temperatures required. Significant amounts of D-T fusion reactions takes place above 10 keV which equals to about 116×10^6 K as the cross-section for fusion is high at these temperatures. However, since the cross-section for Coulomb interaction is also high, the plasma has to be confined to allow Coulomb interaction to occur until fusion takes place. Currently there are two major approaches to the problem, inertial and magnetic confinement. In the case of inertial confinement, fusion is achieved by pointing laser beams onto a target made of a frozen D-T mixture. The target is heated to fusion conditions on a very short time scale, leading to shock waves propagating inwards into the target. These waves compress the ice and the mixture starts to fuse [15] [16].

Magnetic confinement systems on the other hand heat gas by ohmic heating, microwaves or injection of highly energetic neutral particles until it reaches the temperature necessary for fusion. This plasma can be confined inside strong magnetic fields. The charged particles of the plasma gyrate around the magnetic field lines. In order to prevent end losses that would occur in a homogeneous magnetic field, the plasma is bent to form a ring. In a toroidal magnetic field however the field strength is highest near the central axis (magnetic high field side) and decreases in radial direction with 1/R towards the outboard side of the ring (magnetic low field side). This leads to a drift of the charged particles inside the plasma. The gradient of the magnetic field and its curvature cause a vertical charge separation, due to the so called grad. B drift and the curvature drift. The resulting electrical field leads to a charge independent particle drift (ExB-drift) perpendicular to both the E-field and

the B-field, hence towards the outboard side of the torus. To compensate for this drift motion, a secondary poloidal field has to be added to the toroidal field, generating helical field lines which spiral around the torus. Over the past decades of fusion research, two options for the creation of this poloidal field have been pursued. One is to generate the field by using an electric current in the plasma. For this purpose, a set of planar coils is inserted at the torus central axis, called the central solenoid. An alternating current in these coils generates a magnetic field, which induces a secondary current in the plasma. The plasma current itself generates a poloidal magnetic field which adds to the toroidal field generated by external field coils, forming the helical magnetic field. This setup is called a Tokamak (Fig. 1.1). The other approach is to generate the helical field by a set of external coils, which are placed around the ring. This is the so called Stellerator. Unlike Tokamak devices, stellerators have no toroidal symmetrical plasmas, hence far more parameters have to be optimized. In addition to that, the helical coils are challenging to manufacture, leading to higher costs. Due to this, the Tokamak is currently the more advanced system for magnetic confinement, although in principle it only allows pulsed operation and it is susceptible to plasma instabilities. New stellerator machines are being built, like the Wendelstein Stellerator W7-X for the purpose of risk mitigation and due to superior properties they possibly exhibit. In the following, this work will focus on Tokomaks, since disruptions don't occur in stellerator devices.

The Tokamak is currently the preferred principle for a nuclear fusion power plant as more experience is available with this machine. For this reason, several experimental devices are in operation all around the world to conduct research on high temperature plasmas, the most prominent being AUG[1], JET[2],

[1] "Axial Symmetric Divertor Experiment" in Garching, Germany. R=1.65 m, a = 0.5 m [17]

[2] "Joint European Torus" in Culham, England. Major radius R=2.96 m, minor radius a = 1.25 m [17]

DIII-D[3], TFTR[4], JT60-U[5], EAST[6] and KSTAR[7]. Since the energy transport in the plasma is dominated by diffusive processes, the temperature gradient is fixed for the given fusion temperature. Hence, larger machines are favorable to reduce the transport. Therefore the new experiment ITER[8] will be the largest magnetic confinement device. Predictions say, that ITER will generate a total of 500 MW of fusion power with 50 MW of external heating power, making it the first device to exceed the so called break-even point. In fact, ITER comes close to ignition conditions, which means that the energy of the alpha particles created in the fusion reaction would be sufficient to heat the plasma. The ignition conditions are fixed by the Lawson criterion [21]. This describes the lower boundary for the product of Temperature T, plasma density n and energy confinement time τ_E.

$$n * T * \tau_E > 3 * 10^{21} \ \frac{keV * s}{m^3} \tag{1.2}$$

The value on the right side is the minimum at which the fusion power sustains the fusion temperature. However, this criterion disregards losses due to Bremsstrahlung. For ITER it is foreseen to have plasma densities of about $1 \times 10^{20}\,\mathrm{m}^{-3}$, Temperatures of $150 \times 10^6\,\mathrm{K}$ which corresponds to roughly 12.9 keV and an energy confinement time of 3.75 s [22]. Thus, ITER could be able to reach ignition. Medium size Tokamaks, like ASDEX Upgrade (AUG), are too small to sustain fusion conditions without auxiliary heating. The research is focused mainly on the study of plasma effects, like turbulence, magneto hydrodynamic (MHD) instabilities and disruptions, as well as technical aspects, like the power exhaust schemes. ASDEX Upgrade went into operation in 1991 and has been working reliably ever since. Over the past 25 years, the device has been enhanced continuously. As of today it allows the creation of hydrogen, deuterium or helium plasmas with a temperature above 10 keV,

[3] Tokamak in San Diego, USA. R=1.67 m, a = 0.67 m [18]

[4] "Tokamak Fusion Test Reactor" in Princeton, USA. R=2.48 m, a = 0.85 m [17]

[5] "Japan Torus" in Naka, Japan. R=3.4 m, a = 1.1 m [17]

[6] "Experimental Advanced Superconducting Tokamak" in Hefei, China. R=1.7 m, a = 0.4 m [19]

[7] "Korea Superconducting Tokamak Advanced Research" in Daejeon, South Korea. R=1.8 m, a = 0.5 m [20]

[8] lat. for "The way", Cadarache, France. R=6.2 m, a = 2 m [17]

confined in magnetic fields of up to 3.9 T. The duration of a plasma pulse is limited to 10 s, due to the heat up of the field coils and the plasma facing components, as well as the energy stored in the flywheel generators. In the first phase of the pulse, the gas is heated by ohmic heating. This is achieved by ramping the current in the central solenoid, inducing a loop voltage in the torus, which leads to a break down ionizing the background gas. The heating power of the ohmic heating is about 1 MW. This is sufficient to ionize the gas completely, creating a highly conducting plasma. The plasma is further heated by injecting microwaves with the specific frequencies resonant to the gyrofrequencies of the electrons and ions. These are the so called Electron-Cyclotron Resonant Heating (ECRH) and Ion-Cyclotron Resonant Heating (ICRH) systems, with their respective heating powers of 4 MW and 6 MW. Another additional heating system is used, namely the Neutral Beam Injector (NBI) providing additional auxiliary heating power of 20 MW. This device injects neutral particles with high energy (60 - 100 keV) into the plasma. Collisions between the neutral particles and the ions transfer the energy into the plasma.

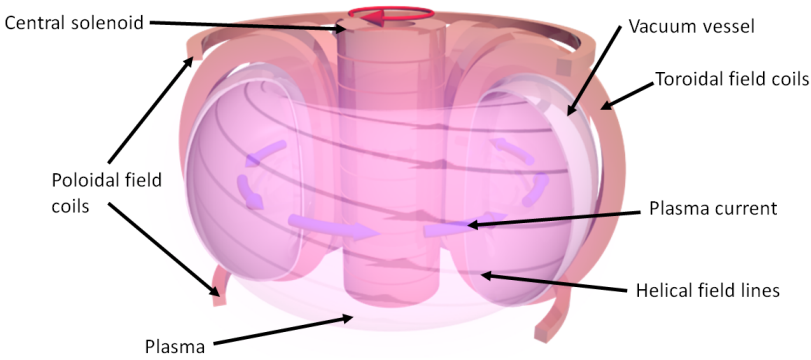

Figure 1.1: Operation principle of a Tokamak

1.3 Disruptions

A disruption is a terminal instability occurring in Tokamak plasmas that threatens the safety of the vessel. The causes for disruptions are manifold, such as a transgression of the operational limits or technical faults. These can cause large perturbations of the magnetic field topology (MHD modes) which increase energy transport in radial direction significantly, leading to a sudden loss of the plasma thermal energy. As a result, the plasma facing components are exposed to a tremendous heat flux (20 $\frac{\mathrm{MW}}{\mathrm{m}^2}$ in AUG [23], 150 $\frac{\mathrm{MW}}{\mathrm{m}^2}$ in JET [24]) which can cause severe damage. The plasma current, which is responsible for the poloidal field component of the magnetic containment field, decays due to the increased electric resistivity of the colder plasma. This leads to a rapid change of the poloidal magnetic field which in turn induces eddy currents in the vessel. Crossed with the stationary toroidal magnetic, these eddy currents generate huge Lorenz-forces (200 kN in AUG [25]) which can damage the vessel.

Furthermore, elongated plasmas are vertically unstable. During a disruption the vertical position can be perturbed beyond the region in which the control system can recover it and the plasma moves towards the upper or lower divertor. This incident is called a cold vertical displacement event (cold VDE) as the plasma has already lost most of its thermal energy. A VDE can also occur before the onset of a disruption as a consequence of MHD modes. This hot VDE can itself cause a disruption. Both cases, hot and cold VDEs, drive strong halo currents in the vessel which result in tremendous Lorenz-forces.

An additional hazard during disruptions is caused by so called "Runaway Electrons". These electrons can reach velocities close to the speed of light and are usually well confined. However, if the beam of these relativistic electrons suffers from MHD instabilities, the beam can lose confinement and hit the vessel wall. This deposits huge amounts of energy on plasma facing components, leading to severe damage of in-vessel components and the vacuum system.

Thus, a system for handling disruptions is vital for current plasma experiments and future fusion power plants that operate according to the Tokamak principle. As of today, a layered approach to disruption control is pursued (Fig. 1.2). The configuration control includes the supervision of the plasma

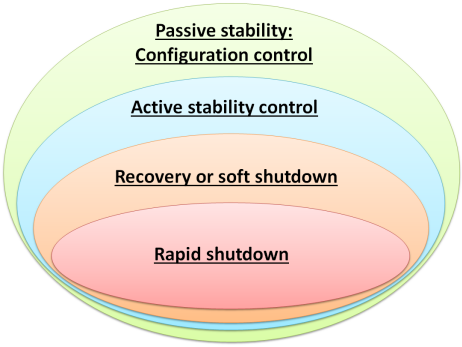

Figure 1.2: Measures for disruption mitigation

parameters before the initialization of the plasma discharge. This is meant to ensure, that the operating conditions are within the limits. In the case of experiments that are run close to the operational limits it is possible that small perturbations exceed these boundaries. To avoid resulting disruptions, active stability control systems like density, energy and current profile control bring the plasma back into a safe operating regime. If this is not possible and precursors indicate an upcoming disruption, an external current drive with ECRH can recover the discharge, allowing a soft shutdown. Should all previous measures fail, it is important to shut down the plasma discharge immediately and mitigate the consequences of the disruption before serious damage to the vessel can occur.

This rapid shutdown is performed by the injection of heavy impurities into the plasma. These impurities are generally noble gases like neon or argon that radiate the energy from the plasma due to collisions with the electrons and by that reduce heat loads to the divertor. The injection of the gas can either be achieved by pellet injection or by "Massive Gas Injection" (MGI) through high speed gas valves. The design, construction and testing of such valves are the objectives of this thesis.

Chapter 2

Physics of Disruptions

This chapter deals with the description of the phenomena that occur just before and during disruptions, based on experimental data. It further provides and analytical approach for the causes and consequences of disruptions. From this information it is possible to formulate the requirements for the gas valve.

2.1 Disruption Causes

In general, disruptions are caused by a rapid loss of thermal energy in the plasma. This leads to a sudden increase of the electrical resistivity of the plasma, causing a fast decay of the plasma current and therefore a loss of confinement. The rapid diminishing of the thermal energy or thermal quench (TQ) can be caused by different events. Extensive studies at the Tokamaks JET [26] and ASDEX-Upgrade [27] have shown, that many different factors may lead to disruptions. These can roughly be classified by physical and technical reasons. Physical causes for disruptions are mainly magneto hydrodynamic (MHD) instabilities, which occur, when the plasma is operated near certain limitations.
A well-known boundary is the low-q limit. The q-factor describes the helicity of the magnetic field lines and is often referred to as safety factor. In diverted plasmas, the edge-q is infinite, but the value at 95% of the minor radius has

proven to be a good approximation for the edge. Taking the elongation of the plasma into account, the q_{95} can be calculated.

$$q_{95} = \frac{2\pi a^2 B_t}{\mu_0 R I_p} * \frac{1+\kappa^2}{2} \tag{2.1}$$

Here, B_t is the toroidal magnetic flux, a and R are the minor and major radius of the plasma, I_p is the plasma current and κ is the elongation. A hard limit for this factor is derived from the ideal external kink mode[9] at $q_{95} = 2$. Another limitation is the upper boundary of the plasma density. The Greenwald limit [28] is derived from empirical values and is associated with increased radiation cooling at high densities. It scales with the inverse small radius square and the plasma current.

$$n_G = \frac{I_p}{\pi a^2} \tag{2.2}$$

This limit is especially important for the edge density, since pellet fueling experiments [29] have proven that the Greenwald density can be exceeded in the core plasma without causing MHD instabilities. Besides bremsstrahlung, line-radiation is the dominant form of radiation cooling. It is caused by not fully ionized light ions at the plasma edge and leads to extensive loss of thermal energy. If the irradiated power and the associated cooling of the plasma edge exceed the heating power it can result in a radiative collapse, which destabilizes MHD modes [26].

The lower density limit is reached, when external magnetic error fields can penetrate the plasma. These error fields perturb the main magnetic field from its axisymmetric shape and are mostly caused by misalignment of the magnetic field coils or components made from ferritic materials. Already small perturbations can slow down and stop rotating modes, leading to a locked mode.

Locked modes are typical precursors for disruptions. MHD modes can rotate with the plasma and are slowed down by error fields or eddy currents in the

[9] In case of small perturbations the strong helicity leads to a force imbalance and a kinking of the plasma

wall [30]. When the mode finally stops, the mode grows according to the resistivity of the vessel wall. Large locked modes have a very high thermal conductivity in radial direction and thus lead to a sudden loss of the plasma thermal energy, resulting in a disruption.

The plasma pressure is limited by the Troyon criterion [31] or the β-limit. The β-factor describes the ratio between the plasma kinetic pressure and the magnetic pressure.

$$\beta = \frac{nk_BT}{B^2/2\mu_0} \tag{2.3}$$

A high β is accompanied by a large local pressure gradient, favoring kink modes or ballooning modes[10]. The achievable β usually scales with the plasma current, the minor radius and the toroidal magnetic flux.

$$\beta < \beta_N \frac{I_p}{aB_t} \tag{2.4}$$

However, it has been shown, that peaked pressure profiles or certain current density profiles [32] [33] allow operation above this limit.

Multifaceted asymmetric radiation from the edge (MARFE) [34] is a poloidal asymmetric source of thermal radiation. The electron temperature can drop in the region of eV leading to a strong local temperature gradient and a fast loss of thermal energy. MARFE usually form close to the wall or the divertor, preferentially on the magnetic high field side or the X-point and are therefore most likely caused by plasma wall interaction. Neo-classical tearing modes (NTMs) [35] are another cause for disruptions in Tokamaks. These occur in H-mode[11] plasmas and are usually stable. In high β plasmas a pressure driven current (bootstrap current) exists. Magnetic islands flatten the pressure profile, reducing the bootstrap current and supporting the growth of the seed islands. Above a certain island width the mode destabilizes and grows. Larger islands have a high thermal conductivity in radial direction and lead to a rapid loss of the thermal energy.

Tokamaks usually operate with elongated plasmas due to better confinement

[10] Instability occurs when the plasma pressure is not compensated by the field line curvature (usually outboard side)

[11] Plasma state with high energy confinement due to an internal transport barrier

properties. But these shaped plasmas are intrinsically unstable to vertical movement, meaning in the direction of the torus symmetry axis. This calls for a fast feedback system to control the vertical position of the plasma, which is normally done by fast control coils. If the perturbation of the vertical position due to MHD modes is too large, the control system cannot recover the vertical stability and the displacement grows rapidly. This is called a vertical displacement event (VDE) [36]. VDEs cause immense forces on the vessel and the structures [37] due to halo currents, which can result in severe damage. They occur in most disruptions during the current decay (cold VDE), but they have been observed prior to the onset of disruptions (hot VDE).

The phenomena described above are just the most common physical causes for disruptions in Tokamaks. A complete list can be found in Ref.[26]. Besides the physical instabilities, there is a large variety of technical issues that make it difficult to operate Tokamaks close to the stability limits without the risk of disruptions.

Impurity seeding, which is usually used for edge plasma cooling and enhancing plasma performance, relies in a feedback control system. In case of incorrect density measurement, an increased impurity influx can lead to excessive radiation and a disruption. In rare cases, plasma shaping can fail which reduces the safety factor close to its limit. Fringe-jumps in the interferometry measurement responsible for the density control can influence the feedback system and cause increased gas puff, bringing the plasma to the upper or lower density limit. Problems with auxiliary heating systems may also cause disruptions as the NBI usually prevents modes from locking or adds heating power to avoid radiative collapse. Influx of high-Z material due to increased plasma material interaction can lead to increased radiation and large MHD modes. Finally, so-called unidentified flying objects (UFOs), meaning macroscopic parts from plasma facing components, parts from in-vessel diagnostics or even tiles from the heat shield may fall into the plasma, causing an immediate radiative collapse.

2.2 Evolution of disruptions

The mechanism of disruptions can be subdivided into three phases, namely the precursor phase, thermal quench (TQ) and current quench (CQ). During the precursor phase, small instabilities, mainly magnetic islands at the q=2 surface, develop. These islands rotate with the plasma fluid and are therefore detectable as oscillations in the magnetic field by the Mirnov-coils [38] (Fig. 2.1(b) [39]).

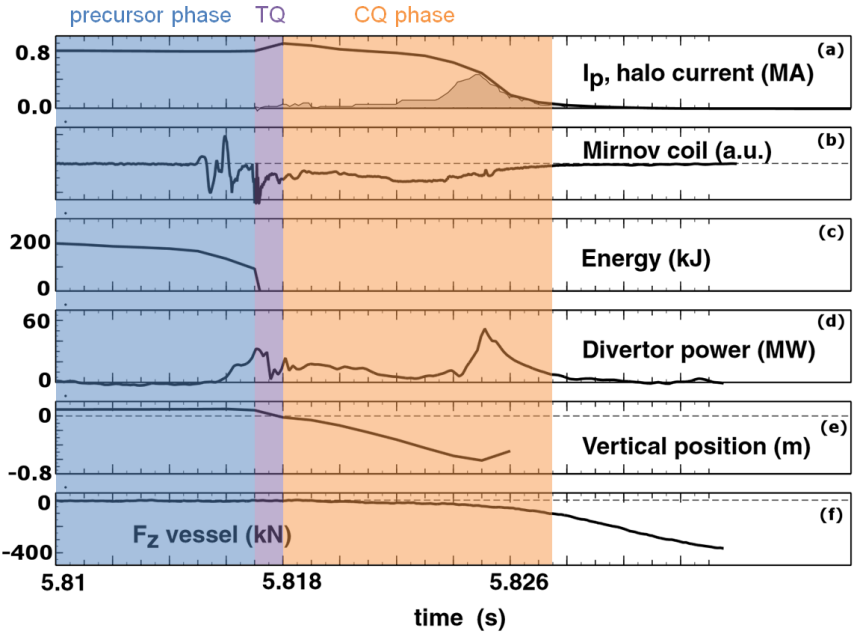

Figure 2.1: Development of plasma/halo current, magnetic field, thermal energy, power to the divertor, vertical position of the plasma and vertical force on the vessel during a disruption in ASDEX Upgrade (#13647)

Because the islands are a good indicator for an upcoming disruption they are called precursors. Another indicator for the existence of magnetic islands is the electron temperature profile, which is, in the case of ASDEX Upgrade, measured by the electron cyclotron emission diagnostic [40]. Due to the high heat conductivity across the islands, the temperature profile is almost flat over

this region. Usually, the timescale over which precursors develop accounts to several hundred milliseconds [41], but in some cases the precursor phase can be significantly shorter or can be completely absent [42]. The second phase (TQ) is characterized by a strong burst of thermal energy from the plasma to the vessel wall and especially the divertor. This occurs due to mode coupling and locking, leading to an excessive growth of the magnetic islands and the destruction of the magnetic topology. The timescale of the thermal quench is somewhere between 0.1 ms and several milliseconds (1 ms in AUG), depending on the size of the Tokamak and certain plasma parameters [43].
The loss of the plasma thermal energy (Fig. 2.1(c) [39]) during the TQ means the electron temperature drops to some eV. Because the plasma electrical resistivity is proportional to $T_e^{-3/2}$ it rises immensely, causing a decay of the plasma current (CQ). This decay can be described by a circuit equation. The plasma is viewed as a simple toroidal conductor with the self-inductance L and the electrical resistivity R^*.

$$\frac{dI}{dt} = \frac{1}{L} * (U - R^* * I) \tag{2.5}$$

$$L = \mu * R \underbrace{\left[ln\left(\frac{8 * R}{a * \sqrt{\kappa}}\right) - 2 + \frac{li}{2} \right]}_{\Gamma} = \mu R \Gamma \tag{2.6}$$

$$R^* = \frac{2\pi * R * \eta}{A} \tag{2.7}$$

μ being the magnetic permeability, R and a the plasmas major and minor radii, κ the elongation, η the specific electrical resistivity and A the cross section area. According to the Lenz rule, the decaying plasma current generates a loop voltage U to sustain the current.

$$U = (1 - \gamma^*) * L * \frac{dI}{dt} \tag{2.8}$$

The factor γ^* is the fraction of the dissipated magnetic energy in the plasma. The corrected self-inductance L^* is derived from this.

$$L^* = \gamma^* * L \tag{2.9}$$

The circuit equation (2.5) simplifies to a homogeneous linear differential equation, which is fulfilled by an exponential function with the time constant τ.

$$\frac{dI}{dt} * \frac{1}{I} = -\frac{R^*}{L^*} = -\frac{2\pi * \eta}{A * \gamma^* * \mu * \Gamma} = \frac{1}{\tau} \tag{2.10}$$

The specific electrical resistivity can be calculated according to Spitzer [44] from the effective charge Z_{eff} [45], the Coulomb logarithm [46] and the electron temperature.

$$\eta = \frac{\pi * e^2 * m_e^{1/2}}{(4\pi\epsilon_0)^2 * (1.5 * k_B)^{1.5}} * \frac{Z_{eff} * ln\Lambda}{T_e^{1.5}[eV]} = 5.27 * 10^{-5} * \frac{Z_{eff} * ln\Lambda}{T_e^{1.5}[eV]} \; (eV\Omega m) \tag{2.11}$$

$$Z_{eff} = \frac{\sum_j n_j j^2}{\sum_j n_j j} \tag{2.12}$$

$$ln\Lambda = ln\left(\frac{\lambda_D}{b_0}\right) = ln\left(\sqrt{\frac{\epsilon_0 k_B T_e}{n_e e^2}} * \frac{12\pi\epsilon_0 k_B T_e}{Z_{eff} e^2}\right) \tag{2.13}$$

Typically, a post-TQ plasma has an electron temperature of a few eV which correlates to an electrical resistivity around 0.7 mΩ [47]. With an inductance of about 6 µH [47], the current decay time constant is about 8.6 ms. Assuming that the current decay is effectively over when the plasma current has reached 20 % of its initial value, the current decay time is of the order of 14 ms.

2.3 Consequences of disruptions

As described before, disruptions occur within 10-15 ms. During this time, several phenomena arise which are directly linked to the disruptive process. Three of them are especially threatening to the plasma vessel and internal components.

- Massive heat loads on in-vessel components
- Strong forces on the vessel structure
- Electrons at relativistic speed (Runaway electrons)

The largest fraction of the plasmas thermal energy is lost during the thermal quench phase. Hence the thermal power that is distributed onto the components is huge and the energy diffuses into the material only to a depth which is proportional to $\sqrt{\Delta t}$. The resulting temperature increase is inversely proportional to the heat capacity and thermal conductivity of the materials and is characterized by the energy impact θ.

$$\Delta T \propto \theta = const. * \frac{\Delta W}{A_c * \sqrt{\Delta t}} \tag{2.14}$$

For tungsten and carbon, which are used in present day machines, the energy impact limit is of the order of $0.05\,\mathrm{GJ/m^2s^{1/2}}$. If the entire thermal power would be distributed onto the divertor, this limit would be exceeded [48] which would lead to deterioration of the components. Fortunately, a significant share of the power is radiated onto the vessel walls by impurities [49] and the scrape-off layer broadens during the thermal quench [50], increasing the effective area of the divertor on which the energy is deposited. In addition to that, the time in which the energy is distributed is prolonged due to the finite heat conductivity of the scrape-off layer. However, in large Tokamaks also a reasonable amount of thermal energy is delivered during the current quench by self-inductance of the plasma and ensuing ohmic heating. Overall high heat loads on small surface areas pose a problem for the operation of Tokamaks and have to be mitigated.

When the plasma current decreases during the current quench (5-10 ms [46]), the poloidal magnetic field changes and thus induces eddy currents in the vessel wall and the supporting structure. These currents not only heat the material by ohmic heating but they will also generate forces and moments when crossed with the toroidal magnetic field. When the vertical position of the plasma is perturbed during a disruption and the control system cannot bring it back to equilibrium (VDE) (Fig. 2.1(e) [39]), the plasma moves up or

down, touching the vessel walls and scraping off flux surfaces from the edge. This leads to a rapid shrinking of the cross-sectional area. Due to the toroidal flux conservation, a poloidal loop voltage is induced, driving an axially symmetric poloidal current from the plasma through the wall and back [51]. These halo currents can reach values of up to 50% of the original plasma current and thus cause enormous j × B-forces. Additionally, asymmetric halo currents are possibly produced by low edge-q, external kink modes are observed in most machines. This is especially dangerous for the machine, because of asymmetric stress. Further, the VDE generates Lorenz-forces acting on the plasma causing an acceleration of the plasma in direction of the perturbation and finally wall contact.

$$F_z = -2\pi I_p n_v B_z (z - z_0) \tag{2.15}$$

$$n_v = -\frac{R}{B_z}\frac{dB_z}{dR} \tag{2.16}$$

Forces due to halo currents can reach several 100 kN (Fig. 2.1(f) [39]) in medium size Tokamaks and reach values of over 3 MN in large machines like JET [52]. These tremendous forces can cause severe damage and thus have to be mitigated.

In plasmas, electrons are slowed down by friction, meaning coulomb collisions between the particles. With increasing electron speed, this friction decreases with $\frac{1}{v_e^2}$. Thus a critical electric field E_c exists above which the acceleration is no longer balanced by friction, resulting in the generation of relativistic electrons.

$$E_c(v_e) = \frac{e^3 n_e ln\Lambda}{4\pi\epsilon_0 m_e v_e^2} \tag{2.17}$$

In the case of a circular flight path of the electrons the acceleration is limited by the power loss due to synchrotron radiation as soon as the particles reach relativistic speed. For these electrons the critical E-field is $E_c(v_e \approx c) = E_{c,rel}$. While the internal field is below this critical field, there are no runaways. In fusion plasmas most electrons have thermal velocities, meaning if the internal field approaches the critical E-field for thermal velocities, a significant number of electrons will become runaways. For the so-called Dreicer-field all electrons

are assumed to become relativistic.

$$E_{c,Dreicer} = 0,43 E_c(v_{th}) \tag{2.18}$$

Because of the high resistivity during the current quench, strong internal electric fields are generated. Depending on the size of the Tokamak, these fields can reach sufficient values for the production of runaway electrons.

$$E_{internal} = \frac{\mu_0 l i I_p}{4\pi \Delta t_{CQ}} \tag{2.19}$$

A significant number of relativistic electrons has only been observed at low densities so far. But in large devices a secondary mechanism contributes to the generation. A seed current of runaway electrons can transfer parts of its kinetic energy to slower electrons by collisions. This can cause an exponential growth of the number of runaways.

$$\frac{1}{I_{RA}} \frac{dI_{RA}}{dt} \approx \frac{e * E_{c,rel}}{m_e * c * ln\Lambda} \left(\frac{E_{internal}}{E_{c,rel}} - 1 \right) = \frac{1}{\tau_{RA}} \tag{2.20}$$

If the internal field is larger than the critical field for the speed of light $E_{c,rel}$, an avalanche of runaway electrons is created. For a much larger ratio the amplification factor is $e^{\frac{\Delta t_{CQ}}{\tau_{RA}}}$. A beam of these runaway electrons deposits a huge amount of energy on a very small area if it hits material, comparable with electron beam welding. The runaway current can carry up to 50% of the plasma current and thus can generate a fast changing magnetic field when decaying. This induces eddy currents which themselves lead to thermal and mechanical stress on the vessel. Hence, runaway electrons are a significant threat to larger Tokamaks and have to be dealt with.

Chapter 3

Disruption mitigation technologies

In order to control the effects of disruptions, several systems for disruption detection and mitigation have been developed and operated at several experiments all over the world. In this chapter, the different approaches for disruption prediction that were tested in different Tokamaks, as well as impurity injection systems (pellet injection, liquid injection, gas injection) for disruption mitigation that were designed or operated at Tokamak machines are described.

3.1 Disruption prediction

The prediction of a developing disruption is of great importance, so the mitigation systems can be activated before damage to the machine can occur. Difficulties arise from the large variety of regimes run in current Tokamaks in order to achieve higher performance. For future Tokamak fusion reactors, the plasma conditions will be well defined and this drawback will be reduced greatly. But for the time being, detection systems must work reliably for a large set of plasma regimes.

The development of a reliable disruption predictor has been an important research topic on many Tokamak machines. Artificial neural networks are a possible solution that was investigated extensively. These neural networks evaluate different input signals to decide if a plasma is in a pre-disruptive state or not. Therefore they have to be trained to decide if a precursor leads to a disruption. Early experiments on TEXT [53] used the fluctuation data of the Mirnov coils as input signal. This allowed a prediction 1 ms in advance. Later research done on ADITYA [54] included signal from Mirnov coils, soft X-ray and line radiation measurements. This increased the prediction time to 8 ms. The model developed at DIII-D [55] used 33 plasma parameters to calculate the plasma β_N and compare it to the actual value. From the ratio of calculated and measured values, the disruption could be detected with a probability of 90 %. On JET [56], the neural net was trained using seven input parameters (locked mode, density, input power, radiated power, q_{95}, l_i, β_p and the derivative of the stored energy) and was trained with 360 plasma discharges. This network was able to predict disruptions with 90 % accuracy. The neural network developed at AUG [39] included eleven input signals (q_{95}, l_i, n_e/n_{GW}, radiated fraction of input power, normalized τ_e, MARFE signal, locked mode, β_N, dl_i/dt, $d\tau_e/dt$, $d\beta_N/dt$). This allowed predicting disruptions in 85 % of all tested cases.

A fuzzy logic system for disruption prediction was developed at JET [57]. This system maps a set of twelve scalar input signals (same signals as AUG neural network + plasma current) into a single scalar which is used to predict the disruption. The fuzzy logic system was able to predict 74 % of all disruptions about 400 ms prior to their onset.

Another system for disruption prediction uses classification and regression trees [58]. The algorithm proceeds through different steps. In each step one of the input signals is evaluated and the plasma is classified whether it is disruptive or not. The system achieves successful predictions in 95 % of all tested cases 40 ms before the disruption.

Current disruption prediction systems are based on statistical methods. Unlike the systems described before, these methods do not require machine learning but are rather based on physics laws and empirical findings. The system

currently used at AUG [59] divides disruptions into classes, namely vertical instability (VIDs), edge cooling (ECDs), impurity accumulation (IADs) and beta limit (BLDs) disruptions. For each class, a linear or quadratic discriminant function is created based on observations which are known for the respective class. The function is also used to determine the class of unknown observations. There are six input variables in the functions (ln l_i, ln n_e/n_{GW}, ln U_{loop}, ln P_{frac}, ln β_N, ln q_{95}) which have different impact depending whether linear or quadratic formulation is used. The success rate of the statistical method depends on the class of the detected disruption but are all about 90 % within 500 ms prior to the disruption.

3.2 Disruption mitigation

Several technical means to deliver impurities to the plasma have been developed and operated in the past. This section will give a short summary of different devices and their technical properties. Experimental results concerning the MGI valves are summarized in chapter 4.

3.2.1 Pellet injection

Disruption mitigation using pellets was performed at several Tokamaks. T-10 [60] used a gas gun to inject solid spherical C and KCl pellets with a diameter of 0.4 mm. The gun used helium at a pressure of 10 MPa to accelerated the pellets to a velocity of 150 $\frac{\mathrm{m}}{\mathrm{s}}$.

ASDEX Upgrade [61] used a modified gas gun to fire solid carbon pellets into the plasma. The pellets were accelerated by a helium pulse of up to 10 MPa. The magazine of the gun could hold a total of 90 carbon pellets of 0.2 mm to 0.7 mm diameter, hence delivering 1×10^{18} to 1×10^{20} atoms. An electric motor rotated the magazine until the pellet was in front of a fast gas valve. When the valve opened, the pulse accelerated the pellet, dragging it along the 1.2 m long gun barrel (inner diameter 0.85 mm) and shooting it into the 2.05 m long stainless steel guiding tube (inner diameter 5 mm) that led to the experiment. At the exit of the barrel, the pellet had reached its maximum

velocity of about 600 $\frac{\mathrm{m}}{\mathrm{s}}$. The propellant gas was removed in an expansion tank that was placed before the guiding tube entrance.

At JT-60U [62], disruption mitigation was performed using cryogenic neon pellets. The pellets are formed in housings inside the gun barrels. A total of 4 cylindrical pellets can be created simultaneously with 3 mm length and 3 mm diameter or 4 mm length and 4 mm diameter. Therefore, the barrels are cooled with liquid helium to a temperature of 6.5 K. The pellets are then accelerated by expanding hydrogen at a maximal pressure of 10 MPa and fly along the 0.8 m long barrel, through the guiding tube into the plasma. The pellet velocity was measured at 700 $\frac{\mathrm{m}}{\mathrm{s}}$. For disruption mitigation, the pellets were injected at a frequency of 5 Hz.

The current approach made by DIII-D [63] works with cryogenic neon pellets fired by a pipe gun. The pellet is created by freezing out neon gas in a cooled section of the gun barrel. The barrel has an inner diameter of 16.4 mm, hence defining the pellets outer diameter. The section of the barrel, where the pellet is created, is cooled by liquid helium and has a length of 16.4 mm. The pellet itself grows a bit longer than the cooled section and reaches a maximum length of 22 mm. This corresponds to 2×10^{20} atoms per pellet. When the pellet is fired, a fast electromagnetic valve is opened, releasing hydrogen gas at a pressure of 6.9 MPa into the gun barrel, pushing the pellet out of the cooled section and accelerating it by adiabatic expansion of the propellant gas. At the end of the gun barrel, the pellet has reached a velocity of 250 $\frac{\mathrm{m}}{\mathrm{s}}$. The pellet is then shattered on several target plates before reaching the plasma.

3.2.2 Liquid jets

The concept of liquid jets for the purpose of disruption mitigation was designed at DIII-D [64]. Liquids can penetrate deep into the plasma, have high cooling capabilities and can increase the plasma density by a factor of 30-100 times. The injector consists of two reservoirs which are connected by a moveable piston. The front reservoir is sealed off by a rupture disc. Before the Tokamak starts its operation, the smaller front reservoir is filled with liquid helium and set under pressure at 69 MPa. This is close to the burst pressure

of the rupture disc. The liquid has to remain cooled to about 9 K for the duration of the plasma discharge. While the front reservoir is filled with the liquid, the rear chamber is filled with pressurized helium at 7.7 MPa. The piston itself has a pressure intensification ratio of 9. Hence the piston is in force equilibrium. When the liquid jet is to be fired, a laser pulse of 0.5 ms and $10 \times 10^6 \frac{\mathrm{W}}{\mathrm{cm}^2}$ heats up the rupture disk to a temperature of 200 °C. The rupture disc is manufactured with grooves which serve as weak spots. At a temperature of 200 °C and under the pressure of the liquid, the mechanical stress limit of the rupture disc is exceeded and the groves cause failure initiation. The liquid expands through the converging-diverging nozzle and cools down by the Joule-Thomson effect. Additionally, the pressurized helium gas in the chamber drives the piston, pushing out the liquid. The volume of the propellant gas is much larger than the volume of the liquid which leads to quasi-static driving pressure on the piston during injection and therefore a constant stream of liquid. The nozzle is designed to produce a jet with a diameter of 1 mm and a velocity of 777 $\frac{\mathrm{m}}{\mathrm{s}}$. A scheme is shown in figure 3.1. The concept of liquid jet injection has advantages regarding penetration depth, cooling capabilities and delivered amount of impurities. But the high technical effort for cooling the liquid and replacing the rupture disk after every disruption have led to the decision to put this concept on hold and to pursue pellets and MGI.

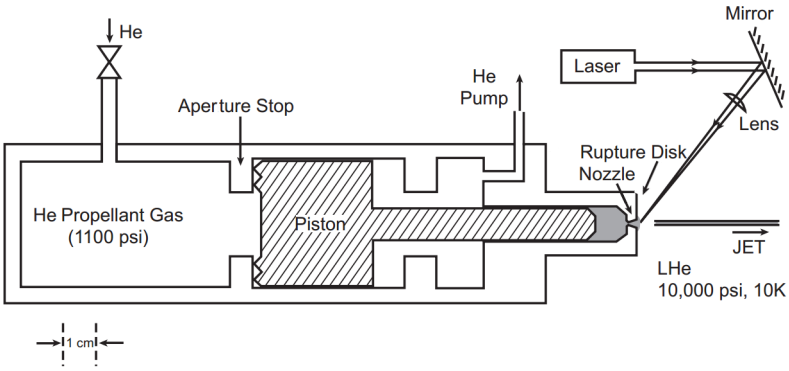

Figure 3.1: Scheme of the liquid jet device [64]

3.2.3 Massive gas injection

Massive gas injection (MGI) is the most widely investigated form of impurity delivery for disruption mitigation. All major Tokamak plasma experiments operate a MGI device. The most important technical specifications of a selection of valves are compiled here.

The majority of the MGI valves used on current Tokamaks are electromagnetic (EM) valves and work according to the same principle (Fig. 3.2). A mushroom shaped valve piston is pressed against the valve sealing either by spring force or by pressurized gas. The gas reservoir is then filled with the desired gas species. The valve is opened by a strong current of up to 1.5 kA, which is ramped up in a coil beneath the mushroom head. The varying magnetic field induces eddy currents in the mushroom head and the entire piston is accelerated away from the coil due to the jxB force. This opens the valve, releasing the gas from the reservoir. The opening time can be adjusted by the spring force, the gas pressure or the current. This type of valve has proven to work reliably due to its simple construction and working principle, but the main drawback is the necessary magnetic field. The valve must therefore be operated outside the Tokamaks magnetic field or with a shielding made of soft iron if operation in a magnetic field is mandatory. Hence, this type of valve is relatively large or the distance to the plasma edge results in a slow gas delivery. The high peak current also limits the time in which the valve can remain open, thereby limiting the gas throughput. Nevertheless, this type of valve is the most commonly used, with different reservoir volumes and operating pressures, according to the experiments needs.

The EM valve designed by Oak Ridge National Laboratory [65], which is used at DIII-D, has a slightly different working principle. A two-stage system is applied to allow high-throughput and high opening frequencies. The pilot valve is a standard EM valve with a small orifice and the main valve contains a pressure driven poppet and a large orifice. In the closed state, the poppet is pressed against the sealing by pressurized gas. Upon opening the pilot valve, the closing gas is vented downstream and the resulting pressure difference pushes the poppet back opening the main valve. This valve type has also

been operated successfully, but it still has the disadvantages of large size and long distance from the plasma.

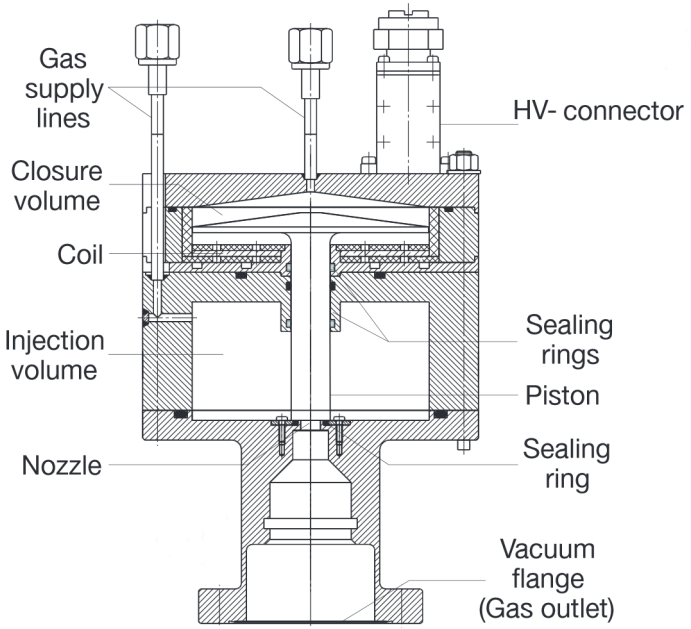

Figure 3.2: Scheme of the JET EM valve [66]

To overcome these problems ORNL introduced another concept based on a standard Inconel rupture disk (RD) [67]. A large gas reservoir is connected by a 1.4 m long thin tube to a small chamber which is sealed off by the rupture disk. A fast EM valve is placed along the tube. Before the plasma discharge is initiated, the reservoir is filled with 7 MPa of noble gas. When the gas is to be injected, the EM valve opens, releasing the gas to the rupture disk. The disk has a burst pressure of 5.4 MPa, hence it breaks open shortly after the gas arrives. The rupture disk can be placed very close to the plasma edge, because it is small compared to the EM valves and creates no magnetic fields. However, the variation of the opening time is of the order of 50 ms. Therefore it is very difficult to determine the exact time of the gas injection, making this valve only an option for large Tokamaks with long disruption time scales. The working principle of the spring-driven (SP) valves used at ASDEX Up-

grade goes as follows. In the first step, pressurized air pushes the piston with the valve plate against the sealing, closing the gas reservoir and tensing a stack of disk springs. Next, the reservoir is filled with the mitigation gas. The piston is then held in place by charging piezoelectric stack actuators, which expand and clamp down on the piston. The pressurized air is then vented and the valve is ready to be fired. When the gas should be released, the piezoelectric stacks are discharged within a few microseconds and the piston is accelerated back by the disk springs until it reaches its original position, thereby opening the valve. This working principle allows the valves to be placed very close to the plasma due to the absence of magnetic fields. This is favorable with respect to fueling efficiency (chapter 4.4) and arrival time of the gas at the plasma edge. Through further development, the size of the valves could be reduced so they can be mounted behind the heat shield on the magnetic high field side which protects the central column of the torus. However, the relatively complex construction of these valves affects their reliability.

	Type	m_{max} [Pam^3]	t_o [ms]	d_v [mm]	dist [mm]	Ref
Tore Supra	EM	100	1	22.5	1600	[68]
MAST	EM	195	2	10	1500	[69]
JET	EM	2340	2	10	4000	[66]
TEXTOR	EM	180	1	10	800	[70]
Al C-Mod	EM	2100	2	10	2000	[71]
DIII-D (1)	EM	3000	1	5	500	[72]
DIII-D (2)	EM	1050	2	22.3	-	[65]
DIII-D (3)	RD	362	50	20	50	[67]
AUG (1)	EM	54	2	12	1500	[73]
AUG (2)	SP	400	2	14	50	[46]
AUG (3)	SP	400	2	13	50	[46]

Table 3.1: Comparison between MGI valves at current Tokamak experiments concerning Type, gas reservoir volume, opening time, orifice diameter, maximal reservoir pressure, tested gas species and distance between valve and plasma edge

Chapter 4

Previous experimental results of MGI

Multiple studies concerning disruption mitigation using MGI were carried out over the past decade on many different Tokamak machines. These experiments were performed using different methods of material injection and varying plasma and machine parameters. This allows determining the requirements for future injection systems. The findings of the experiments are summarized shortly in this chapter.

4.1 Mitigation of forces

The mitigation of forces on the plasma vessel by massive gas injection has proven to work very successfully on all Tokamak machines. In the case of divertor Tokamaks, MGI is used to tune the current quench time by adjusting the amount of injected particles. Increasing the amount of injected gas reduces the current quench time until it reaches a lower limit. Beyond this limit it is assumed that ohmic heating of the plasma competes with the radiative cooling of the impurities. This limit is defined by the minimal current quench time Δt_{CQ}, meaning the time between the end of the thermal quench and the point when 80 % of the plasma current has decayed. This time is then

normalized by the plasma cross-sectional area to allow comparison between different plasma shapes and machines. At ASDEX Upgrade this limit was found at $\Delta t_{CQ} = 4 \frac{ms}{m^2}$ (Fig. 4.1), at DIII-D this limit is located at $\Delta t_{CQ} = 2.3 \frac{ms}{m^2}$ [74] and at JET it was found at $\Delta t_{CQ} = 1.7 \frac{ms}{m^2}$ [75]. The gas amounts necessary to reach these limits depend on the gas species and the Tokamak size. For medium size Tokamaks (AUG, DIII-D) 10^{22} particles are required, for large machines (JET) about 10^{23} particles are needed. However, spherical Tokamaks like MAST and NSTX show no significant reduction of Δt_{CQ} during MGI compared to unmitigated disruptions. At MAST, the limit for the current decay time was found at $\Delta t_{CQ} = 1.6 \frac{ms}{m^2}$ [76] which is close to the time scales of unmitigated disruptions. In Tore Supra it was discovered that MGI in a circular machine actually slows down the current quench up to 50 % compared to unmitigated disruptions. The Δt_{CQ} limit was found at $\Delta t_{CQ} = 5 \frac{ms}{m^2}$ [77]. A short current decay time is favorable with respect to the forces generated by halo currents. In this case, a significant share of the plasma current has decayed by the time a cold VDE occurs, thus reducing halo currents and EM forces. In JET, AUG and Alcator C-Mod [78], the halo currents were reduced by 50 %. However, a fast Δt_{CQ} leads to strong eddy currents which are induced in the structures due to the rapidly changing poloidal magnetic field. Thus, the current decay time has to be tuned to compromise between halo/eddy currents and to thereby reduce forces on the vessel as far as possible.

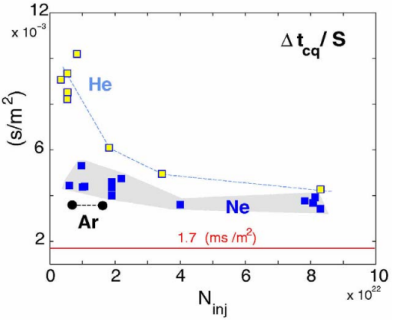

Figure 4.1: Current quench time normalized by the plasma cross-section as function of the injected gas amount and gas type at ASDEX Upgrade [79]

4.2 Mitigation of thermal loads

The heat flux on the divertor during disruptions poses a significant problem for divertor Tokamaks. Mitigation of the divertor heat flux by massive gas injection has therefore been investigated extensively and the results are promising. It has been found, that the largest fraction of the plasma thermal energy is irradiated during the pre-TQ and TQ phases, when using MGI. The duration of these phases depend mainly on the atomic mass of the injected gas and only slightly on the overall amount of injected impurity atoms. Mid-Z impurities shorten the cooling time more than pure helium or deuterium. Hence, the dominant mechanism is the radiative energy loss per impurity ion. The correlation between the irradiated power and the number of injected impurity particles can be described, utilizing the radiation curves in figure 4.2.

$$P_{rad} = \frac{W_{th}}{\Delta t_{pre-TQ} + \Delta t_{TQ}} = N_e * N_{inj} * H_z \tag{4.1}$$

For a standard H-mode plasma, the thermal energy W_{th} can reach up to 5 MJ in large Tokamaks like JET. The pre-thermal quench time Δt_{pre-TQ} is several milliseconds and the thermal quench time Δt_{TQ} is about 1 millisecond. The electron density N_e is usually of the order of $1 \times 10^{20}\,\mathrm{m}^{-3}$. At a disruptive plasma temperature of about 10 eV, the radiative loss parameter H_z is approximately $1 \times 10^{-32}\,\mathrm{W\,m}^3$. Hence, the number of injected impurity atoms N_{inj} amounts to 7.67×10^{22} which corresponds to $318\,\mathrm{Pa\,m}^3$. It has to be stated here that the actual impurity density in the plasma is dominated by the impurity assimilation as described in section 4.4. Experiments have proven, that significantly lower amounts than calculated are sufficient to mitigate thermal loads. In the case of AUG more than 60 % of the plasma thermal energy before gas injection are radiated by injecting 0.5×10^{22} particles of helium [80].

Injecting similar amounts of mid-Z impurities like Ar, Ne, or Kr has shown to radiate around 100 % of the plasma thermal energy during the cooling time Δt_{cool}. This has been observed at JET [75], DIII-D [81] and AUG [80] among others. The cooling time is generally defined as the time between the arrival

of the gas at the plasma edge and the onset of the thermal quench. In some cases the time of flight of the gas is also included.

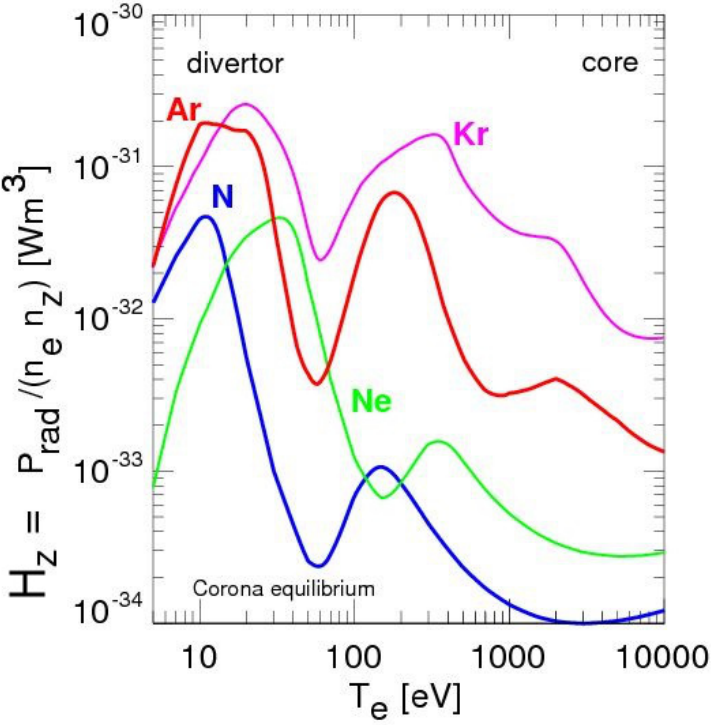

Figure 4.2: Radiative cooling power for different impurities [82]

It was also observed, that the cooling time cannot be reduced below a certain limit, even when using massive amounts of mid-Z impurities. Pre-thermal and thermal quench times are assumed to depend on the propagation of the cold front, resulting from the gas, into the plasma. Current models show an edge density build up during MGI that slows down the propagation of the cold front. Hence, injecting more gas cannot reduce the cooling time. Cooling times have been found to be $\Delta t_{cool} = 1\,ms$ at AUG [79] and DIII-D [74], $\Delta t_{cool} = 4\,ms$ at Tore Supra [77], $\Delta t_{cool} = 2\,ms$ at MAST [76] and $\Delta t_{cool} = 4\,ms$ at JET [75]. These cooling times were achieved by injecting 0.5×10^{22} particles of different noble gases into the plasma.

Radiative cooling works very effectively in reducing the heat flux on the divertor. In the very first moments of the injection though, the radiation is very localized around the injection port [83]. This is an issue for the injection of large amounts of mid-Z impurities and for the use of in-vessel valves, since the radiation in these cases is very localized and therefore the thermal power is deposited on a small area. Besides the valve location and the gas species/amount, the first wall materials also play an important role. In full metal machines, the largest share of radiative losses during mitigated disruptions is caused by the injected impurity atoms, while in carbon machines up to 50 % is caused by sputtered carbon atoms [74].

4.3 Mitigation of Runaway electrons

The mitigation of runaway electrons is still one of the unresolved issues concerning the safe operation of Tokamaks. As of today it is not possible to reach the necessary electron density during the current quench in order to suppress the runaway generation. To prevent the primary generation of runaways one has to keep the internal electric field during the current quench below the critical electric field for relativistic electrons. This condition gives a relation for the necessary electron density, the so called Rosenbluth density n_{RB}.

$$n_{RB} = \frac{m_e l_i I_p}{e^3 \mu_0 c^2 ln\Lambda \Delta t_{CQ}} \tag{4.2}$$

For an H-mode plasma in ASDEX Upgrade ($l_i = 0.8$, $I_p = 1.2$ MA, $ln\Lambda = 17$, $\Delta t_{CQ} = 10$ ms) the Rosenbluth density is $n_{RB} = 1.11{*}10^{22}$ m^{-3}. Considering a plasma volume of 13 m^3, a total of 1.44×10^{23} electrons would have to be injected. The mitigation gas is singly ionized and the bound electrons have half the scattering cross-section compared to free electrons. Therefore, every neon atom could provide 5.5 electrons and every argon atom 9.5 electrons. This would account for 2.62×10^{22} or 108 Pa m^3 of neon respectively 1.52×10^{22} or 63 Pa m^3 of argon. The Rosenbluth density is several magnitudes higher than the standard plasma density and currently not achievable. However, injection of mid-Z material into an existing RE beam after the CQ is very efficient in

suppressing the REs, since the Rosenbluth density is much smaller. Additionally, the Rosenbluth theory does not take the ions into account. Although they do not slow down the runaway electrons, they do disperse the electron beam by scattering. The cross-section of the ions with respect to scattering is relatively high compared to the electron-electron scattering. This effect is currently based on observation as no clear theory has been worked out. As for the gas itself, it has been found that low amounts of pure argon (2×10^{21} particles [84]) are a strong driver for the generation of REs, due to its large cooling capabilities. Injection of massive impurity pellets has also proven generate REs effectively. In the case of pellet injection the runaway current can build up to a significant share of the original plasma current [85], whereas for MGI only 10 % of the plasma current was observed as RE current in DIII-D [74] and 30 % in TEXTOR [86], but 50 % in AUG [87] and up to 60 % in JET [88]. This behavior could originate in the deposition profile of the impurities. While pellet injection delivers most of the impurities to the plasma core, MGI mainly fuels the plasma edge. Increasing the amount of argon injected into the RE beam has shown a noticeable reduction of the RE current decay time at AUG [84]. At 10^{22} injected particles the RE current decay time has dropped to 3 ms. The critical electric field becomes larger when more argon is puffed. Once this critical electric field exceeds the toroidal electric field, the REs lose energy. Experiments performed at Tore Supra with helium and a mixture of helium and argon showed a noticeable reduction of the RE current, independent of the injected amount of gas [77].

4.4 Impurity assimilation during MGI

The mitigation of disruptions is performed successfully by the injection of massive amounts of material into the plasma, as proven by many experiments. These mid-Z impurities have to be assimilated efficiently into the plasma in order to fulfill their task and to prevent unnecessary loads onto the Tokamaks pumping system. Gas injection is currently the most widely used method for the delivery of the material. Thus the assimilation characteristics of material in gaseous state have been investigated. The findings from recent experiments

at ASDEX Upgrade [46] [79] and TEXTOR [89] are summarized here shortly. First, one has to introduce an indicator that evaluates the quality of the assimilation. The fueling efficiency describes the amount of impurity atoms that are ionized and hence absorbed in the plasma, compared to the total number of injected atoms:

$$\Phi_{eff} = \frac{N_{ion}}{N_{tot}} \tag{4.3}$$

In the case of ASDEX Upgrade, the ion density can be measured indirectly. The CO_2 laser interferometer acquires the line-integrated electron density throughout the plasma at two lines of sight (V-1 and V-2). This diagnostic sends out two infrared laser beams which are both split up before entering the plasma into primary beams and reference beams. The primary beams traverse the plasma and are phase shifted depending on the plasma density. A comparison with the reference beams allows the determination of the line-integrated density along the lines of sight. For an electron temperature at the plasma edge of about 2.5-3 eV, impurities like neon are singly ionized according to the ADAS Database [82]. Therefore the rise in electron density during gas injection is directly proportional to the amount of assimilated gas atoms and reflects the ion count N_{ion}.

$$N_{ion} = \frac{Vol}{2} \int \left(\frac{\Delta \int n_e dl_{V-1}}{l_{V-1}} + \frac{\Delta \int n_e dl_{V-2}}{l_{V-2}} \right) \frac{dt}{\Delta t_{eff}} \tag{4.4}$$

Here, Vol describes the total plasma volume, l_{V-1} and l_{V-2} are the lengths of the lines of sight and Δt_{eff} is the effective time over which the gas assimilation occurs. The total number of injected impurity atoms is given by the volume of the gas reservoir in the valve, the pressure and the gas temperature.

$$N_{tot} = \frac{p * V}{k_B * T} \tag{4.5}$$

Based on these definitions, multiple experiments were performed to assess the quality of the gas injection in dependence on gas and plasma parameters, as well as different valve locations and a varying number of valves at different toroidal locations.

The most influential driver for the gas assimilation was found to be the distance between the valve orifice and the plasma edge. The closer the valve is located to the plasma, the higher the fueling efficiency is. Studies performed at ASDEX Upgrade, which compared valves at distances of 1.5 m and 0.1 m from the plasma edge showed an increase of the fueling efficiency by a factor of 2-3 when injected into similar plasmas. The peak fueling efficiency was found with the in-vessel valves at over 80 % [46]. Investigations at TEXTOR with a 0.8 m long guiding tube between the valve and the plasma confirm the result with a peak fueling efficiency of 50 %. DIII-D with its guiding tube of 1.3 m length achieved an efficiency of 40 % [81]. Another advantage of in-vessel valves close the plasma is the elimination of the delay time between the valve trigger and the arrival of the gas at the plasma edge.

The experiments also revealed a dependence of the poloidal position of the valve. Impurity injection from the high field side (HFS) has proven to be up to 50 % more effective than from the low field side (LFS) at comparable gas and plasma conditions. It is assumed that this is due to the larger distance between injection location on the HFS and the magnetic surface in the plasma where the safety factor q = 2, extending the pre-TQ time and thus allowing more gas to be assimilated. This is only valid up to a certain amount of injected atoms though. Above that limit, fueling efficiencies during injection from HFS and LFS are equal (Fig. 4.3 [46]).

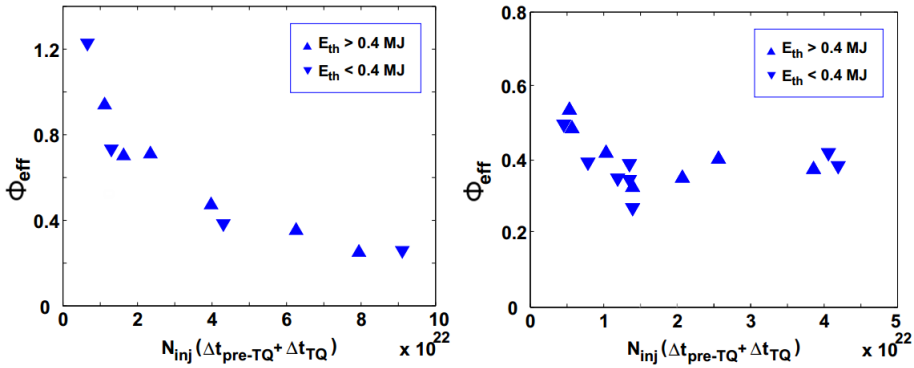

Figure 4.3: Comparison of Φ_{eff} for HFS (left) and LFS (right) injection over different amounts of injected atoms

It is also visible, that the fueling efficiency drops significantly with the amount of injected material. This is due to the buildup of a steep density gradient at the edge during impurity injection. The accumulated material cools the plasma edge rapidly and the diffusion into the plasma center is slow. Although the absolute electron density is still increased with higher amounts of injected gas, the overall fueling efficiency becomes low. In addition to that, a dependence on the plasmas thermal energy is not detectable. This is also valid for plasmas after the onset of the current quench. Although a large share of the thermal energy has been radiated at this point, the remaining fraction is still sufficient to ionize the impurities and hence increase the electron density in post-TQ plasmas. A visible influence of the gas pressure could not be found. When injecting the same amount of gas atoms from two different volumes, respectively with two different pressures, the resulting electron density was the same. With higher gas pressure the onset time of the current quench is reduced slightly and the rise in density is a bit faster, but the fueling efficiency remains the same. The number of valves that is used to inject the gas plays a minor role. If the same amount of material is injected from one location or from two, does not influence the fueling efficiency. On the other hand, the density distribution of the impurities in the plasma becomes more homogeneous when multiple valves at different toroidal locations are used. This is beneficial concerning the radiation cooling during the thermal quench.
Investigations at ASDEX Upgrade and TEXTOR concerning the gas species indicate that the fueling efficiency drops with increasing atomic mass of the impurities. In the case of TEXTOR with its valve located 800 mm away from the plasma, this is mainly due to smearing of the gas pulse. Hence, only a small pressure front reaches the plasma and starts the edge cooling before the bulk reaches the plasma. Additionally, mid-Z materials are very efficient in cooling the plasma. Therefore, the plasma has already lost most of its thermal energy and the majority of the injected atoms cannot be ionized anymore. Low-Z materials like helium have a high Φ_{eff}, but their cooling capability is low. Because of this, argon and neon are widely used for disruption mitigation, due their relatively high cooling capability and good RE mitigation performance.

Chapter 5

Requirements for the new valves

Before the development of new valves can begin, the technical requirements have to be outlined. Based on the experiences made with previous valves and on the experimental findings, one can formulate a list of requirements for the design of new valves for massive gas injection in ASDEX Upgrade. The most important lesson learned from the experiments is to optimize the valves for best fueling efficiency. The impurity load onto the vacuum system and the vessel walls can be reduced significantly by this measure.

- In-vessel valves
  As mentioned in chapter 4, the fueling efficiency depends strongly on the distance from the valve to the plasma edge. Long guiding tubes lead to a pressure drop and a slightly delayed gas arrival at the plasma. Thus, such a setup should be avoided. The valves close to the plasma at ASDEX Upgrade have shown the best performance concerning fueling efficiency and such an arrangement should be considered for the next generation of valves. This cancels out electromagnetic valves that can hardly be operated inside the Tokamak due to its size. Additionally, the valves have to withstand in-vessel conditions.

- Magnetic high field side injection

  It has also been found that the injection from the magnetic high field side leads to better assimilation of the impurities in the plasma. Due to the very limited space on the HFS behind the heat shield, small valves are required. The heat flux at this position does not pose a significant issue, but all non-metal components of the valve must have no direct line of sight to the plasma.

- Valve size

  The fueling efficiency is low for large amounts of injected gas and the onset time of the current quench gets shorter for higher gas pressures. Additionally, the forces and heat loads are mitigated quite well even for low amounts of injected material. These factors all favor the use of multiple valves with small gas reservoirs at high pressure, symmetrically distributed around the torus. This is also beneficial concerning toroidal radiation asymmetry. The valve size is ultimately limited by the space behind the inner heat shield when going for HFS injection.

- Internal gas volume

  Regarding the necessary gas amount, one has to consider that the mitigation of thermal and mechanical loads require roughly the same amount of injected particles as RE mitigation. Concerning mechanical and thermal loads, the results presented in chapter 4.1 and 4.2 can be used as design criterion. There it was shown that gas amounts of 10^{22} particles are sufficient to mitigate forces and heat loads in medium size Tokamaks. This corresponds to $40\,\mathrm{Pa\,m^3}$. As for RE mitigation, the Rosenbluth density would call for the injection large quantities of gas. However, the experiments presented in chapter 4.3 revealed that the RE current decay time becomes reasonable short (3 ms) with injecting 10^{22} particles of argon. Hence the valve must provide a reservoir for at least $40\,\mathrm{Pa\,m^3}$.

- Reliability

  Another requirement is, that the valve has to be constructed as robust as possible. It will experience the same magnetic flux change ($100\,\mathrm{T\,s^{-1}}$) during disruptions and thus be exposed to forces due to eddy currents. The valve components have to designed to undergo minimal deformation und these forces. This measure increases the reliability which is extremely important since in-vessel valves can only be accessed by opening the vessel.

- Opening time

  Pre-TQ time scales call for a valve that opens within milliseconds and the entire gas inventory has to be vented into the vessel equally fast. The actuation principle has to be laid out accordingly.

- Gas species

  The used gases are mostly noble gases and do not require special design considerations. But for the use of deuterium it is a necessity to exclude any form of ignition potential. Although it is unlikely that an explosive atmosphere could form inside the valve, safety measures call for either an extra gas chamber free of any ignition sources or an actuation principle that guarantees no possible form of ignition. Concerning materials, none can be used that either absorb deuterium in significant amounts or that undergo chemical reactions. Hence, components that come in contact with deuterium should be made from stainless steel.

- Heat loads

  From previous experience, thermal loads during plasma discharges are not a problem for the valve as they are protected by shielding tiles. But the baking of the entire machine before every experimental campaign has caused problems in the past. The baking is done to remove water from the interior surfaces of the vessel in order to achieve better vacuum conditions. Therefore the vessel is heated up to 150 °C. The valve and all its components have to withstand this temperature without being damaged.

- Ultra-high vacuum

  The valve has to be compatible with the vacuum conditions inside the vessel. All used materials must not outgas at pressures below 1×10^{-5} Pa. Further the valve seal must ensure leaking rates below $1 \times 10^{-8} \frac{\mathrm{Pa\,m^3}}{\mathrm{s}}$.

- Radiation

  Concerning neutron radiation, all materials must not contain elements that are highly activated or create long living isotopes by neutron interaction. The actuation mechanism must also remain unaffected by neutrons to ensure operability over a long period of time. The neutron flux is relatively low in present day plasma experiments ($10 \times 10^{13}\,\mathrm{m^{-2}\,s^{-1}}$), but it will have to be taken into account regarding future fusion devices.

- Magnetic field

  As the valve is operated inside the Tokamaks magnetic field, all materials and actuators must not be influenced by field strengths of up to 4 T and must not perturb the magnetic field topology. This calls for materials with a magnetic permeability below 1.05.

The complete list of requirements can be found in appendix A.

Chapter 6

The spring-driven valve

This chapter contains the design and testing processes for the new spring-driven valve. This new spring-driven valve is an improved design of a valve type that has been used at ASDEX Upgrade since 2011. The old defective valves were removed from the vacuum vessel and examined to find the reasons for their failure. From the information gained during the operation of the old valve, the retrieval from the vessel and the examination it was possible to determine what improvements had to be made to the new valve design in order to increase reliability. The following list summarizes the weak spots found in the old valve.

- The stem slides when the compressed air is vented.
- The micro switches for position detection fail during baking.
- The valve opens a bit too slow.
- The valve sealing fails after several operational cycles.
- The size of the valve is at the limit of what can be installed on the HFS.
- Crucial parts of the valve cannot be maintained non-destructively.

These points were considered for improvement during the design of the new valve. In the following it is explained how these weaknesses would be eliminated.

6.1 Working principle

The new valve has basically the same working principle as the previous model. Figure 6.1 shows the scheme of the new valve. In the idle state, the gas chamber (6) of the valve is open. To prepare the valve for fast gas release, compressed air is let into the rear chamber (1). The rear bellow (2) is compressed in axial direction, pushing the stem (3) forward, expanding the front bellow and pressing the valve plate (5) into the seal, thus closing off the gas chamber (128 cm^3). The stack of disk springs (4) is compressed simultaneously. When the stem has reached its final position, an electrical voltage is applied to piezoelectric stack actuators (7a, 7b) which are mounted perpendicular to the stem. The expanding actuators press two clamps on the stem on opposite sides, holding it in its current position. The compressed air is then vented from the rear chamber and the rear bellow expands. At the same time, the mitigation gas is let into the gas chamber. The valve is now ready to release the gas. If the valve is triggered, the piezoelectric actuators are discharged and they contract, releasing the stem. The disc springs accelerate the stem and the valve plate backwards, opening the gas chamber and venting the mitigation gas onto the plasma.

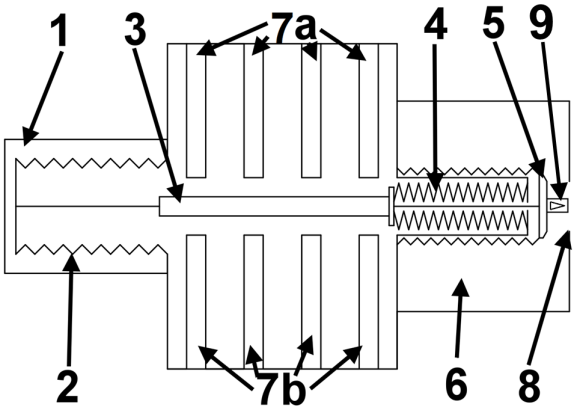

Figure 6.1: Principle sketch of the spring-driven valve

6.2 Valve components

In this section all major components of the spring-driven valve are described and the reasons why they were selected or designed in this distinct manner is explained. This includes all analytical calculations as far as they are of importance for the valves operational characteristics. In the case of the valve stem, additional experimental data concerning its friction coefficient is presented.

6.2.1 Disc springs

The stack of disc springs is responsible for the acceleration of the stem and the valve plate, hence determining the opening time of the valve. The force of the stack has to be large enough to accelerate the stem, the valve plate, the front bellow, the bolt and the spring itself. On the other hand it must not exceed the allowed lateral force on the piezoelectric stack actuators and it must be above the friction force between the stem and the clamps.
It was decided to use a stack, because the stack provides a high stiffness and force, as well as relatively low space requirements and mass. The stack contains 47 discs of the type Schnorr 002 700A discs [90]. The geometry of a single disc is given by its outer diameter $d_o = 12.5\,mm$, inner diameter $d_i = 6.2\,mm$, thickness $th = 0.7\,mm$ and a free stroke of $h_0 = 0.3\,mm$. The stack is assembled of disc pairs in column configuration and a single spring at the end of the stack. This form allows the spring force to remain constant while the effective stroke is increased by the number of discs. The spring force F and the stiffness k of the whole stack can be approximated by Eq. 6.1 and Eq. 6.2 as long as the stroke of each disc $s < 0.75 * h_0$.

$$F(s) = 0,034 * s^3 - 1,288 * s^2 + 72,199 * s \tag{6.1}$$

$$k(s) = 0,102 * s^2 - 2,576 * s + 72,199 \tag{6.2}$$

The force of one disc compared to the force of the stack depending on the stroke is shown in figure 4.2. The allowed stroke for the stack is increased compared to a single disc from 0.225 mm to 10.6 mm, but the maximal force of

660 N remains the same. The material of the discs has to be compatible with the magnetic and nuclear requirements. Therefore the entire stack is made of stainless steel 1.4301. Hence the total mass of the stack accounts for 0.021 kg and the effective mass[11] in the equation of momentum is 0.007 kg. The friction between the discs can be neglected due to the column configuration.

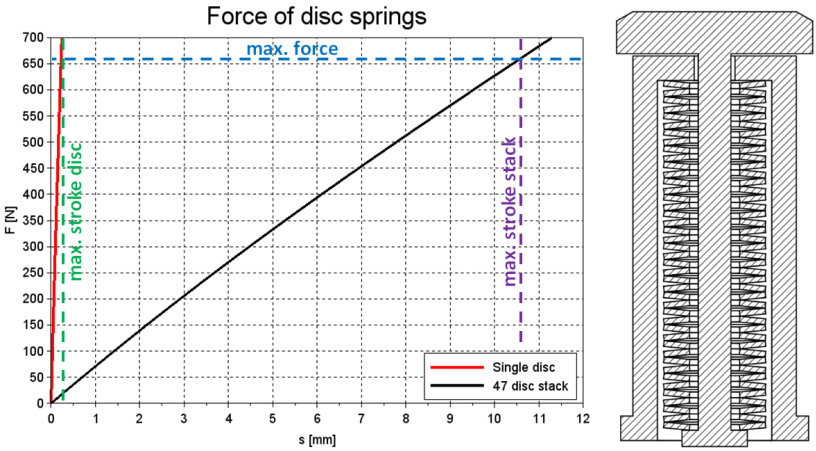

Figure 6.2: Force F of a single disc and of the whole stack as function of the stroke s (left) and configuration of the disc spring stack (right)

6.2.2 Bellows

The valve contains two bellows serving different purposes. The rear bellow is used to transfer the pressure force of the compressed air onto the valve stem and isolate the piezo-chamber from the rear chamber. This bellow is a Witzemann BAA 27x41x2x0.2 [91] with 8 corrugations and an effective area of 9.1 cm^2. The upper pressure limit for this type is 3.2 MPa allowing a total force of 2912 N. Demands concerning the material are met by the stainless steel 1.4571. The stiffness of the rear bellow is 32.5 $\frac{N}{mm}$ with an uncertainty of 30 %. Since the rear bellow is not fixed to the valve stem, it is not accelerated during the valve opening. Hence, it has not to be taken into account in the

[11] Effective mass describes here the mass of linearly compressed components in the momentum equation (m_{eff} = m/3). It is derived from the kinetic energy during linear expansion.

momentum equation, unlike the front bellow. The purpose of the front bellow is to relieve the valve plate from the gas pressure. Otherwise the valve would have to open against a pressure force of up to 1900 N (5 MPa). This bellow is a Witzemann BAA 16.8x24x2x0.15 [91] with 17 corrugations and an effective area of 3.25 cm^2. This area corresponds to an orifice diameter of 20.3 mm. It is designed to withstand a pressure of 7 MPa and is made of stainless steel 1.4571. Its stiffness is specified to be 24.7 $\frac{N}{mm}$ with an uncertainty of 30 %. The valve plate is directly welded to the front bellow. Hence stiffness and mass of the bellow are of importance for the opening time. The total mass of the bellow is 0.02 kg and the effective mass would be 0.007 kg.

6.2.3 Valve stem

The valve stem transfers the force from the rear bellow to the front bolt and thus the disc springs. In addition to that, it acts as rest for the tensed spring stack when clamped by the PE stacks. Therefore the design criteria for the stem are the elasticity, friction between steel and ceramic and mass. The requirements concerning resistivity against radiation, baking temperature and magnetic field have to be met as well.

The stem is a quadratic bar with the dimensions 8 mm x 8 mm x 48 mm which is made of sintered ceramic. This ceramic is a Buntenkötter Alsint 99.7 composed of 99.7% Al_2O_3. According to specifications it is compatible with the UHV and magnetic conditions and is fit for the thermal stress. Only the high aluminum contend poses a slight problem because it forms isotopes with moderate activity under the given neutron spectrum. The mechanical properties meet the requirements with respect to elasticity (370 $\frac{kN}{mm^2}$) and mass (3.93 $\frac{g}{cm^3} \Rightarrow$ 12.1 g).

To ensure that the static friction coefficient between the stainless steel clamps and the ceramic is sufficient, it was investigated in a simple experimental setup that closely resembles the assembly in the valve. The ceramic was clamped between two stainless steel plates and the clamping force, acting as normal force F_N was measured by a load cell. A force transducer was then pressed against the stem, representing the spring force in parallel direction.

The force transducer was pushed with increasing force until the stem began to slide between the plates. The analogue signal of the transducer was recorded during the procedure. An analysis of the data showed a peak of the parallel force F_{max} directly before the onset of the movement (Fig 6.3a). This force was taken as static friction force and used to compute the static friction coefficient. The linear dependency between the static friction force and the perpendicular force is clearly visible in Fig. 6.3b. The static friction coefficient for the old ceramic is slightly higher with a value of 0.91 compared to the new ceramic with a coefficient of 0.78. This can be explained with increasing surface roughness of the ceramic due to wear.

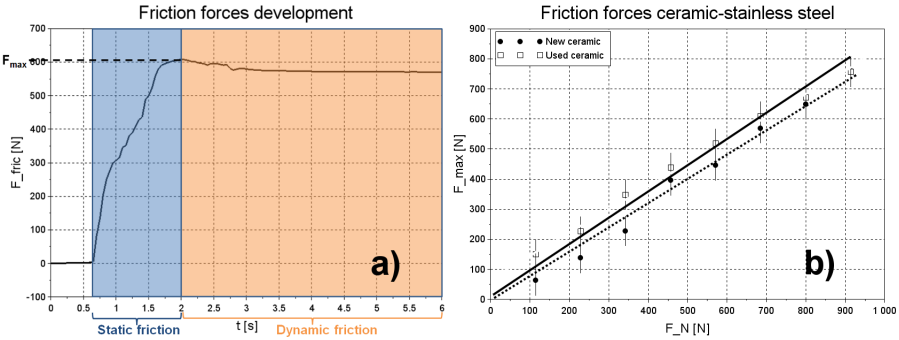

Figure 6.3: Development of the friction force for a new ceramic at $F_N = 690N$ (a) and the maximal friction force F_{max} as a function of the normal force F_N

6.2.4 PE actuators

A total of eight piezoelectric stack actuators is used to hold the ceramic stem in place, keeping the valve closed. Piezoelectric stacks were chosen for this task due to their insensibility to magnetic fields, temperatures of up to 150 °C and UHV conditions. Furthermore, they have a fast response time which is essential to release the stem on the desired time scale. Eight stacks are installed on opposing sides of the stem (four on each side) with their direction of expansion perpendicular to the direction of movement of the stem. Each stack is of the type piceramic P-888.91 [92] with a cross-sectional area of 10

mm x 10 mm and a length of 36 mm. The length of the stack determines the maximal elongation of the stack which is 0.038 mm ± 0.008 mm, while the cross-sectional area defines the maximal force which is 3800 N for this stack. These values are reached when the stack is supplied with 120V DC. The maximal force, called blocking force, is only achieved if the stroke of the stack is kept at zero. As the stack expands, the force decreases linearly until it reaches zero at the maximal stroke. These characteristics depend on to the supply voltage. In the closed state of the valve, both the front bellow and the disc springs generate a combined force of 446 N. This force has to be counteracted by the clamping force of the piezoelectric stacks. Using the static friction coefficient of the new ceramic, the stacks have to provide a perpendicular force of 572 N. Hence, each stack has to generate a force of 71.5 N which corresponds to an elongation of 0.0008 mm. Thus the stack can perform 98% of its maximal stroke and still achieve the necessary force to ensure sufficient friction. This leaves the stem enough space to slide freely when the stacks are discharged and the valve opens. However, the stacks have to be adjusted after the valve is assembled to compensate for inaccuracies during the installation. Therefore a M6 screw with fine thread is mounted behind each stack. This screw is separated by a thin metal membrane from the interior volume of the valve, which thereby remains a closed volume. By turning these screws from the outside, the stacks on the inside can be moved closer to the stem. Additionally, each stack is pre-stressed using leaf springs. This is needed to push the metal clamps apart when the stacks retract and to pre-stress the stacks themselves. Without this pre-stressing the ceramic plates in the stacks could delaminate under the stacks own inertia, destroying the stack.

6.2.5 Valve seal

The main valve seal is located between the valve plate and the nozzle entrance. In the closed state the conical edge of the valve plate is pressed into the circular opening of the seal, closing off the gas reservoir. The seal is a ring shaped viton plate with an outer diameter of 48 mm, an inner diameter of 20 mm and

a thickness of 2 mm. The outer diameter and the thickness were chosen to fit into a standard CF40 flange connection. Hence the viton plate also serves as seal between the gas reservoir and the nozzle flange. The inner diameter fits to the hydraulic diameter of the front bellow. Thus, there is no effective pressure force from the gas inside the reservoir acting on the valve plate. The seal is manufactured from a 2 mm thick viton plate by stamping. Microscopic investigations have shown that the plate material has fewer and smaller holes compared to the vulcanized and polished material used in the old valve design. Additionally, the stamping procedure allows fast and easy manufacturing.

6.2.6 Nozzle

The valve nozzle (Fig. 6.1 (8)) is made from a standard CF40 flange. This flange has a centered circular drilling with a diameter of 13 mm which serves as straight nozzle. The straight design has the advantage of low manufacturing effort while having very little drawbacks concerning outflow velocity and mass flow rate compared to an adjusted nozzle. Further, the diameter of the orifice is designed to prevent a direct line of sight between the plasma and the viton seal. This is necessary since viton degrades under ultraviolet radiation. The mass flow rate and the reservoir pressure can be estimated using the compressible gas law in the critical flow cross-section and the ideal gas law.

$$\dot{m}(t) = \frac{p_0(t) * A(t) * \sqrt{\gamma}}{\sqrt{R_s^g * T_0}} * \left(\frac{\gamma+1}{2}\right)^{-\left(\frac{\gamma+1}{2*(\gamma-1)}\right)} \tag{6.3}$$

$$\frac{\partial p_0}{\partial t} = \dot{m}(t) * \frac{R_s^g * T_0}{V_0} \tag{6.4}$$

Here $\dot{m}$ is the mass flow rate, p_0, T_0 and V_0 are the reservoir gas pressure, temperature and volume, R_s^g is the specific gas constant of the mitigation gas and γ is its adiabatic constant. The critical cross-sectional area $A(t)$ is time dependent as the valve plate moves and it changes its location during the valve opening. In the first phase, the critical area A_1 is located between the nozzle entrance at the viton seal and the valve plate. When this area becomes larger than the nozzles cross-sectional area A_2, the critical flow cross-section

moves its location into the nozzle.

$$A_1(t) = \pi * d_i * x(t) \tag{6.5}$$

$$A_2 = \frac{\pi}{4} * d_n^2 \tag{6.6}$$

Here, d_i is the inlet diameter of the viton seal, in this case 20 mm and d_n is the nozzles diameter, which is 13 mm for this valve. $x(t)$ describes the movement of the valve plate which can be assumed to be linear. Another assumption, that was made for the calculation is that the reservoir temperature remains constant over the evacuation time. Under these assumptions and with the given values, the stroke at which the critical flow area changes from A_1 to A_2 is 2.11 mm.

6.2.7 Position detection

The position detection system is of great importance for the safe operation of the valve. Since the valve is located inside the vacuum vessel and it is normally open, the position detector is the only way of knowing if the valve is closed and gas can be let into the reservoir without flooding the vessel. However, leaking or damage to the valve seal can only be found by the pressure sensors during filling of the gas reservoir. The micro switches which were used in the old valve closed electrical circuits depending on the position of the valve plate. The investigation of the old valve that was retrieved from the vessel of ASDEX Upgrade showed that the micro switches had fallen apart possibly due to forces during disruptions and their electrical connectors had deteriorated probably during baking. To avoid these problems, an optical system was developed for the new valve, consisting of a light source (820 nm) outside the vessel, a small metal plate attached to the valve plate that is moved through the beam and a receiver outside the vessel. Optical fibers with a diameter of 0.4 mm connect source and receiver with the valve. The attached plate is manufactured from stainless steel with a size of 2 mm x 4 mm x 11 mm with a milled recess of 2 mm width in the middle (Fig. 6.4). This recess reduces the thickness of the plate to 0.3 mm. A drop like contour is eroded in this recess, which is

positioned in such a way that the beam of light passes through the narrow end, if the valve is opened, and through the thick end of the drop, if the valve is closed. Hence the signal of this light barrier setup is close to zero if the valve is open or if the position detector is broken and is at its maximum if the valve is closed and safe for filling. In the vessel, the ends of the optical fibers are fixed on opposing sides of the nozzle flange perpendicular to the nozzle axis. The receiver side is equipped with a collimator lens to collect more light and achieve a higher output signal. Although the position detector will be used primarily to determine the open or closed positions during operation, it also allows the observation of the movement of the valve plate in real time. For both purposes, the light signal is converted to an analogue voltage signal. It is calibrated to give an output of 0 V, if the valve is open and 10 V, if the valve is closed.

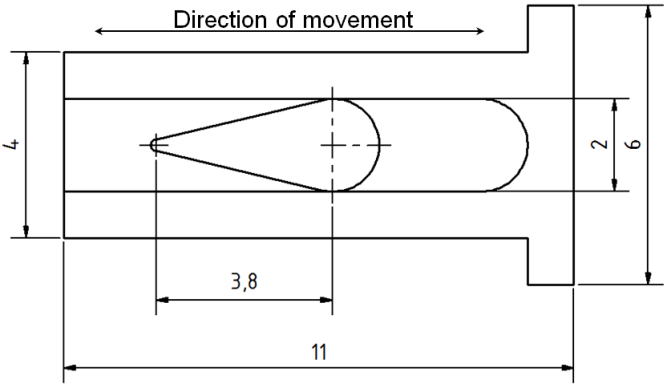

Figure 6.4: Geometry of the attachment for position detection

6.2.8 Clamping mechanism

The sliding of the stem was one of the main problems with the old valve. This was investigated thoroughly and it was found that the clamps which are pressed against the ceramic by the PE actuators were too stiff. The actuators could not be adjusted precisely after assembly. This lead to a tilt of the clamps and thus not sufficient friction between stem and clamps. This issue was solved by redesigning the entire clamping mechanism. Another

pair of PE actuators was added for safety (6 actuators in the old valve) and the clamps were constructed with soft joints between the areas where the actuators press against. This prevents tilting of the clamps, even when some actuators do not reach their designated expansion. To compensate for uneven expansion, adjustment screws with fine thread are placed in the valve block behind each PE actuator. These screws are accessible from outside the valve to allow individual adjustment of each PE actuator in the assembled state. As the chamber, in which the PE stacks rest, is sealed off and remains under atmospheric pressure (no change in friction between stem and clamp), the screws press on a thin metal membranes (one on each side of the valve) which are eroded in the valve block and serve as barrier between the chamber and the environment while transmitting the pressure of the screws onto the PE stacks.

6.2.9 Valve assembly

The main components of the valve, which were described before, are assembled into different sub-assemblies. This is done to simplify the assembling process itself and for better maintainability. The complete valve can be roughly separated into four sub-assemblies:

- The rear cap, which holds the rear bellow, the electric plugs for the piezoelectric stack actuators and the connectors for the gas lines (Fig. 6.5 blue)
- The valve block, which holds the clamping mechanism with the piezoelectric stacks, the clamps and the ceramic, as well as the gas reservoir (Fig. 6.5 orange)
- The spring unit, which holds the stack of disc springs, the front bellow, the valve plate and the attachment for the position detector (Fig. 6.5 green)
- The nozzle flange, which holds the optical fibers (Fig. 6.5 purple)

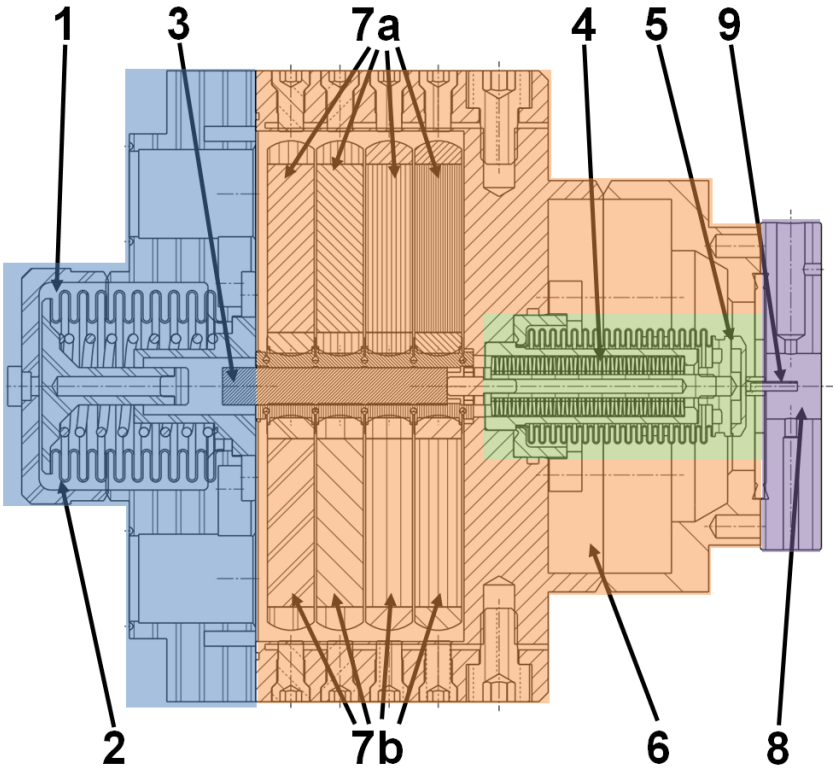

Figure 6.5: Assembled valve with colored sub-assemblies and numbered active components according to Fig. 6.1

The rear cap assembly consists of a base plate (Fig. 6.6 (1)), a dome cap (Fig. 6.6 (2)), the bellow plate (Fig. 6.6 (3)), the rear bellow (Fig. 6.6 (4)) and a return spring (Fig. 6.6 (5)), as well as the connectors for gas and voltage supply. The bellow plate is welded onto the rear bellow, which is then welded into the base plate. The dome cap is then carefully welded onto the base plate, closing the volume around the bellow. The gas lines for the mitigation gas and the leak search helium, as well as the Sub-D electrical connectors are then welded into the base plate. The gas line for the pressurized air is welded into the dome cap. The return spring, which has a low spring rate, is pressed against the bellow plate using a simple fitting (Fig. 6.6 (6)) as counteracting support.

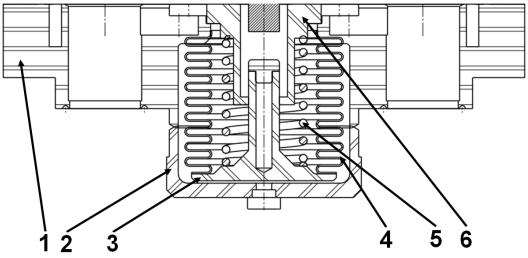

Figure 6.6: Assembly of the rear cap

The rear part of the valve block holds piezoelectric stack actuators (Fig. 6.7 (1)), the clamps (Fig. 6.7 (2)) and the ceramic stem (Fig. 6.7 (3)). The actuators are stacked into an eroded pocket in block, separated by thin viton plates. The clamps are placed in front of the two rows of actuators and the ceramic is positioned between the clamps. The space (Fig. 6.7 (4)) between the back of the actuators and the wall of the pocket is filled with thin metal sheets. The M6 fine thread screws (Fig. 6.7 (5)) press from the outside onto the separating membrane (Fig. 6.7 (6)) and the metal sheets, thereby adjusting the actuators. The front part of the valve block contains the gas reservoir (Fig. 6.7 (7)).

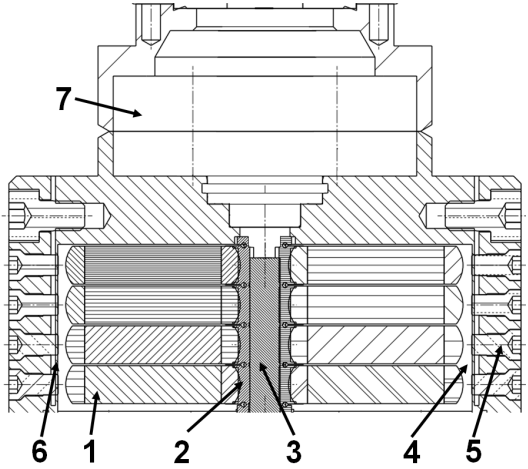

Figure 6.7: Assembly of the valve block

The spring unit consists of a metal bolt (Fig. 6.8 (1)) with a M4 thread at the top on which the disc springs (Fig. 6.8 (2)) are stacked. A shell (Fig. 6.8 (3)) serves as casing for the discs and as counteracting support for the stack. This configuration is placed into the front bellow (Fig. 6.8 (4)), which has the valve plate (Fig. 6.8 (5)) welded to its top and a socket (Fig. 6.8 (6)) welded to its bottom. The bolt is screwed into the valve plate, holding the unit together. The pre-stress on the stack and the length of the unit can be adjusted by screwing the bolt further into the valve plate. This affects the opening time and the stroke.

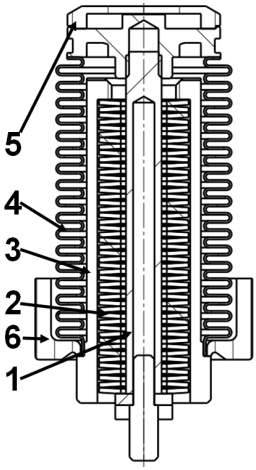

Figure 6.8: Assembly of the spring unit

For the final assembly all sub-assemblies are put together. First, the actuators are connected to the Sub-D plugs in the rear cap. A gold wire serving as main seal between the components is placed in the foreseen immersion and a viton O-ring is placed where the gas line runs through. Cap and valve block can then be fastened together by a total 22 M5 screws. The spring unit is placed in the immersion within the gas reservoir. A radial O-ring seal and a gold wire tighten off the gas reservoir from the piezo-chamber. A ring is placed over the edge of the socket and fastened to the valve block, keeping the spring unit in place. Finally the main valve seal is laid on top of the gas reservoir and fixed with the nozzle flange.

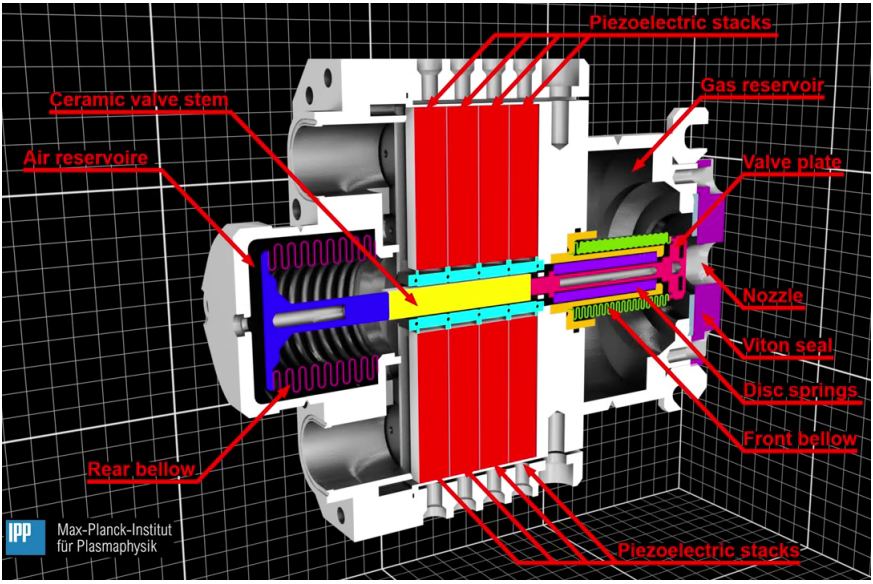

Figure 6.9: 3D model of the assembled spring-driven valve

Chapter 7

The piezoelectric valve

The piezoelectric valve is a new design for MGI valves based on the thermal helium beam diagnostic developed at TEXTOR [93]. The valve plate is directly propelled by the piezoelectric stack actuators, using a monolithic titanium stroke amplifier. It is constructed for in-vessel application and is normally closed, while the spring-driven valve operates as normally open valve. The normally closed layout has advantages over the normally open type:

- Simple construction and better maintainability due to fewer parts
- Simple operation cycle, because the valve doesn't have to be actively closed before or after operation
- Little wear due to frictionless layout
- High reliability due to no-slip design
- Small in size compared to spring-driven valves

However, since force and stroke of the amplified actuators are limited, the active parts of the valve have to be constructed with great care and precision.

7.1 Working principle

The valve illustrated in figure 7.1 is closed in the idle state. The conical valve plate (5) is pressed into the viton seal by the steel bellow (3), sealing off the gas reservoir (4). The reservoir, which can hold 42 cm^3 of gas, can be filled with up to 5 MPa gas pressure. This corresponds to a maximum gas inventory of 210 $Pa\,m^3$ or $5 * 10^{22}$ particles. When the valve is triggered, a DC voltage of 200 V is applied to the piezoelectric stacks (2) which expand immediately. A monolithic titanium frame (1) amplifies the stroke of the PE actuators. The frame is firmly connected to the valve plate, which is pulled back by the deforming frame. Thus, the valve is opened and the gas is released through the nozzle (6).

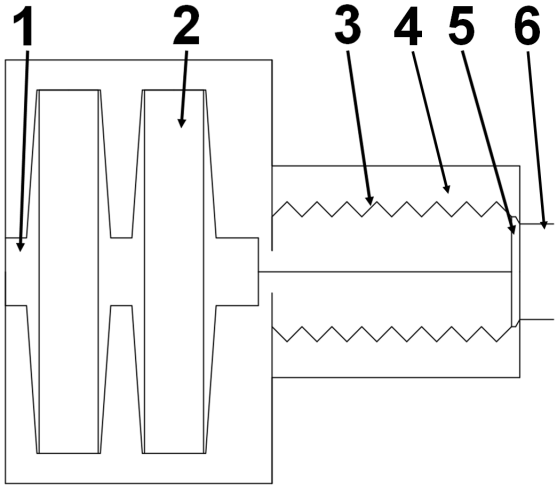

Figure 7.1: Principle sketch of the piezoelectric valve

7.2 Valve components

This section contains the information for all active components of the valve. Emphasis is put on the design and testing of the actuator since this is the critical part of the construction. However, since the actuator has strict operational limits regarding stroke and force, the other components have to be

chosen to fit the actuators properties while keeping the major design criteria, opening time, mass flow rate and gas inventory, in mind.

7.2.1 Actuator

The actuator ((1) and (2) in Fig. 7.1) is the main component of the valve. It pulls back the valve plate opening the nozzle. Hence, the actuator must have a short reaction time and a sufficient stroke to allow the maximal mass flow rate through the nozzle. The actuator consists of two parts, the piezoelectric stack actuators and a frame which serves as amplifier for the stroke of the PE actuators. This design is based on the long distance linear actuator PX 500 [94] by Piezosystem Jena, which is used in the thermal helium beam diagnostic developed at TEXTOR [93].

PE actuators

Four piezoelectric stack actuators (Fig. 7.1 (2)) are built into the valve actuator and serve as energy converter from electric to motional energy. PE actuators have proven to work reliably in magnetic fields, UHV and high temperature environments. The speed at which they expand is proportional to the electric current used to charge the stacks. Hence, the electric supply must be chosen accordingly to the electric capacity of the PE stacks. For the valve, stacks of the type Noliac NAC2023-H64 [95] with a cross-section of 15 mm x 15 mm and a length of 64 mm were chosen. The stacks are supplied with a maximum of 200V DC which allows a peak blocking force of 9450 N and a maximal stroke of 0.1 mm. These properties are governed by the stack dimensions. The blocking force is directly proportional to the cross-sectional area of the stack, while the stroke is proportional to the length. Longer stacks are available, but their mass, which is of great importance for the opening time of the valve, increases with the length. Hence, it was decided to use the shortest stacks that still fulfill the requirements. The variable length is possible since a PE stack consists of several plates, which are glued together. The glue is applied in very thin layers, so that the elasticity of the glue does not affect the stroke. Furthermore it is stable in UHV and high temperature environments.

However, if the stack is charged quickly, the inertia of the expanding stack can delaminate the plates. Thus the stack must always be operated under axial pressing force. As for the blocking force, there is currently no commercial PE stack available that can achieve more than 9450 N. Custom-made stacks were considered, but again the mass increases with the cross-sectional area so the standard stacks were preferred.

Blocking force and stroke are related linearly by the stacks stiffness. As the stack expands, the force, that the stack produces, decreases until it reaches zero at the maximal elongation. When different voltages are applied, the blocking force and the maximal stroke change, but the gradient of the characteristic lines, meaning the stiffness, remains the same. This makes modeling of PE stacks for the FEM (finite element method) analysis of the actuator very easy. A cuboid, resembling the stacks dimensions, is used for the FEM simulation. The elasticity of the material has to be calculated to represent the stacks stiffness.

$$E^* = \frac{F_0 * l}{A * \Delta l} \tag{7.1}$$

Here, E^* is the elasticity of the material used in the FEM simulation, F_0 is the blocking force, l is the length, A is the cross-sectional area and Δl is the maximal stroke of the stack. For the simulation, the blocking force has to be applied in the direction of expansion. The fineness of the mesh has proven to be of low importance. In the case of tetrahedral elements, an edge length of 10 % of the stack length for each elements produced results with errors below 5 % regarding the stroke. For an investigation of the stress distribution in the stack, it was found that the edge length of an element should not exceed 1 % of the stack length. Symmetric expansion to both sides has shown a lower peak stress than one sided expansion with a fixed end.

Amplifier frame

The frame (Fig. 7.1 (1)) fulfills two functions. It amplifies the stroke of the PE stacks and it pre-stresses each stack so they don't delaminate when charged. The amplification is necessary since the stacks only perform a stroke of 0.1 mm, which is far too small for a sufficient mass flow rate. The frame has to

operate with low maintenance in a high temperature and vacuum environment. Hence any joints can't be lubricated. Therefore, a monolithic design was chosen, meaning the frame is manufactured from one solid workpiece. Furthermore it must be uninfluenced by magnetic fields and ionizing radiation, which limits the selection of applicable materials. The amplification is achieved by deforming rectangular triangles (Fig. 7.2 right image).

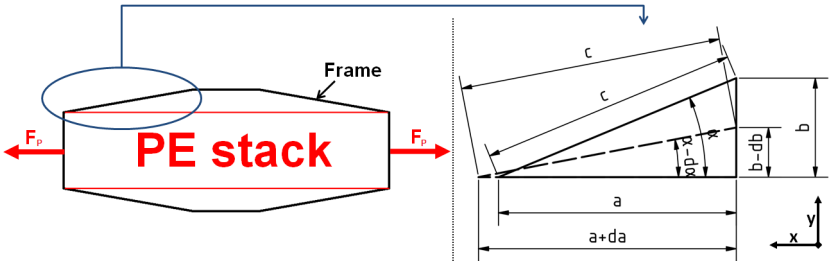

Figure 7.2: Operating principle of the amplifier frame

The frame (Fig. 7.2 left image) has a rhomb like shape which holds the PE actuators. When the stacks expand in the x-direction, the rhomb is deformed, leading to an amplification of the stroke in the y-direction. One leg of the rhomb is sketched on the right side of Fig. 7.2, with the solid line being the non-deformed leg and the dashed line being the deformed case. The amplification can now be derived from simple trigonometric relations.

$$a^2 + b^2 = c^2 \tag{7.2}$$

$$(a + da)^2 + (b - db)^2 = c^2 \tag{7.3}$$

$$tan\alpha = \frac{b}{a} \tag{7.4}$$

$$tan(\alpha - d\alpha) = \frac{b - db}{a + da} \tag{7.5}$$

Eq. 7.5 can be rewritten using the identity.

$$\frac{tan\alpha - tand\alpha}{1 - tan\alpha * tand\alpha} = \frac{b - db}{a + da} \tag{7.6}$$

Inserting Eq. 7.3 into Eq. 7.6 one derives

$$\frac{tan\alpha - tand\alpha}{1 - tan\alpha * tand\alpha} = \frac{\sqrt{c^2 - (a + da)^2}}{a + da} \tag{7.7}$$

Using Eq. 7.2 to supplement c^2 Eq. 7.6 is modified.

$$\frac{tan\alpha - tand\alpha}{1 - tan\alpha * tand\alpha} = \frac{\sqrt{a^2 + b^2 - (a + da)^2}}{a + da} \tag{7.8}$$

Finally b^2 is replaced using Eq. 7.4 to obtain

$$\frac{tan\alpha - tand\alpha}{1 - tan\alpha * tand\alpha} = \frac{\sqrt{a^2 + a^2 * tan^2\alpha - (a + da)^2}}{a + da} \tag{7.9}$$

Eq. 7.9 is rewritten to derive an expression for $d\alpha$, which only depends on the properties of the PE stack a, which is the half length of the stack, da, which is the half stroke and the non-deformed angle of the leg α:

$$d\alpha(a, da, \alpha) = arctan\left(\frac{\sqrt{a^2 + a^2 * tan^2\alpha - (a + da)^2} - (a + da) * tan\alpha}{\sqrt{a^2 + a^2 * tan^2\alpha - (a + da)^2} * tan\alpha - (a + da)}\right) \tag{7.10}$$

To determine the relationship between the stack properties, the original angle and the amplified stroke db, Eq. 7.10 can be implemented into Eq. 7.6.

$$db(a, da, \alpha) = a * tan\alpha - \frac{(tan\alpha - tand\alpha(a, da, \alpha)) * (a + da)}{1 - tan\alpha * tand\alpha(a, da, \alpha)} \tag{7.11}$$

The actual amplification of the frame depends on the number of legs which are in series. In the case of one rhomb, as shown in Fig. 7.2, the number of serial legs is two. Hence, the amplification can be increased further by adding rhombs on top of each other.

The blocking force of the actuator is reached, when the frame performs no movement in the y-direction and the stack only deforms the leg elastically. Thus, the geometry of the leg is very important.

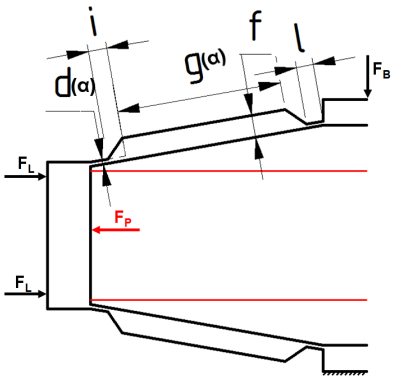

Figure 7.3: Geometry of the legs and active forces in the frame

Each leg (Fig. 7.3) consists of two identical thin joints with a thickness $d(\alpha)$ and a length l, which are connected by a thick bridge to counteract bending with a thickness f and a length $g(\alpha)$. Both ends of the bridge fall off over a length i. The width of the legs ext are equal to the width of the frame. The thickness $d(\alpha)$ and the bridge length $g(\alpha)$ are functions of the angle to be consistent with the parametric model described later.

$$d(\alpha) = d_0 * cos\alpha \tag{7.12}$$

$$g(\alpha) = \frac{g_0}{cos\alpha} \tag{7.13}$$

d_0 and g_0 being the lengths at an angle $\alpha = 0$. From this geometric information one can derive the elastic spring rate of one leg.

$$D_L(\alpha) = \frac{E^* * ext}{\frac{2*l}{d(\alpha)} + \frac{g(\alpha)}{f} + \frac{4*i}{f-d(\alpha)}} \tag{7.14}$$

The rhomb can be described as 2D framework. Neglecting parts of the frame, that don't take up any force or torque, the framework is reduced to a simple model with four bars representing the legs of the rhomb, two nodes where the PE stacks transfer their force and two fixed bearings. The upper fixed bearing describes a bearing which could move in the y-direction but the blocking force B_y keeps it in force equilibrium (Fig. 7.4).

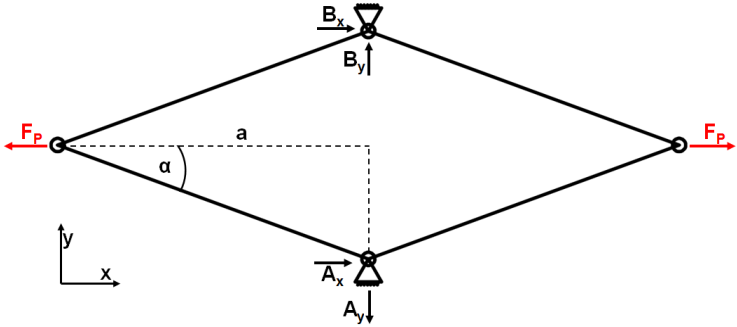

Figure 7.4: Framework model of the actuator

Results of the systems torque and force balances show, that the bearings don't take up any force in x-direction, but equal force in y-direction ($A_y = -B_y$) which corresponds to the blocking force. The relation between this blocking force and the force of the PE stacks is derived from the force balances of each node and bearing.

$$0 = B_y - 2 * F_L(x) * sin\alpha \tag{7.15}$$

$$0 = F_P(x) - \frac{2 * F_L(x)}{cos\alpha} \tag{7.16}$$

Considering the linear relation between force and stroke of the PE stacks and the elastic spring rate of the legs, the expressions for the PE force $F_P(x)$ with the blocking force F_0 and the elastic force of the legs $F_L(x)$ are described as shown in Eq. 7.17 and 7.18.

$$F_P(x) = F_0 - \frac{F_0}{da} * x \tag{7.17}$$

$$F_L(x) = D_L(\alpha) * x \tag{7.18}$$

Equation 7.14 allows the determination of the maximal stroke $\tilde{x}$ at which the PE stack and the frame are in force equilibrium.

$$\tilde{x}(\alpha) = \frac{F_0 * da * cos\alpha}{F_0 * cos\alpha + 2 * D_L(\alpha) * da} \tag{7.19}$$

The blocking force itself is then derived from Eq. 7.15 and Eq. 7.19.

$$B_y(\alpha) = F_B(\alpha) = 2{*}D_L(\alpha){*}\tilde{x}(\alpha){*}sin\alpha = \left(\frac{F_0 * da * D_L(\alpha)}{F_0 * cos\alpha + 2 * D_L(\alpha) * da}\right){*}sin(2\alpha) \tag{7.20}$$

To increase the blocking force, the geometry of the legs has to be optimized and multiple PE stacks can be installed parallel into the rhomb. The blocking force of each stack adds to the overall PE blocking force F_0. However, more PE stacks increase the mass of the actuator immensely. Stacking rhombs on top of each other has no effect on the blocking force of the frame, since only the frame with fixed legs determines the blocking force.
The linear relation between blocking force and stroke of the PE stacks is translated by the frame and is conserved. Thus, the characteristic of the actuator is completely described by the maximal stroke db and the blocking force F_B.

The equations 7.11 and 7.20 were checked using a parametric FEM simulation. The model was set up with two parallel PE stacks, each with a cross-section of 15 mm x 15 mm and a length of 64 mm. This results in a total blocking force $F_0 = 18900$ N and a half stroke $da = 0.05$ mm. The material of the frame was set to be titanium Grade 5 (Ti6Al4V) with an elasticity of $E = 114\,000\,\frac{\mathrm{N}}{\mathrm{mm}^2}$. As for the geometry, the following values were chosen: $ext = 31$ mm, $d_0 = 0.5$ mm, $l = 2$ mm, $f = 2.8$ mm, $g_0 = 19$ mm, $i = 2$ mm. The angle α, being the most influential factor, was kept as free parameter.
For each angle, two simulations were conducted; one without a force to the free end and one with a force of 50 N. Using the linear relation, the blocking force for each angle of the FEM model was derived.

$$F_{B,FEM}(\alpha) = \frac{50N * db_{FEM}(0N, (\alpha))}{db_{FEM}(0N, (\alpha)) - db_{FEM}(50N, (\alpha))} \tag{7.21}$$

A comparison between the results of the analytic model and the FEM simulation (Fig. 7.5) show a good agreement regarding the stroke at angles above 5°. The deviation at small angles is caused by overshooting of the legs, meaning that the legs have an angle $\alpha < 0$ in the deformed state. This is indicated by an imaginary term in the result of Eq. 7.10. The FEM model counteracts this

massive overshoot by increased stress in the legs. As for the blocking force, the analytic model overestimates the force roughly by a factor of two. This is mainly a result of a leg stiffness which is significantly higher than in the FEM simulation. Eq. 7.14 assumes a homogeneous stress distribution over every cross-section of the leg. The FEM model shows a stress distribution in the thick bridge, which is much thinner than the thickness f. However, the trend of the dependency between blocking force and angle seems to be correct, as the maximum force is reached at 45°.

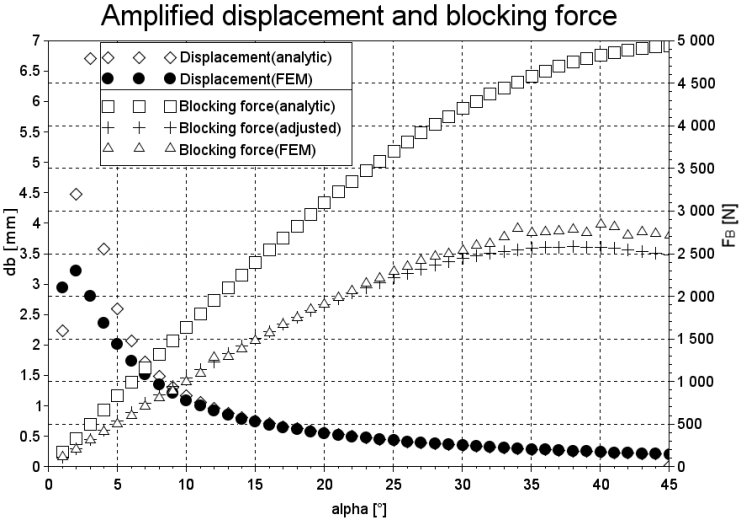

Figure 7.5: Comparison between results of the analytic model and the FEM simulations

A more realistic approach for the blocking force is achieved by assuming an even stress distribution in the joints and the bulky bridge. Since the leg is symmetric and the bulky part is much thicker than the joints, an exponential Ansatz with a plateau was chosen. The thickness $t_\sigma(\alpha, x)$ of the stress layer in the leg is described by Eq. 7.20.

$$t_\sigma(\alpha, x) = \frac{\frac{f}{2} - d(\alpha)}{(e^{i*(x-\frac{g(\alpha)}{2})} + 1) * (e^{i*(-x-\frac{g(\alpha)}{2})} + 1)} + d(\alpha) \tag{7.22}$$

This Ansatz allows a close representation of the actual stress distribution in the leg as shown in Fig. 7.6. It is clearly visible that the maximum stress occurs at the bottom of the leg as the joints are connected there, whereas the top of the bridge is mostly stress free.

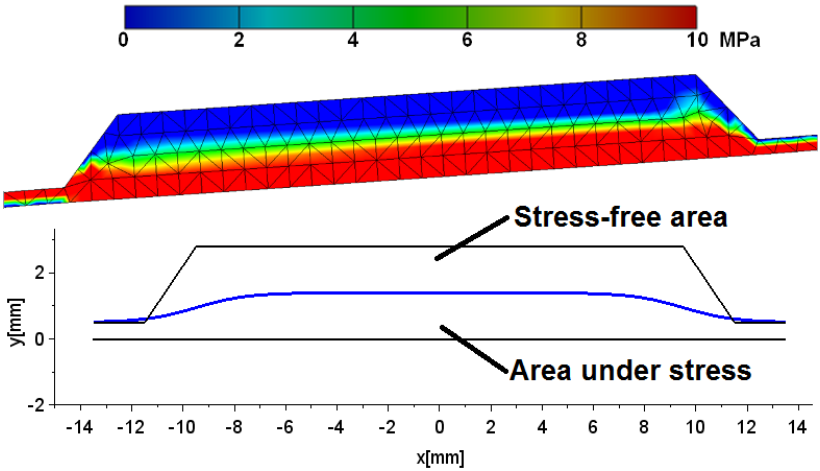

Figure 7.6: Stress distribution in the FEM model and representation by the distribution function

The elastic spring rate of the leg is then derived from the averaged thickness of the stress layer over the length of the leg.

$$D_L(\alpha) = \frac{E^* * ext}{2 * (\frac{g(\alpha)}{2} + i + l)} * \frac{2 * \int_0^{\frac{g(\alpha)}{2}+i+l} t_\sigma(\alpha, x)dx}{2 * (\frac{g(\alpha)}{2} + i + l)} = \frac{E^* * ext * T_\sigma(\alpha)}{2 * (\frac{g(\alpha)}{2} + i + l)^2} \tag{7.23}$$

$$\begin{aligned} T_\sigma(\alpha) = & \frac{(-f + 2d(\alpha))e^{g(\alpha)*i} ln(e^{\frac{g(\alpha)}{2}*i} + e^{\frac{g(\alpha)}{2}+i+l})}{g(\alpha) * (e^{g(\alpha)*i} - 1)} \\ & + \frac{(f - 2d(\alpha))e^{g(\alpha)*i} ln(e^{i*(g(\alpha)+i+l)} + 1)}{g(\alpha) * (e^{g(\alpha)*i} - 1)} \\ & + \frac{2 * i * d(\alpha) * (\frac{g(\alpha)}{2} + i + l) * (e^{g(\alpha)*i} - 1)}{g(\alpha) * (e^{g(\alpha)*i} - 1)} \end{aligned} \tag{7.24}$$

This adjusted spring rate can be directly implemented into Eq. 7.20. Using the same values as for the FEM simulations an adjusted blocking force was

calculated for angles $1° \leq \alpha \leq 45°$. The results, displayed in Fig. 7.5, show an excellent agreement between the FEM simulation and the adjusted analytical model. Unlike the ideal analytical model, the adjusted model has its maximal blocking force at an angle of 38°, which is due to the increased influence of the angle α on the elastic spring rate. This leads to slightly smaller blocking forces at large angles compared to the simulation results. The overall accuracy of the adjusted model compared to the ideal model is significantly better though.

Test actuator

The test actuator was built to check the reliability of the FEM simulations, using spare PE stacks from the spring-driven valve prototype. The final actuator for the valve requires large and thus expensive stacks, which is why it has to be proven that the design tool delivers realistic results. Only then is it possible to determine the final size of the necessary PE stacks and the geometry of the amplifier frame. The test actuator consisted of a frame with three stacked rhombs, each holding two parallel PE stacks of the type used in the spring-driven valve [92]. The frame was manufactured from a titanium Grade5 monoblock using wire erosion. The void length of each rhomb $2a$=35.88 mm was slightly smaller than the length of the PE stacks. Thus, the frame was deformed elastically during the assembly to fit in the stacks, pre-stressing the stacks in the process. This prevented delaminating of the stacks by their own inertial force when they expanded rapidly. Since the frame was deformed during the assembly, the manufactured leg angle $\alpha^* = 95.4°$ was chosen slightly larger than the operational leg angle $\alpha = 94°$. The leg geometry was chosen according to the previously explained factors: ext = 20 mm, d_0 = 0.56mm, l = 1.5 mm, f = 2 mm, g = 5.7 mm, i = 3mm. The assembled test actuator resembled a previously designed FEM model concerning geometry and mass (240g).

A series of FEM simulations was performed with increasing loads on the free end from 0 N to 150 N in steps of 10 N. The displacement in the y-direction was recorded for each step. To compare the test actuator to the simulations, the free end of the assembly was attached to a tension spring with low spring

rate ($1\,\frac{\mathrm{N}}{\mathrm{mm}}$), which was elongated in steps of 10 mm to resemble the load steps. For each load different voltages were applied to the ceramics, ranging from 20 V to 120 V in steps of 20 V. The voltage was supplied either slowly to observe a quasi-static displacement or abruptly using a manually operated capacitor circuit (Appendix C.3), to investigate the dynamic behavior. The displacement of the free end was observed by a fast laser displacement sensor and recorded by a fast oscilloscope for each case.

For the quasi-static investigation, the results are displayed in Fig. 7.7a. A linear behavior of the actuator is clearly visible with decreasing displacement as the load on the free end is increased. This corresponds to the linear behavior of the PE stacks, indicating that the titanium frame translates the characteristic properties of its stacks. This allows the definition of a blocking force and actuator stiffness for the assembly. In the case of the test actuator the blocking force can be derived from Fig. 7.7a by connecting the measurement points for each voltage. The point where the line crosses the x-axis is the blocking force for the respective voltage. For the maximal supply voltage of 120 V the blocking force is 160 N. The stiffness of the actuator is calculated by dividing the blocking force by the displacement at 0 N load for each supply voltage. Hence, for the maximal voltage of 120 V the stiffness of the assembly is $175\,\frac{\mathrm{N}}{\mathrm{mm}}$. The spring rate of the spring used for the load can be neglected since it is small compared to the stiffness of the actuator. A comparison with the FEM simulations shows a very good agreement between the model and the experiment. Hence, FEM is an adequate tool for the design of the valve actuator.

When the voltage is supplied instantaneously ($\Delta t_{supply} \rightarrow 0$) the maximal displacements are significantly higher compared to the quasi-static case (Fig. 7.7b). This is due to an overshoot of the actuator as a result of the actuators own inertia. The maximal displacement is on average 60 % higher than for the quasi-static case. Hence, the valve actuator can be designed to reach the maximal stroke by overshooting although it has to be taken into account that the actuator swings back almost to its initial position. Thus the time between onset of the movement and end of the swing back is of great importance to ensure the fast opening time of the valve and the evacuation of the gas reser-

voir before the actuator swings back. Two time points were extracted from the displacement data of the fast charge experiments, one at which the free end reaches the displacement from the quasi-static measurement (Fig. 7.7c) and one at which the maximal displacement during the overshoot is reached (Fig. 7.7d). It is clearly visible that the supply voltage has no influence on the displacement times as the quasi-static displacements are reached after 2 ms to 2.5 ms and the maximal displacements are reached after 3.5 ms.

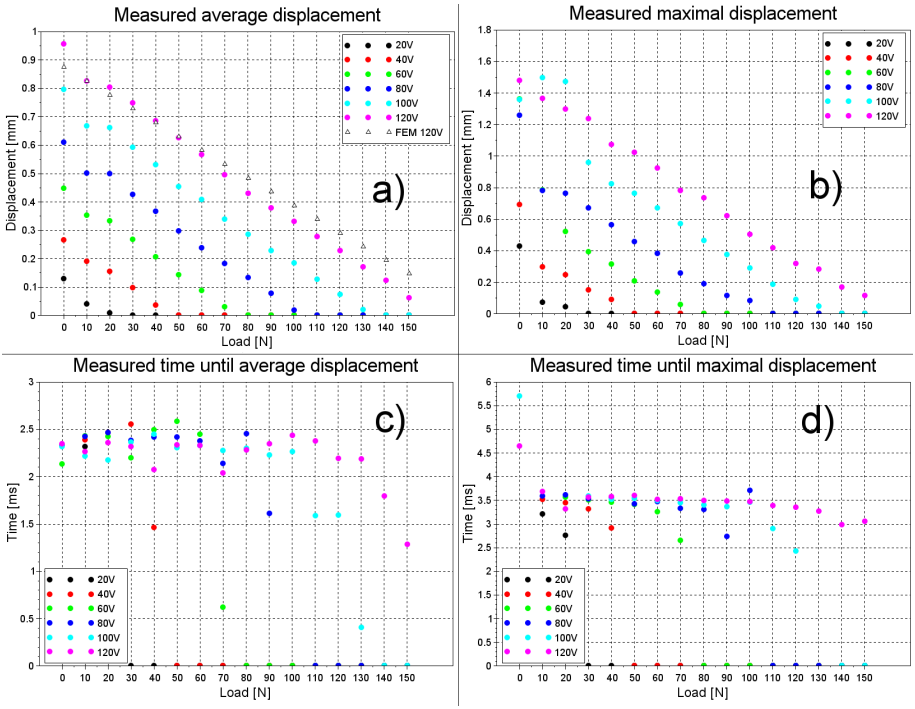

Figure 7.7: Results of the characterization of the test actuator

The movement can be modelled analytically using the equation of momentum for the system. For this, the blocking force F_B, the actuator stiffness k, the spring force F_S and the spring rate R are of importance, as well as the effective masses for both the actuator $m_{eff,act}$ and the spring $m_{eff,S}$ which form the

total mass of the system.

$$m_{tot} * \frac{\partial^2 x}{\partial t^2} = \underbrace{F_B - k * x}_{Actuator force} - \underbrace{F_S - R * x}_{Spring force} - \underbrace{dm * \frac{\partial x}{\partial t}}_{Dampening force} \tag{7.25}$$

This is rewritten to conform to the equation of motion for a dynamic system.

$$\frac{\partial^2 x}{\partial t^2} + \underbrace{\frac{dm}{m_{tot}}}_{2\delta} * \frac{\partial x}{\partial t} + \underbrace{\frac{k+R}{m_{tot}}}_{\omega^2} * x + \underbrace{\frac{F_S - F_B}{m_{tot}}}_{\epsilon} = 0 \tag{7.26}$$

Using the dampened Eigen frequency $\omega_d = \sqrt{\omega^2 - \delta^2}$ the differential equation 7.26 is solved.

$$x(t) = \frac{\epsilon}{\omega^2}(e^{-\delta * t} * cos(\omega_d * t) - 1) \tag{7.27}$$

Concerning the masses one has to consider that not the entire masses of both the spring and the actuator are accelerated. Since the displacement of the spring and the titanium frame increases linearly along their height, their effective mass can be derived from the energy equation and corresponds to one third of their inertial masses (see footnote 11). Concerning the PE stacks the effective mass depends on their location in the frame. In the case of the test actuator the PE pair in the upper rhomb performs almost the entire movement, while the middle pair accelerates only half the way and the lower pair moves one third of the full stroke. Hence, the total effective mass of the system can be calculated using the full masses of the spring m_S, the titanium frame m_F and one single PE stack m_P.

$$m_{tot} = \underbrace{\frac{m_S}{3}}_{m_{eff,S}} + \underbrace{\frac{m_F}{3} + 2m_P + \frac{2m_P}{2} + \frac{2m_P}{3}}_{m_{eff,act}} = \frac{m_S + m_F + 11m_P}{3} \tag{7.28}$$

For the test actuator the mass of the frame is $m_F = 70$ g and the mass of a single PE stack is $m_P = 28.44$ g which corresponds to a density of the ceramic material of 7.9 $\frac{\text{g}}{\text{cm}^3}$. The mass of the spring is $m_S = 68$ g. This adds up to a total effective mass of $m_{tot} = 150.28$ g.

Using Eq. 7.27 with the effective mass, the blocking force and the actuator

constant from the analytical model (Eq. 7.11 and Eq. 7.20 with 7.23 and 7.24), the spring rate of 1 $\frac{\mathrm{N}}{\mathrm{mm}}$ and a dampening coefficient of $dm = 30\,\frac{\mathrm{N\,s}}{\mathrm{m}}$ the dynamic behavior of the system can be modelled for various loads F_S. Fig. 7.8 shows a comparison between the measured movement of the test actuator and the model for a load of 30 N and a supply voltage of 120 V. The quasi-static displacement ($\frac{\epsilon}{\omega^2}$) and maximal displacements are closely aligned. This is the case for all loads and voltages proving that the actuator constant remains unaffected as the blocking force and load change. However, the eigenfrequency of the model is slightly off because the analytical model neglects the initial delay of the actuator of about 1 ms before it starts moving and it ignores the lateral oscillation of the spring which adds onto the transversal oscillation of the system. This leads to an error of the displacement times of about 0.8 ms. The displacement times remain constant though, which is in agreement with the findings displayed in Fig. 7.7c and Fig. 7.7d. This is due to the unaffected actuator constant and spring rate which determine the eigenfrequency. Taking the slight offset of the eigenfrequency into account the model is a useful tool to predict the dynamic behavior of the actuator.

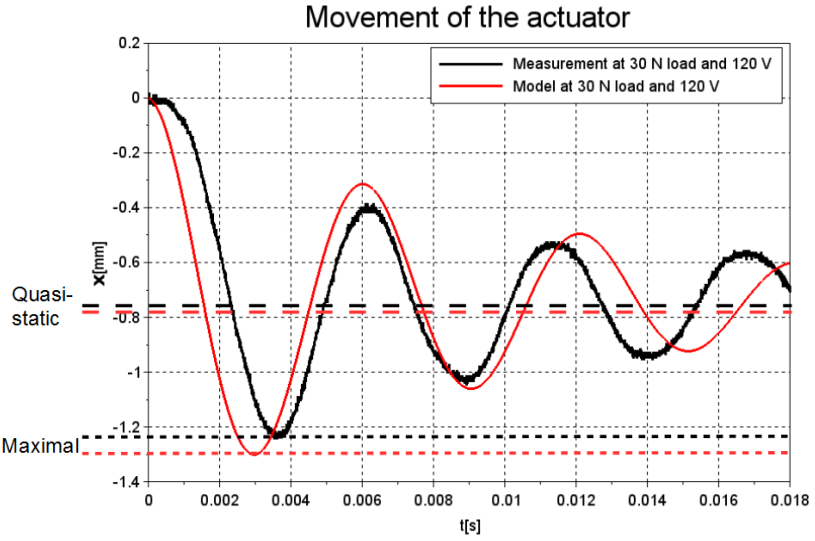

Figure 7.8: Movement of the test actuator compared with the analytical model

The FEM model was used to determine the maximal stress in the frame in order to investigate its durability. This was done using the material properties from the datasheet of the Ti Grade5. The frame is cut from a solid block of this material using a process called wire erosion, during which a charged brass wire cuts through the material by spark discharges. Since the frame has thin joints, it is possible that the high temperatures of the spark could alter the crystalline structure of the material resulting in different material properties. The effect of wire erosion on Ti Grade5 was investigated with tensile tests and metallographic images.

For the tensile tests three sample types were manufactured using geometries according to DIN50125. Sample type a) had a critical cross-sectional area of $24\,\mathrm{mm}^2$, sample type b) had $16\,\mathrm{mm}^2$ and sample type c) $12\,\mathrm{mm}^2$. All samples were wire eroded from one solid block to the geometry of type a). The types b) and c) were both eroded further or milled to reach the reduced cross-sectional areas. The samples were tested using a standard tensile test device with a maximal strength of 20 kN. Pneumatic pliers, which apply the closing force diagonally to the sample, were used to fix the sample in the machine. This allows increasing closing force as the sample is pulled. The elongation was measured by a position encoder with a reference length of 25 mm which was clamped onto the sample before the test cycle. The results of the tests are shown in figure 7.9. All samples show a good linear behavior up to an elongation of about 0.8 %. The corresponding E-modulus was measured to be between 102 MPa and 117 MPa, which is close to the literature value of 114 MPa. No dependency on the sample geometry or the manufacturing process could be found. The same is valid for the yield strength $\mathrm{R}_{p0.2}$ which was measured to be between 810 MPa and 850 MPa and the tensile strength R_m with values between 910 MPa and 950 MPa. Both the yield strength and the tensile strength are a bit below the literature values of 910 MPa for the yield strength and 1000 MPa for the tensile strength [96]. These deviations can be explained by plastic deformation of the samples within the pliers during the tests. This leads to the conclusion that the mechanical properties of the Ti Grade5 remain unaffected by the wire erosion manufacturing process. Due to the limited force of the tensile test machine, only the sample types b) and c)

could be destroyed (Fig. 7.9). The fracture area showed only little necking which is supported by the data in figure 7.9. A microscopic investigation of the fracture area indicated a brittle breach for both the milled and the wire eroded samples.

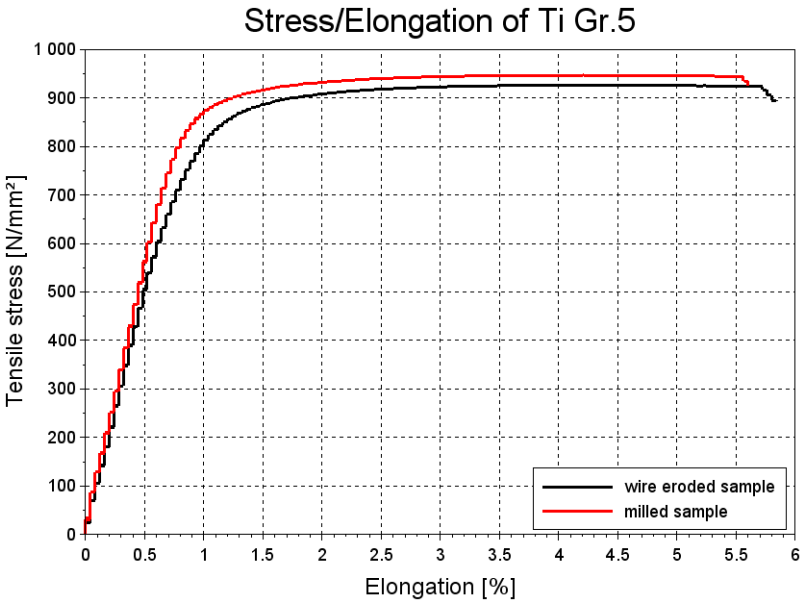

Figure 7.9: Results of tensile tests for a milled sample with 12 mm^2 and a wire eroded sample with 16 mm^2

Metallographic investigations were performed to evaluate the effects of wire erosion on the grain structure of Ti Grade5. Therefore, leftovers from the manufacturing of the frame for the test actuator were molded into a resin, sanded, polished and acid-treated using hydrofluoric acid. These samples were then examined with an electron microscope to determine the grain structure and an energy dispersive x-ray spectroscopy was performed to determine the chemical composition. The micrograph image (Fig 7.10) showed the typical lamellar grain structure which results from cooling down the beta-phase of Ti Grade5. However, the surface of the material is severely roughened. This surface layer has an average thickness of 15 µm. An intermediate layer between the surface layer and the bulk material can be seen clearly by its different

greyness. The intermediate layer has an average thickness of 8 µm indicating, that the thermal energy during the erosion process caused alterations of the material up to this depth.

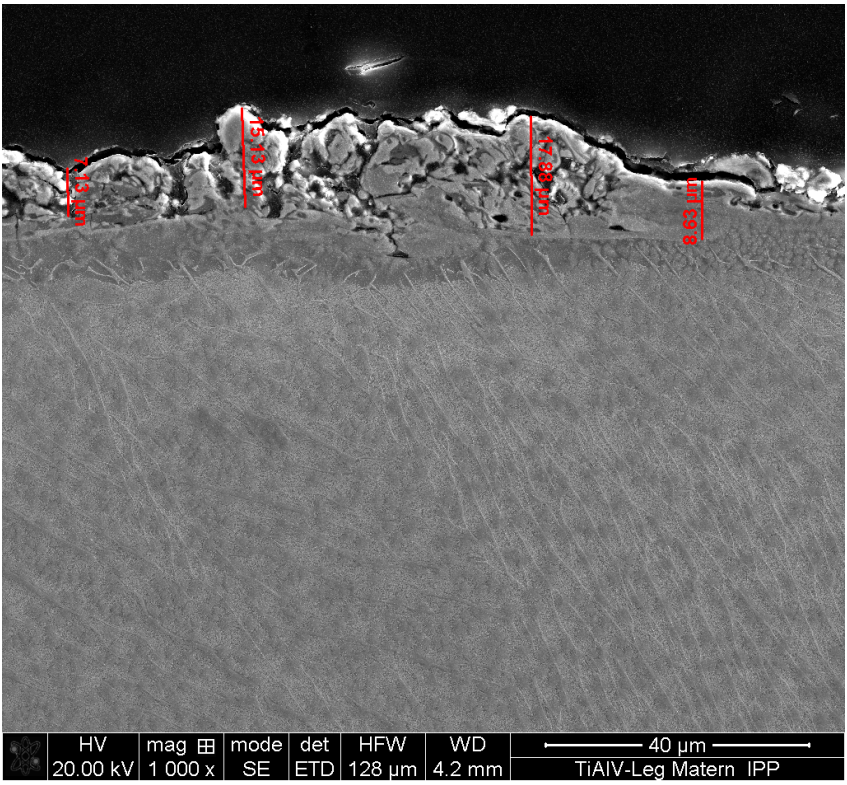

Figure 7.10: Image of a metallographic sample of wire eroded Ti Grade5 from the electron microscope

Energy dispersive x-ray spectroscopy (EDX) was used on the three layers to examine the chemical composition. The bulk material shows the expected spectrum which is dominated by titanium and vanadium with a smaller amount of aluminum. The intermediate layer shows a similar spectrum with an increased concentration of aluminum. This indicates a diffusion of aluminum into this layer by the large localized heat loads during the spark. The roughened top layer shows high concentrations of copper and zinc in addition

to the spectrum of the intermediate layer. This deposition is clearly a result of the wire erosion process as a brass wire is used for the spark erosion. Parts of the wire are transferred onto the surface of the material but do not diffuse deeper than a few micrometer. Hence, the brass contamination has no effect on the mechanical properties of the wire eroded material as the tensile tests already indicated.

Valve actuator

Based on the experiences gained from the test actuator the analytical model was used for the first draft of the valve actuator. Therefore, Eq. 7.11 with Eq. 7.10 were used to for the quasi-static displacement and Eq. 7.20 with Eq. 7.23 and 7.24 for the blocking force for leg angles between 1° and 45° and PE stack lengths between 2 mm and 72 mm. A frame with two serial rhombs was assumed with the leg geometry ext = 31 mm, d_0 = 0.5 mm, l = 2 mm, f = 2.8 mm, g_0 = 19 mm, i = 2 mm. From each displacement and blocking force, the actuator constant was calculated. This data was then used to estimate the actuator movement using Eq. 7.27 with the dampening coefficient dm = 30 $\frac{\mathrm{N\,s}}{\mathrm{m}}$ found with the test actuator, the spring rate from the bellow (R = 30 $\frac{\mathrm{N}}{\mathrm{mm}}$) and the spring force necessary to seal off the gas reservoir (100 N).

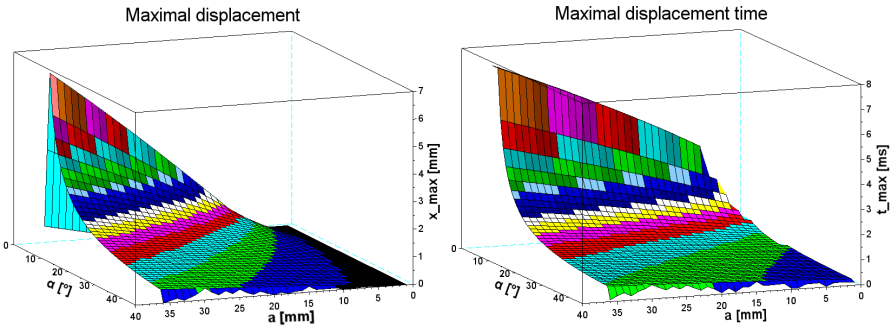

Figure 7.11: Analytic investigation for the maximal displacement and the maximal displacement time for different PE stack sizes and leg angles

Concerning the masses, the mass for the bellow was estimated according to the datasheet with 35 g, the mass of the valve plate with 11 g and the mass of

the valve stem with 6 g. The mass of the actuator was calculated according to the length of the PE stacks. From the dynamic calculation the values for the maximal displacement and the time to reach this maximal displacement were derived for each angle and stack length. The results are shown in Fig. 7.11. Both the maximal displacement and the displacement time decrease with increasing angle and decreasing stack length. As the actuator must generate a stroke of at least 2.05 mm within 3 ms or less, the results are scanned for which parameters both requirements are fulfilled. Figure 7.12 shows that the requirements are met for angles between 6° and 11° and for half stack lengths of 23 mm to 36 mm.

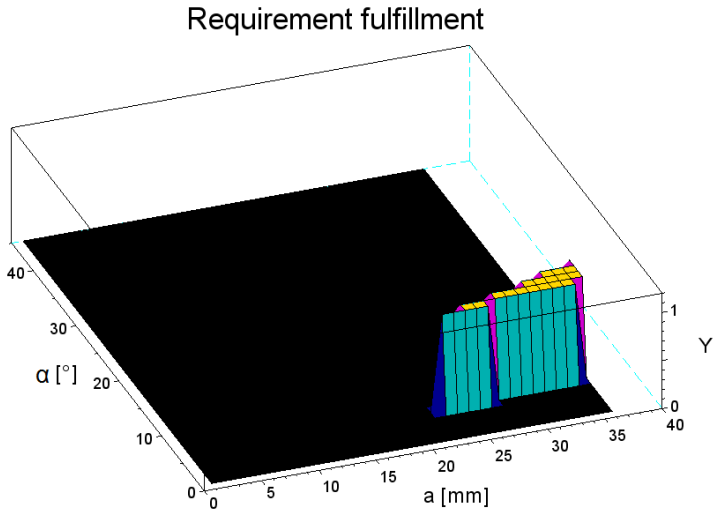

Figure 7.12: Scan at which parameters the requirements for opening time and stroke are fulfilled

The valve actuator was designed with two rhombs for PE stacks with a length of 64 mm, a leg angle of 7° and a leg geometry as described before. The dynamic properties of this assembly (max. displacement 2.7 mm, displ. time 2.8 ms) fit to the requirements with a reasonable safety margin. For the actual manufacturing geometry the pre-stressing force and the resulting elastic deformation during assembly have to be taken into account. A FEM model of the frame was used to determine the deformation for a pre-stressing force

of 150 N per PE stack. It was found that a leg angle of $\alpha^* = 7.5°$ leads to the right angle after assembly. To compensate for rough tolerances of the PE stacks the frame had to be deformed more than anticipated, resulting in a higher pre-stressing force and a leg angle of 6°. This decreases the performance of the actuator and should be corrected in a later version.

The actuator underwent the same testing procedure as the test actuator using the same tension spring. The load on the free end was increased stepwise from 0 N to 150 N in steps of 10 N and for each load supply voltages between 40 V and 200 V were applied either slowly for a quasi-static measurement or abruptly for the dynamic investigation. The movement was recorded by a laser distance meter and an oscilloscope. Multiple FEM simulations were conducted for comparison using the actual actuator geometry and the ideal geometry.

In the quasi-static case (Fig. 7.13a) the actuator shows the expected linear relation between load force and displacement for every supply voltage. The blocking force and the actuator stiffness are derived by the same procedure as with the test actuator. For the maximal supply voltage of 200 V the blocking force reaches a value of 310 N which corresponds to a stiffness of 150 $\frac{\mathrm{N}}{\mathrm{mm}}$. This stiffness remains constant for all supply voltages as the parallel characteristic lines indicate. The FEM model which takes the increased pre-stressing force and the lower leg angle into account fits nicely to the results of the measurement. It is clearly visible that the original geometry would have a slightly higher performance. The maximal displacements from the dynamic tests are about 60 % higher than the quasi-static displacements, as the results from the test actuator predicted. The same linear behavior can be seen (Fig. 7.13b) for each supply voltage. The time until the quasi-static displacement is reached is about 3.5 ms (Fig. 7.13c). For low supply voltages the values scatter at high load forces because the displacement is so low that the signal noise is of the order of the signals amplitude. The maximal displacement is reached after 5 ms to 7 ms with a slightly decreasing displacement time as the load is increased (Fig. 7.13d). The times are significantly longer than in the case of the test actuator which is mainly caused by a higher delay time. The larger stacks require more time to be fully charged due to their higher

electrical capacity. Furthermore, the mass of the actuator is severely higher than in the case of the test actuator. The valve actuator has a total mass of 641 g which increases the eigenfrequency significantly compared to the test actuator. This is a minor drawback with respect to the opening time of the valve but an advantage for the evacuation of the gas reservoir as the valve remains open longer before the swing back narrows the outflow cross-section.

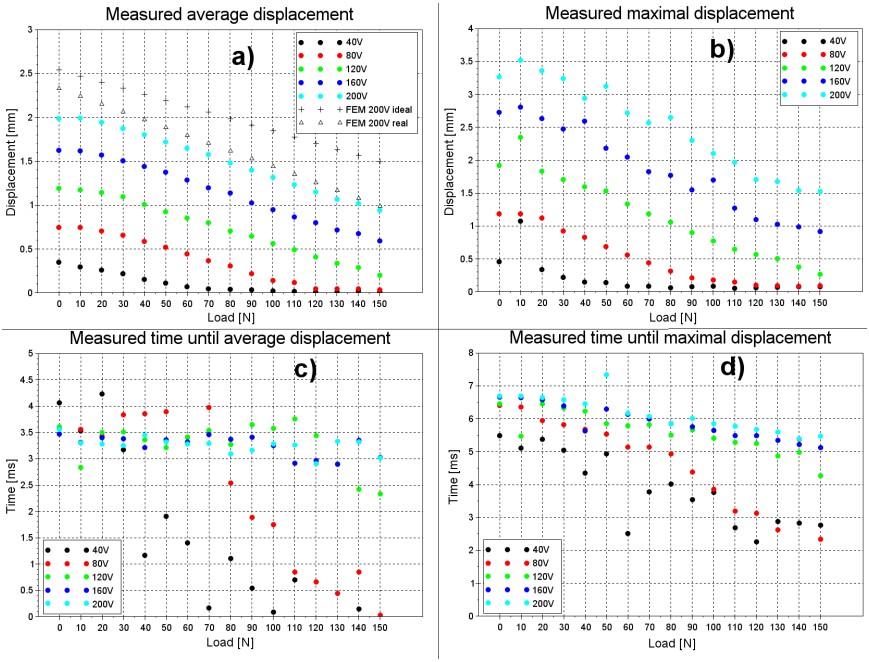

Figure 7.13: Results of the characterization of the valve actuator

7.2.2 Valve seal

The main valve seal is installed between the valve body and the nozzle flange. It serves as seal between the valve plate and the nozzle entrance as well as between the valve body and the nozzle flange. Therefore it is shaped as a flat ring with an outer diameter of 48 mm to fit in a standard CF40 flange. The inner diameter of 24 mm was chosen to fit to the hydraulic diameter of the bellow and the thickness of 2 mm resembles the thickness of a CF40

copper seal. The inner diameter allows the peak flow rate to be reached at a lift of 2 mm of the valve plate with the respective nozzle diameter of 14 mm. Additionally, the equality of the seals inner diameter and the bellows hydraulic diameter ensures, that the gas pressure in the reservoir produces no effective force on the valve plate. The seal is manufactured from a 2 mm viton plate by stamping. This procedure allows a precise cut and fast manufacturing. The valve is normally closed meaning that the conical edge of the valve plate is constantly pressed onto the sealing edge of the seal. The force is applied by compressing the bellow during assembly. It has to be large enough to guarantee leak tightness but low enough so the actuator can overcome it and produce the necessary stroke. For this purpose the leak rate was measured using a simple experimental setup (Appendix D). The tube was filled with helium at atmospheric pressure and the leak rate was recorded every 15 s over a time span of 30 min. This procedure was repeated for increasing force on the seal. For the acting force, the pressure force on the valve plate was added to the spring force. Between every measurement the viton seal was changed, the assembly cleaned with propanol and the leak detector recovered to a base leak rate of about $3 \times 10^{-11}\ \frac{\mathrm{Pa\,m^3}}{\mathrm{s}}$. New seals were necessary because the helium diffused into the viton and outgassed during the following measurement, altering the results. After the measurements with the new viton seals, the seals underwent an artificial aging process during which the valve plate was pressed into the seal and lifted again using a pneumatic piston. Every seal experienced 1000 cycles before the measurement procedure was repeated. Finally, all seals were baked at 150 °C for one week during which they remained tensed between two CF40 flanges. After cooling off, the seals underwent the same measurement procedure. The resulting progressions of the leak rates are displayed in Fig. 7.14.

For each force and seal condition the leak rate is below the required value of $1 \times 10^{-7}\ \frac{\mathrm{Pa\,m^3}}{\mathrm{s}}$ until 20 min after the start of the measurement. The low gradient of the leak rate indicates that the seal is not leaking but that diffusion through the viton is the dominant transport mechanism. This was confirmed by a measurement with a viton disc instead of a viton ring which showed a similar evolution of the leak rate. The force acting on the seal has a small

but visible influence on this transport with increasing leak rate as the force is reduced. This can be explained by the reduced area through which the helium can diffuse since the valve plate compresses the viton more at higher force. The condition of the seal has also a small but clear influence on the leak rate. The aged seal has a slightly higher leak rate compared to a new seal which is due to mechanical deterioration of the viton sealing edge. Microscopic gaps allow faster diffusion through the material. The baking increases the leak rate even further which leads to the conclusion that the viton does not recover by heating but loses a bit of its initial elasticity. This is also indicated by plastic deformation caused by the sealing edges of the CF40 flanges after baking.

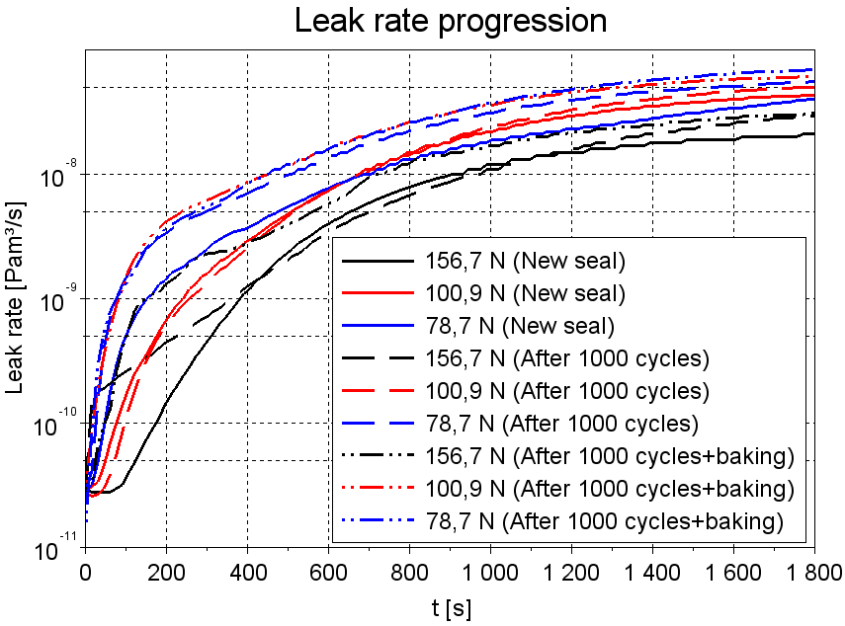

Figure 7.14: Comparison of leak rate progressions for 3 different forces on the seal at different seal conditions

From these measurements it was concluded that the viton seal can be used as main valve seal since the leak rate is below the required value for a long period of time. The diffusion through the viton has to be kept in mind when operating the valve with helium although it is expected that heavier gases like

neon or argon do not diffuse as quickly. During baking the valve plate has to be lifted from the seal to prevent plastic deformation and it is recommended to change the viton seal when possible due to wear.

7.2.3 Bellow

The bellow (Fig. 7.1 (3)) acts as spring to press the valve plate into the viton seal and relieves the valve plate from the gas pressure in the reservoir. The diameter of the bellow is limited by the diameter of the CF40 sealing edge and the head diameter of the M4 screws needed to fasten the bellow to the valve body. This leaves a maximum diameter of the bellow of 30 mm. A suitable bellow is the Witzenmann BAT 19,8x28x2x0,15 [91] with an effective area of 441 mm^2, which corresponds to the seal inner diameter of 24 mm. This type of bellow can withstand a maximal pressure of 5 MPa and is made of stainless steel 1.4571. The number of corrugations depends on the required spring force. In the leak rate experiment it was found that a force of 100 N is enough to ensure good leak tightness. It was chosen to manufacture the bellow with 19 corrugations which corresponds to a maximal axial deformation of 5.7 mm and a spring rate between 15.8 $\frac{N}{mm}$ and 29.4 $\frac{N}{mm}$. Using the maximal spring rate, the bellow has to be deformed 3.4 mm during assembly to achieve the necessary force on the seal. This leaves a free stroke of 2.3 mm which is sufficient for the valve operation. The total mass of the bellow is about 0.035 kg. The valve plate is welded directly to the bellow and a socket with a CF16 sealing edge is welded to the other end. This allows the use of a standard copper seal between the bellow and the valve body.

7.2.4 Nozzle

The nozzle flange (Fig. 7.1 (6)) is manufactured from a standard CF40 flange. A circular drilling with a diameter of 14 mm at the center of the flange serves as nozzle. This straight nozzle design was chosen based on the experience gained from the spring-driven valve. It allows the peak mass flow rate to be reached at a stroke of the valve plate of 2 mm with respect to the inlet diameter of 24 mm. This estimation was done using Eq. 6.3 to 6.6. Additionally, the

nozzle flange shields the viton seal from the plasmas radiation as there is no direct line of sight between plasma and seal. This is necessary to prevent high heat flux and radiative deterioration of the material.

7.2.5 Position detection

The position detection of the valve plate is important for the safe operation of the valve as it is the only mean to determine if the valve is open or closed once the valve is installed in the vacuum vessel. The gas reservoir may only be filled when the valve is closed to prevent uncontrolled flooding of the vessel. Since the bellow presses the valve plate into the viton seal, the valve is normally closed. Hence, it is sufficient to detect if the valve is open. Therefore, two stainless steel plates (8 mm x 20 mm x 0.1 mm), which are bended in the middle, are attached to the two cover plates. The thin plates are isolated from the cover plates by Kapton foil. The position of the thin plates is adjusted in such a way that the free ends of the plates are slightly below the upper rhomb of the titanium frame once the cover plates are installed (Fig. 7.15a). Using this arrangement, the titanium frame closes an electrical circuit between the two thin plates as the actuator is compressed (Fig. 7.15b). Hence, the actuator serves as a switch, which is closed when the valve is open. This information can be provided as a digital input for the control system.

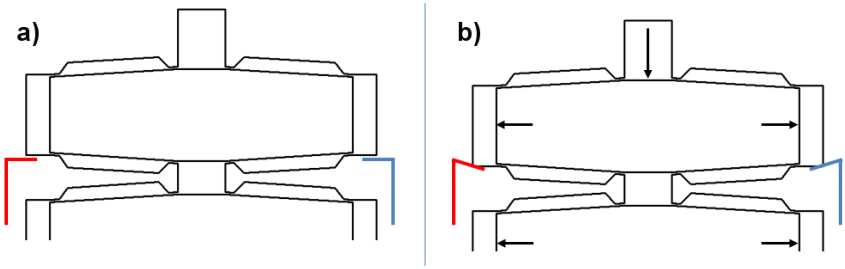

Figure 7.15: Switch for determining the open position of the valve: Valve is closed, switch is open (a), Valve is open, switch is closed (b)

7.2.6 Valve assembly

The valve is assembled from the major valve components described in sections 7.2.1 - 7.2.5. It can be split into five parts for fast and easy maintenance.

- The valve body with the side plates which holds the other components, the electric and gas feed through as well as the gas reservoir (Fig. 7.16 orange)
- The actuator consisting of the PE stacks and the titanium frame (Fig 7.16 blue)
- The bellow which holds the valve plate and the socket (Fig 7.16 green)
- The nozzle flange with the circular drilling which fastens the main valve seal to the valve body (Fig. 7.16 purple)
- The valve stem with the anchor which connects the valve plate to the actuator (Fig 7.16 red)

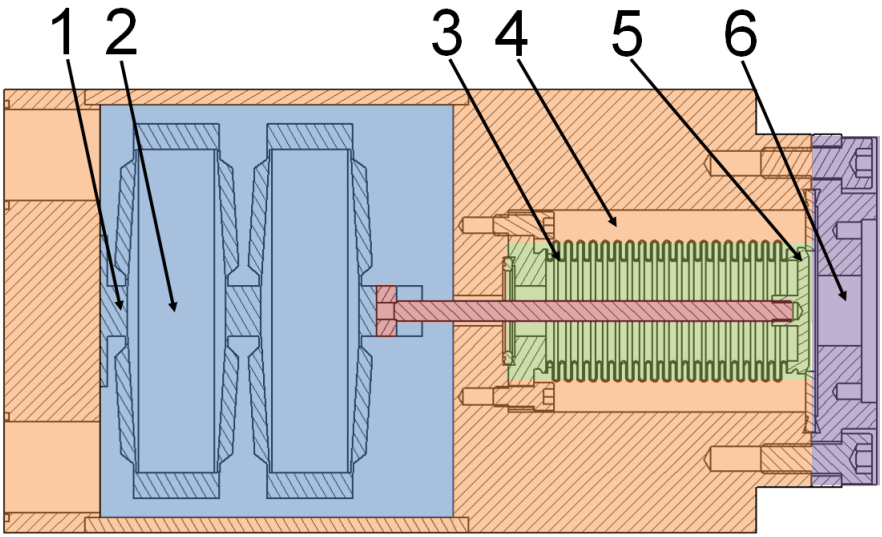

Figure 7.16: Assembled valve with colored components and numbered active parts consistent with figure 7.1

The valve body, which is manufactured from stainless steel, holds the valve components and the gas reservoir. It also serves as protection against ionizing radiation and mechanical impacts. The chamber for the actuator is a rectangular cavity which is wire eroded through the entire body so that the actuator can be slid in from either side. Sub-D connectors are welded into the bottom of the valve body allowing electrical throughput to the PE stacks. When the actuator is installed, the spacing is closed on both sides by 3 mm thick steel plates. As the actuator chamber is evacuated during operation, the plates contain small drillings and no sealing is applied between valve body and plates. The gas reservoir is a drilling with 40 mm diameter and 60 mm depth into the front of the body. A CF40 sealing edge is milled into the top which later holds the main valve seal and a CF16 sealing edge is milled onto the bottom of the gas reservoir allowing a gas tight sealing between the valve body and the socket of the bellow. A 6 mm wide drilling on the central axis serves as throughput for the valve stem. Hence, the inside of the bellow is evacuated as well which is important for the pressure relief of the valve plate. A 6 mm wide drilling parallel alongside the actuator chamber and a 4 mm drilling perpendicular entering the gas reservoir serve as gas feedthrough. After manufacturing, the 4 mm drilling is sealed by a welded cap and a VCR connector welded to the 6 mm drilling allows attachment of the gas line.

The bellow is installed into the gas reservoir of the valve body using a CF16 copper seal and 6 M4 screws. It has to be noted that the heads of the screws have to be milled to a diameter of 6 mm to fit between bellow and reservoir wall. When the main valve seal and the nozzle flange are fixed, the reservoir can be pressurized. If the valve leaks, the pre-stressing force by the bellow must be increased. Therefore the bellow is removed and stretched to achieve a small plastic deformation and to elongate the bellow.

The valve stem is a simple bolt with an M4 thread. The upper end of the bolt is screwed into the valve plate. The length of the bolt has to be adjusted as such, that the lower end of the bolt touches the bottom of spacing in the actuator frame. The anchor is then screwed onto the lower end of the bolt and the actuator is slid in from the side. When the actuator is fixed to the valve body, the anchor is turned until it firmly touches the top of spacing in

the frame. Hence the stem is fixed to the frame and the bellow.

Before the actuator is installed, the frame is electrically isolated using Kapton foil. This is a safety precaution to avoid short circuits should the PE stacks come in contact with the frame. The frame is slid into the actuator chamber and the wires for the PE actuators and the position detection are connected to the Sub-D connectors. The actuator is then fixed using two M6 screws which are fastened through two drillings in the bottom of the valve body. The two thin angled legs on the base of the titanium frame flatten as the screws are fastened and serve as pre-stressing springs to prevent unfastening of the M6 screws.

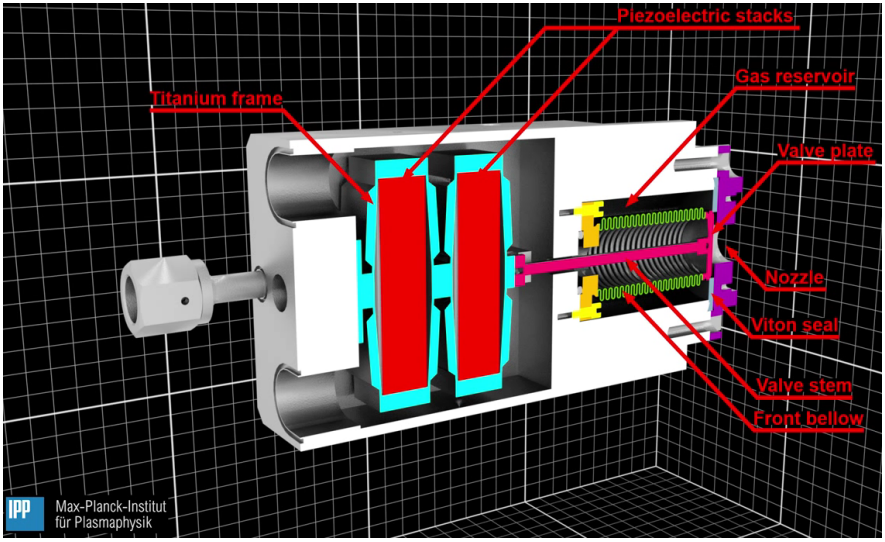

Figure 7.17: 3D model of the assembled piezo-driven valve

Chapter 8

Testing the valves

This chapter is dedicated to the description of the valve test bed and the tests conducted with the two valve types, including testing procedures and results. Opening time and stroke of the valves was measured, the outgassing behavior, the leak rates, the reliability and the gas flow properties.

8.1 Description of the test bed

As access to the valves is extremely limited once they are installed in the vacuum vessel, it is of upmost importance that they work reliably and meet the in-vessel requirements. To verify this, a series of tests was performed on the valves. These tests were primarily done in the valve test bed, which was specially designed for this purpose. The test bed vacuum conditions and temperature resembles closely the in-vessel conditions. However, magnetic fields of the order of 3 T and ionizing radiation, especially neutrons with energies in the MeV region, require immense technical effort and were therefore not considered for the test bed. As the valves from materials with a magnetic permeability coefficient smaller than 1.05 and the actuation principles do not generate magnetic fields, it is assumed that the external magnetic field has no influence on the valves performance. The radiation in ASDEX Upgrade had no noticeable effect on the old spring-driven valves and thus it is assumed

that the valves are resistant against ionizing radiation.

The test bed (Fig. 8.1) consists of two vacuum tanks (internal volumes 0.16 m^3 and 0.05 m^3) which are connected by a CF160 6-way cross (0.019 m^3). The large total volume ensures that the pressure in the tanks remains well below atmospheric pressure even when the maximal gas amount of 640 $Pa\,m^3$ is injected. This is important to protect the vessel and the vacuum pumps as neither is designed to withstand overpressure (bursting of vacuum vessel, destruction of turbo molecular pumps due to torque). A pneumatic shutter between the large tank and the cross allows the separation of the volumes. Hence, both volumes have to be pumped individually as the shutter can only be opened if both tanks are evacuated. The large tank and the cross are each equipped with a turbomolecular pump (TP). The TPs can also be disconnected from the tanks using pneumatic shutters. A bypass tube connects the small tank with the outlets of the TPs and goes to a large sliding vane rotary vacuum pump which generates the low level vacuum. The connections of the bypass line to the small tank and the TPs can be sealed off by pneumatic angle valves.

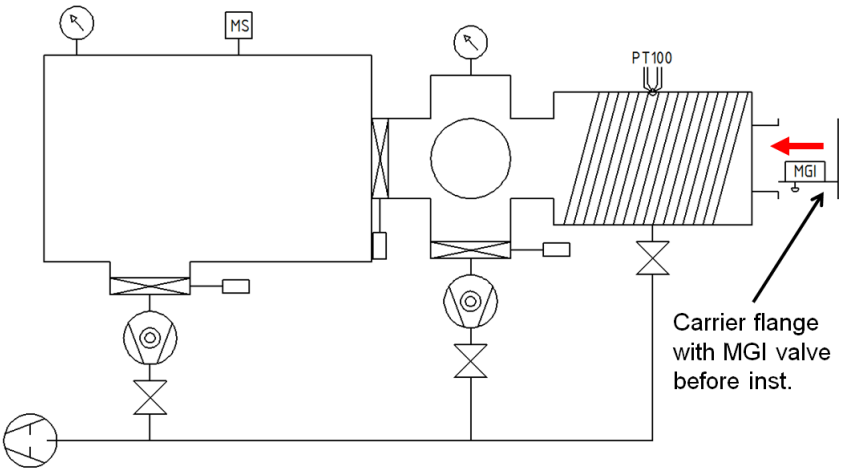

Figure 8.1: Scheme of the valve test bed vacuum system

Since the two volumes of the test bed can be pumped individually, each tank is equipped with a vacuum gauge. These gauges are combined Pirani/Cold cathode with digital output. They have the advantage that they can measure pressures between 100 kPa and 1×10^{-7} Pa very precisely, which is important to measure the vessel pressure when the valves release their gas into the tanks. This allows monitoring whether the valves blow off their gas completely. Furthermore, the output signal can be directly forwarded to the control system by Profibus connection. However, the gauges have to switch the measurement principle from cold cathode to Pirani as the pressure increases and the maximal data output frequency is 100 Hz, which makes the measurement too slow for the analysis of the actual pressure increase during gas injection. A quadrupole mass spectrometer (MS) is attached to the large tank, which is used for leak check and outgassing experiments. During gas injection the MS has to be shut down to protect its hot filaments. Its operation is only possible below pressures of 1×10^{-4} Pa. The smaller tank can be heated up to 165 °C and is therefore equipped with a PT100 temperature sensor. A four-wire measurement is used to compensate for electrical resistivity in the wires and the connector. The sensor is used for monitoring only since an integrated thermocouple regulates the heating power.

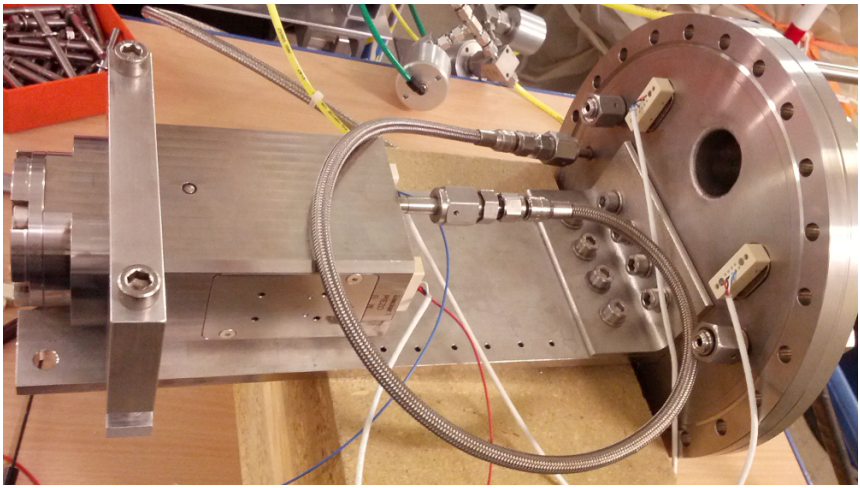

Figure 8.2: Carrier flange with the piezo-driven MGI valve

The MGI valve is mounted to a steel plate which is fixed to a CF200 flange perpendicular to each other (Fig. 8.2). The flange serves as throughput for the electrical and gas supplies by two Sub-D 9-pin and two Sub-D 15-pin connectors, as well as three VCR throughputs. The flange is connected to the rear end of the small tank with the MGI valve inside the small volume. As the assembly of carrier flange and MGI valve has a weight of roughly 20 kg, the steel plate is equipped with a support beneath the MGI valve. This simplifies the installation of the assembly into the tank as the support, which is shaped like a semi-sphere and made from brass, slides along the inner wall of tank as the flange is positioned.

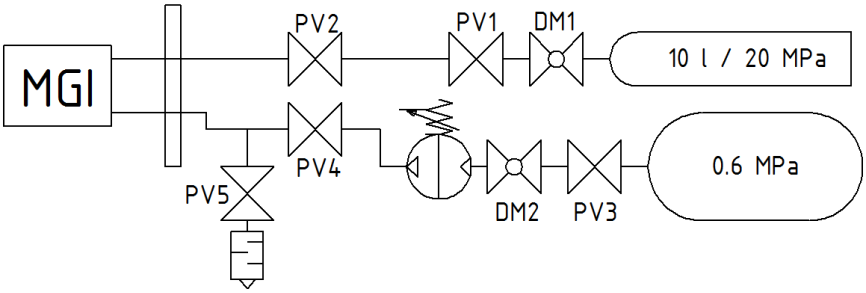

Figure 8.3: Scheme of the gas supply system for the valve test bed

The gas supply for the test bed (Fig. 8.3) is designed to support both the spring-driven and the piezo-driven valve. Hence it is equipped with a gas line for test gas (He, Ne, Ar) and pressurized air. The test gas is taken from a 10 l gas bottle with an attached pressure regulator (DM1). From there the gas line passes through two pneumatic valves (PV1, PV2) which serve as safety valves to prevent flooding of the vacuum tanks. After the second safety valve, the gas line enters the carrier flange and runs to the valve. The pressurized air is taken from the laboratory 0.6 MPa air supply system and routed into the valve system of the Simatic control system (PV3). From there the air line goes through a pressure regulator (DM2) and into a pressure booster. The booster mechanically amplifies the air pressure by a factor of 4. Using the pressure regulator, air pressures between 0.1 MPa and 2.4 MPa can be applied to the MGI valve. After the pressure booster, the air line runs through a pneumatic

valve (PV4), which serves as safety valve, before entering the carrier flange and the MGI valve. A pneumatic valve (PV5) between the safety valve and the flange is used to vent the pressurized air from the MGI valve.

The control system for the pneumatic valves and the MGI valves consists of a S7 CPU and an ET200S external periphery with digital I/O converters, analogue input and the valve system. The digital inputs are used for the position indicators of the shutters and the pneumatic valves, the digital outputs give the trigger signals to the automated control circuits for the valves described in Appendix C.2 and C.4 and for the relays controlling the heating system. The analogue input converts the signal from the PT100 temperature sensor and the valve system controls the shutters and the pneumatic valves in addition the pressurized air supply for the MGI valve. CPU, ET200S and the pressure gauges are all connected by a Profibus system.

The small vacuum tank is heated by a wire with high electrical resistivity. The wire is welded to the stainless steel hull of the tank in meanders and is covered by 40 mm of Styrofoam which serves as isolation. A secondary sheet of stainless steel with a thickness of 1 mm protects the isolation and prevents direct contact with heated parts. The heating wire is connected to the 220 V power supply over a relays which is switched by the control system. When the relay is closed, heating starts immediately as shown in figure 8.4.

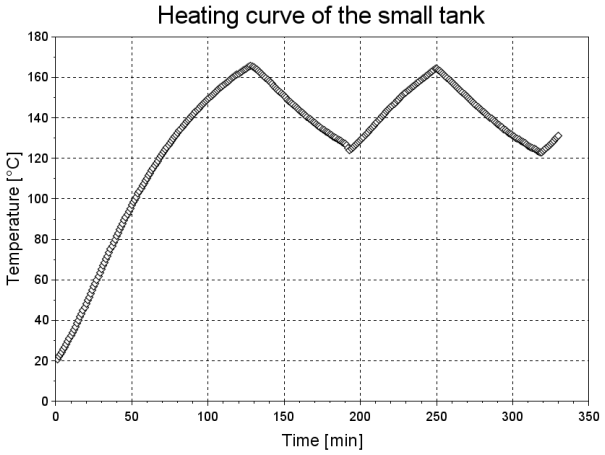

Figure 8.4: Heating curve of the small tank

The temperature increases quite constantly over 130 minutes from room temperature up to 165 °C. Then the thermocouple opens the heating circuit, cutting off the power and the temperature drops over 60 minutes to 123 °C. At this value, the thermocouple closes the heating circuit again and the temperature rises within 60 minutes to its peak value. Although the temperature changes are slow, the low heat conductivity in vacuum prevents the valve from following the heating curve of the tank. Hence, over a time of 24 hours the average temperature of the valve was measured at 145 °C with slight oscillations resembling to the heating curve.

8.2 Valve tests

The following sections contain the tests that were performed with the two valve types. Each valve was subdued to the same tests to allow a comparison. Furthermore, the valves had to complete the tests successfully to be installed into ASDEX Upgrade. It had to be ensured, that the valves are compatible with the in-vessel conditions. Information about opening time and stroke are also important for the evaluation of disruption mitigation experiments and had to be gathered beforehand. Reliability had to be proven as the valves operate over several months without maintenance and the compatibility with UHV conditions and baking temperature had to be investigated to allow installation into the vacuum vessel.

8.2.1 Opening time and stroke

The opening time and the stroke are highly important because only a sufficiently short opening time allows injection during the pre-TQ phase and a sufficiently large stroke is necessary to achieve the peak flow rate during this phase. This test was conducted outside the test bed under atmospheric conditions. The vacuum vessel was flooded and the carrier flange was extracted. The MGI valve was fixed to the steel plate of the flange and this assembly was firmly fastened on a rigid surface. The fast laser displacement sensor was fixed to the same surface to prevent any movement between assembly and

sensor. The laser was pointed through the nozzle onto the valve plate. The analogue signal of the displacement sensor was recorded by a fast oscilloscope as soon as the valve was triggered by the manual trigger circuit (Appendix C.1 for spring-driven valve or C.3 for piezo-driven valve). The signal of the displacement sensor is calibrated to $1\,\frac{\mathrm{V}}{\mathrm{mm}}$. Hence, the signal range (0-10 V) from the position detector was calibrated using the signal of the sensor. With this setup, the tests were performed for each MGI valve.

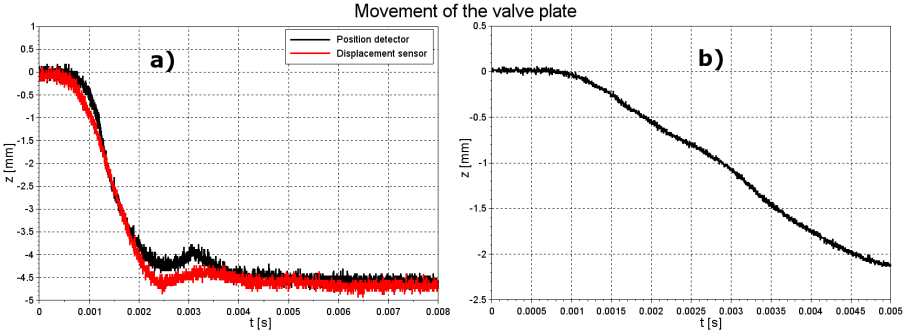

Figure 8.5: Calibrated signals of the laser displacement sensor for the spring-driven valve (a) and piezo-driven valve (b)

For the spring-driven valve (Fig. 8.5a), the signal of the position detector was also recorded and scaled to fit with the displacement sensor. The time traces of both signals are in good agreement. The onset of the plate movement is about 1 ms after the piezo stacks are discharged. This delay is due to the inertia of the stacks, the stem and the spring unit. The maximum stroke of 4.5 mm is reached after 2.7 ms, indicating a mean velocity of the valve plate of $1.67\,\frac{\mathrm{m}}{\mathrm{s}}$. The critical stroke of 2.11 mm is reached after 1.5 ms after which the flow rate is limited by the cross-sectional area of the nozzle. The motion can be described as linear between 1 ms and 2 ms, corresponding to a constant velocity during the opening. The valve plate bounces back about 0.5 mm after 3 ms. This bouncing has no influence on the mass flow rate since the stroke is not reduced below the critical stroke. Hence, the valve fulfills the requirements concerning opening time and stroke and the position detector works properly and is calibrated.

In the case of the piezo-driven valve, the movement of the valve plate (Fig. 8.5b) starts with a delay of about 1 ms. This is due to the large electric capacity of the PE stacks which have to reach a certain charge to overcome the spring force of the bellow. After that delay time, the valve plate performs a nearly linear motion over 4 ms until it reaches its maximal displacement of 2.2 mm. The necessary stroke of 2 mm is achieved after 4.5 ms which means that the effective opening time of the valve is 3.5 ms. This fits to the analytical model used to design the actuator, taking the non-ideal geometry of the frame into account. The performance of the valve concerning opening time and stroke is sufficient to be used for MGI experiments although it could be increased by adjusting the actuator frame.

8.2.2 Outgassing

An outgassing test is of great importance for all in-vessel components in a Tokamak. The quality of the insulating vacuum strongly depends on the outgassing rate of the parts and the plasma quality depends on the species which outgas. Plasma discharges may not be initiated if species with high atomic mass number outgas due to their massive radiative power. The outgassing behavior of the MGI valves was first investigated in the test bed. The vacuum vessel of the test bed was evacuated until a background pressure of 10^{-4} Pa was reached. At this point, the quadrupole mass spectrometer was activated and the background spectrum was measured. After this measurement, the MS was deactivated and the vessel was flooded with nitrogen. The carrier flange with the MGI valve and a PT100 sensor were placed in the vessel and the evacuation procedure was repeated. When the necessary background pressure was reached, the heating system was activated. The valve was heated up until it reached 150 °C. At this point, the second measurement of the mass spectrum was performed using the MS. This testing procedure was performed under the assumption, that the flooding of the vessel with nitrogen would not change the background spectrum. The results shown in Fig. 8.6 were achieved in a dedicated test bed which used the same testing procedure.

The outgassing spectrum of the spring-driven valve (Fig. 8.6a) shows increased partial pressures at masses of 28 and 32 which correspond to nitrogen and oxygen, indicating that air is leaking from the valve body. However, the partial pressures are of the order of 1×10^{-9} Pa which is no issue for the torus vacuum. The peak at mass 18 which corresponds to water is slightly higher than the background but also of a non-problematic order. There are no significant partial pressures above masses of 45 which would show outgassing hydrocarbons. Hence, the outgassing of the valve is in acceptable margins and the valve is fit for in-vessel operation.

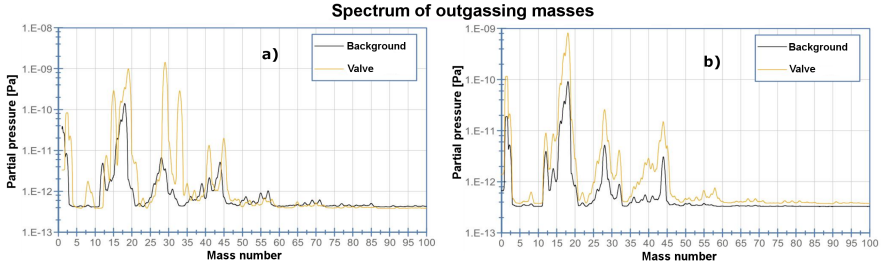

Figure 8.6: Mass spectra of the background and with heated valves for the spring-driven valve (a) and the piezo-driven valve (b)

The outgassing spectrum of the piezo-driven valve (Fig. 8.6b) shows increased partial pressures for masses 1, 2 and 18 compared to the background which correspond to hydrogen and water. This is a normal behavior during baking and the peak partial pressure of 1×10^{-9} Pa does not pose a problem for the torus vacuum. Small increases are also visible at masses 28 and 32 which correspond to nitrogen and oxygen. In this case leakage is not the origin of these air components since the entire valve was pumped. The partial pressures indicate outgassing as the source of these elements. A clear increase is seen for masses between 36 and 44 which come from light alcohols that were used to clean the valve before baking. They are volatile and evaporate during baking. No significant amounts of elements above a mass number of 45 could be detected. Hence the valve is fit to be installed into the vacuum vessel with respect to its outgassing behavior.

8.2.3 Leak rate

The leak rate of the valves has to be determined to allow in-vessel installation. If the leakage exceeds $1 \times 10^{-8} \frac{\mathrm{Pa\,m^3}}{\mathrm{s}}$ the valves would deteriorate the torus vacuum and no plasma could be initiated. A first leak rate test was performed in the test bed for all valves. Therefore, each valve was placed in the vacuum vessel using the carrier flange. The vessel was evacuated until the necessary pressure of 10^{-4} Pa was reached and the MS was activated. The chambers of the MGI valves (spring-driven valve: gas reservoir, piezo chamber, rear reservoir; piezo-driven valve: gas reservoir) were filled with helium at a total pressure of 0.2 MPa. The increase in helium concentration in the vessel was observed over 15 minutes using the MS. For the spring-driven valve, leak rates between $1.5 \times 10^{-10} \frac{\mathrm{Pa\,m^3}}{\mathrm{s}}$ and $2.9 \times 10^{-10} \frac{\mathrm{Pa\,m^3}}{\mathrm{s}}$ and for the piezo-driven valve a leak rate of $6.8 \times 10^{-11} \frac{\mathrm{Pa\,m^3}}{\mathrm{s}}$ was measured. After this first measurement, the valves were heated up to 150 °C. During this baking, the valves gas reservoirs were opened to protect the viton seal. Thus only the rear reservoir and the piezo chamber of the spring-driven valve were filled with helium and checked for leak tightness. The leak rate increased slightly to values between $4.1 \times 10^{-10} \frac{\mathrm{Pa\,m^3}}{\mathrm{s}}$ and $4.8 \times 10^{-10} \frac{\mathrm{Pa\,m^3}}{\mathrm{s}}$. Finally, after cool down, the valves were closed again and the helium pressure was applied to all volumes. The leak rates returned to their initial values. This indicates that the thermal expansion of the components leads to a small deformation which influences the leak tightness of the gold wire seals in the spring-driven valve. However, as the leak rates were within acceptable margins, the valves were evaluated as leak tight and fit to be installed into ASDEX Upgrade. When compared to the results obtained with the test device (Fig. 7.14), it can be seen that the leak rate of the valves are lower. This indicates that the force pressing the valve plate into the seal is higher than in the test device. Furthermore, the surface quality of the valve plates is higher as they are made from polished stainless steel while the test device used normal steel that was milled.

8.2.4 Reliability

Durability tests for the valves were designed to mimic the stress that the valve undergoes during an experimental campaign at ASDEX Upgrade. The tests were carried out in the valve test bed. Each valve was mounted in the vessel using the carrier flange and the vessel was evacuated to a pressure of 10^{-4} Pa. The STEP 7 program for the respective valve was activated (Appendix B).
In the case of the spring-driven valve, the testing cycle went as follows. First, the pneumatic shutters and corner valves were closed to protect the turbo molecular pumps. When the shutters and corner valves were closed, the pneumatic valves PV3 and PV4 (Fig. 8.3) were opened and PV5 was closed. By this the spring-driven valve was closed. After 30 s the PE stack were charged and 4 s later PV4 was closed and PV5 was opened to vent the air from the rear reservoir. In the next step, the valves PV1 and PV2 were opened for 2 s to fill the gas reservoir with 0.5 MPa of argon. The gas rested 5 s in the reservoir before the valve was triggered and the gas was released into the vessel, increasing the pressure to roughly 100 Pa. After another 7 s the corner valve to the bypass line was opened and the vessel was evacuated. When the pressure had dropped below 9 Pa, the shutters and corner valves of the TPs were opened and the vessel was evacuated until the pressure reached 10^{-4} Pa and the cycle was repeated.
For the piezo-driven valve, the procedure was a bit different. The pneumatic shutters and corner valves were closed for protecting the turbo molecular pumps. When all was closed, the pneumatic valves PV1 and PV2 were opened for 2 s to fill the gas reservoir with 0.5 MPa of argon. Another 5 s later, the PE stacks were charged for 2 s, opening the valve and releasing the gas into the vessel. This increased the pressure to roughly 30 Pa. The bypass was opened 1 s after the valve was closed again. As soon as the pressure reached 12 Pa, the shutters and corner valves were opened again, pumping the vessel until a pressure of 10^{-4} Pa was reached and the cycle was repeated. From the data of previous years it was concluded that the valve performs about 1000 operational cycles between maintenance breaks. Therefore, each valve underwent 1000 cycles before being removed from the test bed. The baking

took place in a separate oven. After baking at 150 °C for 7 days, the valves were reinstalled into the test bed to perform another 1000 cycles as described before. The vacuum pressure was recorded to verify that no gas leaked out of the valve at any time.

Both valves passed the durability test without a change in leak rate and performance. Hence the valves are suitable for operation in ASDEX Upgrade with respect to reliability. The viton seal of the spring-driven valve showed signs of deterioration though, as the sealing edge, which was sharp at the beginning, was visibly worn out (Fig. 8.7). The dark area in figure 8.7b is viton which has been scraped off from the top of the seal and pressed between the nozzle flange and the valve plate. However, this deterioration had no negative effect on the leak rate. This deterioration was not observed at the seal of the piezo-driven valve. Thus, this effect is likely due to the higher force at which the valve plate of the spring-driven valve is pressed into the seal.

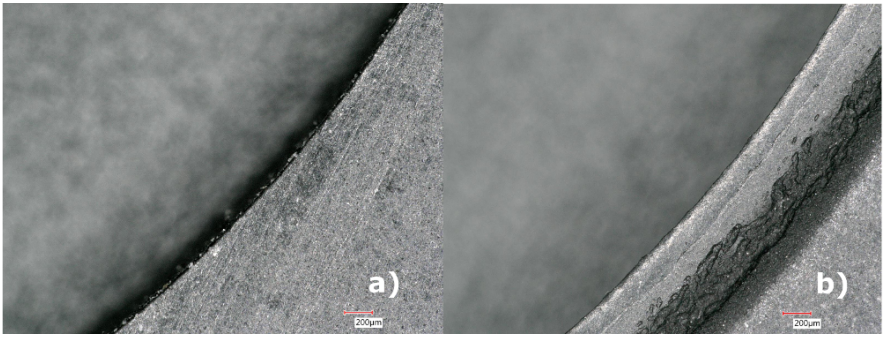

Figure 8.7: New viton seal with sharp sealing edge (a) and seal after 1000 operational cycles with worn out sealing edge (b)

8.2.5 Gas flow

Knowledge of the flow of the gas from the reservoir through the nozzle into the vacuum is highly important for disruption mitigation experiments. The mass flow gives a good estimate of how many particles reach the plasma within a given time, a high flow velocity allows precise injection into the different phases of a disruption and the geometry of the gas cloud gives information

where the highest cooling at the plasma edge takes place. To acquire this data, computational fluid dynamic (CFD) simulations were performed for both valves before measuring the gas cloud experimentally.

In the CFD simulations, different nozzle geometries were investigated in an effort to optimize the mass flow rate and the gas velocity to highest values. Further the simulations were used to check the analytical approach described in section 6.2.6. The simulations were made with ANSYS Fluent using a 2D axisymmetric model of the gas reservoir, nozzle and vacuum space. This 2D model was chosen over the actual 3D geometry to save computing time and modelling effort, allowing the investigation of multiple nozzle geometries. The axisymmetric model was designed to represent the correct dimensions for the gas reservoir (128 cm^3 or 42 cm^3), the stem and the nozzles inlet and outlet diameters, as well as the nozzle contour, while neglecting small features like the corrugations of the bellow, screws and small edges.

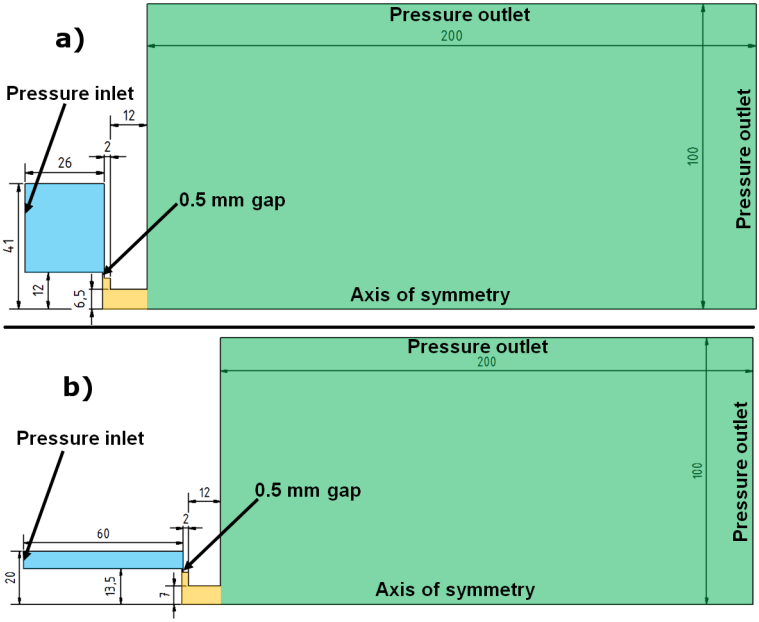

Figure 8.8: 2D axisymmetric models of the flow domain with gas reservoir (blue), straight nozzle (orange) and vacuum space (green) for the spring-driven valve (a) and the piezo-driven valve (b)

Figure 8.8 illustrates the 2D axisymmetric models with a straight nozzle. The pressure inlet boundary condition is located at the far left wall of the gas reservoir, while the pressure outlets are set at the far right and top boundaries of the vacuum space. The nozzle axis is used as rotational axis. Each model contains an artificial leak between the valve plate and the main seal. This gap is 0.5 mm wide and is necessary to generate a continuous flow domain.
In the next step the models are meshed with a regular mesh using squares with and edge length of 0.5 mm. This meshing technique is ideal for this case since the model has rectangular corners. Only the gap has to have a refined mesh, because the moving stem deforms the cells in this area. To keep the angles and sizes of these deformed cells reasonable, the mesh was refined by a factor of 2 in this region.
The setup of the solver was done under the assumption that the flow would be supersonic. Hence, a transient density based solver was chosen to solve the Reynolds-averaged Navier-Stokes equations and the energy equation. The flow model was set to be inviscid, which is valid for supersonic flows. This allows neglecting turbulence, thus saving computing time. Argon with ideal gas properties was chosen for all simulations. Although mass flow rate and gas velocity depend on the gas species, trends should remain similar for different gases. The wall material was set to be aluminum since the wall material has very little influence on the flow on such short time scales. The pressure inlet boundary was set to the desired reservoir pressure and the pressure outlet boundaries were set to 0.0001 Pa. It has to be noted that the Navier-Stokes equations are only valid above the molecular flow regime. It was found that 0.0001 Pa was the lowest acceptable pressure. However, the bulk flow is dominated by viscous flow allowing application of the Navier-Stokes equations. The movement of the valve plate was programmed to resemble the measured movements described in section 8.2.1. For the spring-driven valve, the valve plate was set to move linearly with $2\,\frac{\mathrm{m}}{\mathrm{s}}$, starting with the onset of the simulation over a time of 2 ms. In the case of the piezo-driven valve, the plate was set to move linear with a speed of $0.66\,\frac{\mathrm{m}}{\mathrm{s}}$ within the first 3.5 ms and then return with the same speed in opposite direction over the same time. During the movement the mesh would be deformed like an elastic solid with a Pois-

son's ratio of 0.45. After the first time step of the simulation the pressure inlet boundary would change to a wall boundary to prevent more gas filling the reservoir. An implicit formulation was chosen for the Navier-Stokes equations, which allows larger time steps while remaining stable. The flow domain was initialized with the hybrid model up to a residual of 10^{-8}. This hybrid initialization smoothens the pressure distribution of the entire flow domain. This has the drawback that some gas is already in the nozzle at the onset of the simulation. However, the stability of the simulation is increased tremendously. The width of the time steps was set to be 5×10^{-7} s which amounts to a courant number of 0.6. This means that the computation is stable for the implicit Euler formulation. The number of time steps was set to be 20000 which corresponds to a total simulated flow time of 10 ms. The iterations for each time step would be stopped as soon as the residuals of the velocity, energy and continuity equations dropped below 10^{-3}.
The first series of tests was aimed at investigating different nozzle geometries concerning the achievable mass flow rate and gas velocity. For this task, the only the model of the spring-driven valve was used. The reservoir was filled with argon at a pressure of 5 MPa before the valve opened. The results are shown in Fig. 8.9. It can be seen, that the peak gas velocity (blue) is rather uninfluenced by the geometry. This is in agreement with the velocity limit of gas in vacuum, which can be estimated by Eq. 8.1 [97].

$$U_{lim} = \sqrt{\frac{2\gamma}{\gamma - 1} * R_s * T_0} \tag{8.1}$$

The mass flow rate is mainly determined by the critical flow cross-section. However, only the convergent and straight nozzles in Fig. 8.9 guarantee no direct line of sight between the plasma and the viton seal. The other geometries can be scaled to fulfill this requirement, but the mass flow rate would be the same as for the straight nozzle. Hence, the additional manufacturing effort for adjusted nozzles is not compensated by favorable flow conditions. Hence, the design for both valve types was focused on the straight nozzle.

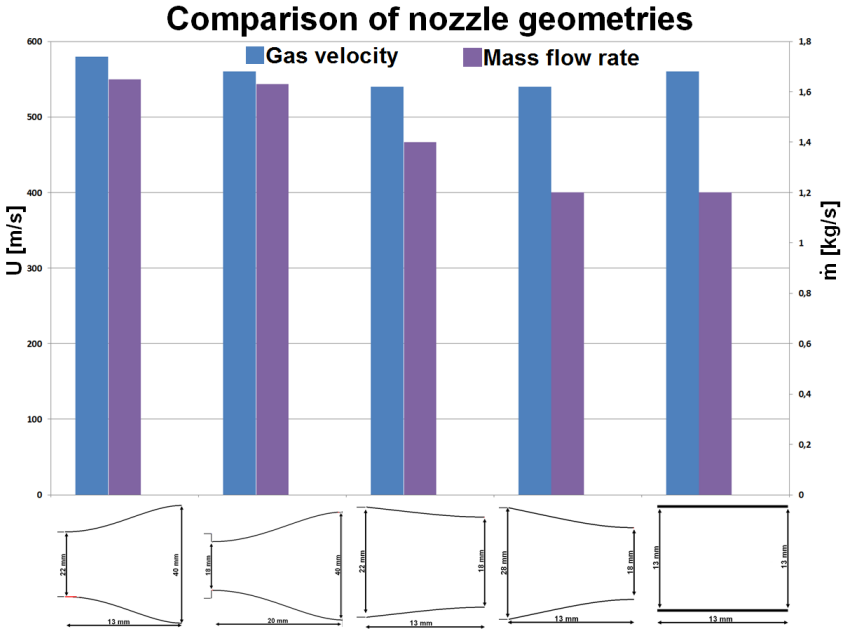

Figure 8.9: Comparison between divergent, convergent and straight nozzle geometries with respect to peak gas velocity and peak mass flow rate

Further simulations were done for both the spring-driven valve and the piezo-driven valve with reservoir pressures of 5 MPa and the simulation properties and flow domains as described before. The results of the simulation concerning mass flow rate and reservoir pressure where compared to the results of the analytical model described in section 6.2.6 with an initial reservoir pressure of 5 MPa and an initial mass flow rate of zero. The time traces are shown in Fig. 8.10.

For the spring-driven valve (Fig. 8.10a), both mass flow rates peak at 1 ms which is the time when the critical cross-section switches its location from the valve plate into the nozzle. The peak value of the CFD simulation is about 25 % smaller than the value of the analytical model. This is due to neglected velocity and temperature profiles in the ideal model, as well as a Mach number slightly above one in the critical cross-section of the simulation. The peak in the simulated mass flow rate after 0.3 ms is due to the hybrid initialization of

the simulation, which distributed some gas into the nozzle. The initial mass flow rate is zero but rises up rapidly until the gas is vented from the nozzle. This is also visible in the time trace of the simulated reservoir pressure, which drops faster in the beginning than the ideal model predicts. However, the evacuation time of roughly 10 ms is identical for both model and simulation.

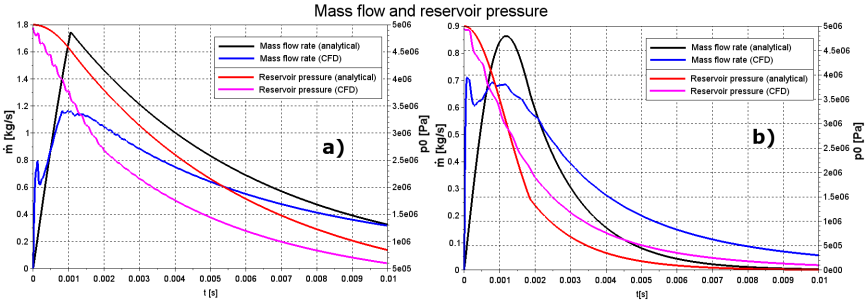

Figure 8.10: Comparison between the analytical model and the CFD simulation concerning mass flow rate and reservoir pressure for the spring-driven valve (a) and the piezo-driven valve (b)

In the case of the piezo-driven valve (Fig. 8.10b), the pressure curves of the simulation and the model are well aligned. The evacuation time of the reservoir (10 % of the initial pressure) is reached after 3.5 ms in the case of the analytical model and after 5 ms for the simulation. This shows that the swing back of the actuator does not influence the evacuation of the reservoir.
The mass flow rate peaks at 1 ms with a peak value of 0.7 $\frac{\text{kg}}{\text{s}}$ for the simulation and at 1.2 ms with a peak value of 0.85 $\frac{\text{kg}}{\text{s}}$ in the case of the analytical model. Hence, the peak times are reasonable well aligned but the peak values are about 20 % off. This is probably caused by neglected velocity and temperature profiles in the analytical model. The peak in the mass flow rate of the simulation is again caused by the hybrid initialization distributing gas in the nozzle at the onset of the simulation. Although the valve is almost closed at 7 ms, the mass flow remains uninfluenced because it is already low due to the low reservoir pressure that drives it. Hence, the narrow flow cross-section cannot further reduce the mass flow rate. It has to be noted here that the peak mass flow rate of the piezo-driven valve is about 70 % smaller than the

mass flow rate of the spring-driven valve for the same reservoir pressure. This is due to the fact, that the reservoir volume of the piezo-driven valve is 67 % smaller than the reservoir of the spring-driven valve, as Eq. 6.3 and Eq. 6.4 show. Simulations with 15 MPa in the reservoir of the piezo-driven valve show similar mass flow rates as for the spring-driven valve at 5 MPa.

The time evolution of the gas velocity along the central axis of the valves was also investigated using the CFD simulations. The results are shown in Fig. 8.11. For the spring-driven valve (Fig. 8.11a), the gas velocity is highest directly after the valve begins to open and the location of the highest velocity is about 0.16 m after the nozzle exit into the vacuum space. The peak value is 570 $\frac{\mathrm{m}}{\mathrm{s}}$ which corresponds to a Mach number of 2. The decrease of velocity is explained by the drop of temperature as the gas in the reservoir expands. A Mach number of 1.3 is reached directly at the nozzle exit so the gas accelerates as it expands into the vacuum, because the sudden change of flow cross-section after the nozzle acts as divergent part of the nozzle.

The piezo-driven valve (Fig. 8.11b) shows a very similar behavior, having the highest flow velocity directly after opening with a value of 550 $\frac{\mathrm{m}}{\mathrm{s}}$ located 0.14 m from the nozzle exit into the vacuum space. This corresponds to a Mach number of 2. The velocity then drops over time due to the temperature drop that was already observed in the spring-driven valve.

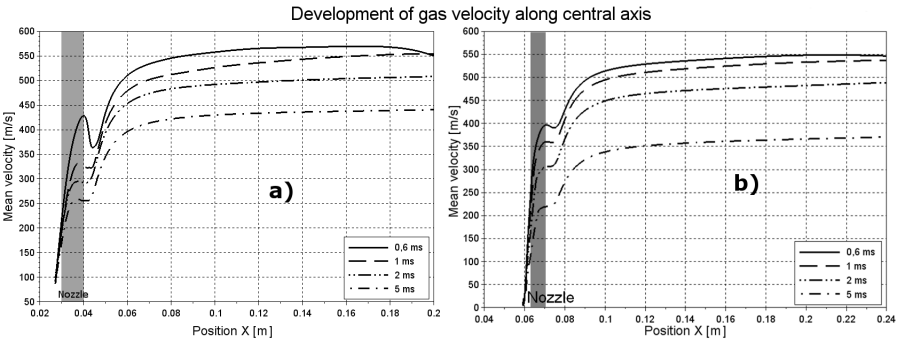

Figure 8.11: Time evolution of the velocity profile along the axis of symmetry for the spring-driven valve (a) and the piezo-driven valve (b)

In addition to the CFD simulation the expansion of the gas cloud was investigated experimentally. This information is useful for the application of MGI since the gas distribution in the vacuum determines the region where strongest cooling takes place during the first milliseconds of interaction between neutral gas and plasma. For the experiment, each valve was suspended in a vacuum tank with a pumped volume of $0.5\,\mathrm{m}^3$ with the valve nozzle oriented towards the bottom of the tank. A fast camera [98] was placed in front of a viewing window allowing a line of sight on the nozzle flange perpendicular to the expected flow axis. The tank was filled with helium to pressures between 1.3 Pa and 1.5 Pa. Voltages between 240 V and 314 V were applied to two in-vessel electrodes creating a glow discharge with plasma currents between 1 A and 2 A. The gas reservoir of the spring-driven valve was filled with argon at a pressure of 5000 Pa while the pressure in the piezo-driven valve was 15000 Pa. The trigger signals for the valves were forwarded to the camera. Hence, when the valve was triggered the camera started recording with a frame rate of 33000 frames per second. The images were then colored according to the light intensity (Fig. 8.12a and Fig. 8.12c).

The argon gas gets excited by the electrons of the helium glow plasma and emits light brighter than the surrounding plasma. The pear shape of the clouds is clearly visible in Fig. 8.12a and Fig. 8.12c, which is in good agreement with the findings of the CFD simulations. For a deeper analysis, the RGB color information of every pixel was added up according to the Euclidian norm to receive the intensity information again. This allowed the evaluation of the intensity distributions along horizontal lines through the image at different distances from the nozzle exit (Fig. 8.12b and Fig. 8.12d). The distribution is symmetrical. Hence a Gaussian curve was fitted into the distribution to even out small oscillations and to compensate the saturation of the camera at distances close to the nozzle. The outline of the cloud was defined where the Gaussian curves reach half of their maximum values. These points were then used to fit tangents onto the outline and the angle δ was measured between the central axis and the tangent.

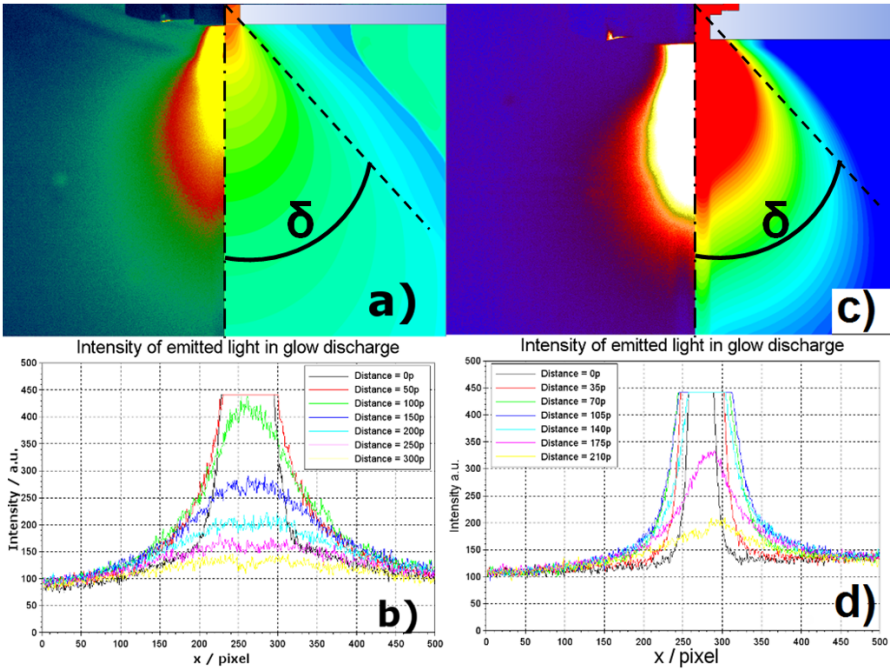

Figure 8.12: Colored image of the expansion cloud (spring-driven valve) 0.28 ms after the valve was triggered (a) and the intensity distribution at various distances from the nozzle exit (b) and colored image of the expansion cloud (piezo-driven valve) 1.1 ms after the valve was triggered (c) and the intensity distribution at various distances from the nozzle exit (d)

For the spring-driven valve, the angle decreases with the distance from the nozzle exit, starting from 49° directly at the nozzle exit to 22° at the bottom of the image, corresponding to a distance of 90 mm. The effective width of the cloud at this distance was measured to be about 120 mm. In the CFD simulation, the angle was measured between the central axis and tangents where the pressure is half the maximal value. The values for the angles are close to the experimental findings with $\delta = 50°$ at the nozzle exit and $\delta = 20°$ at 90 mm distance.

In the case of the piezo-driven valve, the cloud shows a short necking directly at the nozzle exit with an opening angle of 10°. In a distance of 10 mm the cloud forms the barrel shape with an angle of 54°. At the bottom of the

image, in a distance of 90 mm, the opening angle of the cloud is about 24°. The necking could not be observed in the CFD simulation. However, the opening angles fit well with $\delta = 52°$ at the nozzle exit and $\delta = 26°$ at 90 mm distance.

The images also revealed, that the intensity distribution deviates from its symmetrical shape 1 ms after the injection due to discharges between the valve and the anode, which is located to the right of the valve. The argon density in the plasma after 1 ms is high enough to reduce the electric resistivity of the glow plasma, leading to these bright flashes.

Chapter 9

Installation in ASDEX Upgrade

In this chapter, the installation of the new valves into the vacuum vessel of ASDEX Upgrade is explained. This includes the installation locations, additional in-vessel components (shields and suspensions), the gas supply system and the control system.

9.1 In-vessel setup

Three new valves were installed in ASDEX Upgrade in 2016: two spring-driven valves and one piezo-driven valve. These complete the ASDEX Upgrade MGI system consisting of the three new valves, an older spring-driven valve and two electromagnetic safety valves outside the vacuum vessel. The in-vessel valves are set up in pairs with each pair being located 180° in toroidal direction from each other (Fig. 9.1) to compare the effects of outboard and inboard injection.The first pair consists of the two new spring-driven valves, one on the magnetic low field side (LFS) and one on the magnetic high field side (HFS). The second pair on the opposite toroidal position is comprised of the older spring-driven valve on the LFS and the new piezo-driven valve on the HFS. All valves are located roughly on midplane level of the torus.

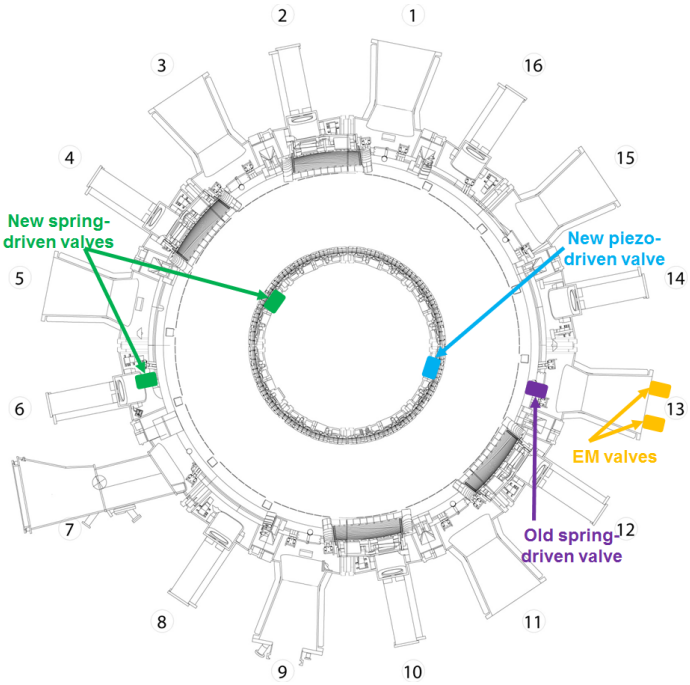

Figure 9.1: Toroidal locations of the MGI valves in ASDEX Upgrade

When planning the installation of the valves in the vacuum vessel, it has to be considered, that the valves will operate in close proximity to the plasma. Hence, they have to be shielded by plasma facing components since stainless steel would heat up rapidly and possibly melt, damaging the valve and degrading the in-vessel conditions. Furthermore, forces during disruptions pose a significant threat. The valves are designed to withstand forces due to induced eddy currents, but the suspensions that fix the valves to the vessel have to handle these forces as well and have to be designed accordingly. The gas supply and control systems are also crucial parts of the new MGI system. In addition to the gas handling system for the old spring-driven valve, a completely new system was developed to support the three new valves simultaneously. The control system was restructured to allow management of all four in-vessel valves in parallel from one screen. A detailed description of the newly developed components is given in the following.

9.2 Shielding

Plasma temperatures in ASDEX Upgrade can reach several thousand Kelvin at the edge [99]. Highly energetic particles and electromagnetic radiation transport energy to the plasma facing components. This results in temperatures of several hundred Kelvin at the surface of these parts. The valves are designed to withstand the baking temperature of 150 °C, hence these elevated temperatures could cause serious damage especially to sensitive parts like the viton seal. Additionally, highly energetic particles erode stainless steel and thereby release heavy elements like Fe, Cr, Ni, Mn and Si from the alloy into the plasma. These impurities radiate power from the plasma very rapidly and lead to disruptions. Thus the valves have to be shielded from the plasma by materials with high melting temperature and a low sputtering yield with respect to the energies of the particles coming from the plasma (1-40 eV in AUG [100]).

For the spring-driven valves in segment 6 (Se6) (Fig. 9.2a) and segment 13 (Se13) on the LFS, shielding is achieved by mounting tungsten-coated carbon tiles in front of the valves. The sputtering yield of tungsten, which is used in the AUG divertor, is acceptable (10^{-4} atoms/ion [100]) and the flux of tungsten particles from the shielding tiles is assumed to be acceptable as the ion flux at the installation locations is lower than at the divertor. The tiles have a circular drilling in their center with the same diameter as the valve nozzle. The tiles are installed in such a way that the drilling and the nozzle align. Since carbon is brittle, the tiles are installed loosely at the nozzle flanges. In the case of the new spring-driven valve in Se6, the wave guides for the position detector have to be shielded separately as they are not covered by the tile. This is done by enclosing them in a flexible stainless steel bellow with an inner diameter of 4 mm. Since the wave guides are several centimeter further away from the plasma than the tile, they experience a lower flux of energetic particles, thus stainless steel can be used.

The magnetic high field side in ASDEX Upgrade is equipped with a heat shield that protects the inner wall. This inner heat shield is made up of 15 rows of tiles which go around the inner side of the torus. The tiles are made of

tungsten-coated carbon but the 5th row from the top and the bottom were replaced by metallic tiles made of P92 [101]. The valves on the HFS (Fig. 9.2b, 9.2c) have to be installed behind this heat shield which poses strict space restrictions. The valves were designed to fit in this narrow space between vessel wall and heat shield. However, no additional shielding has to be provided.

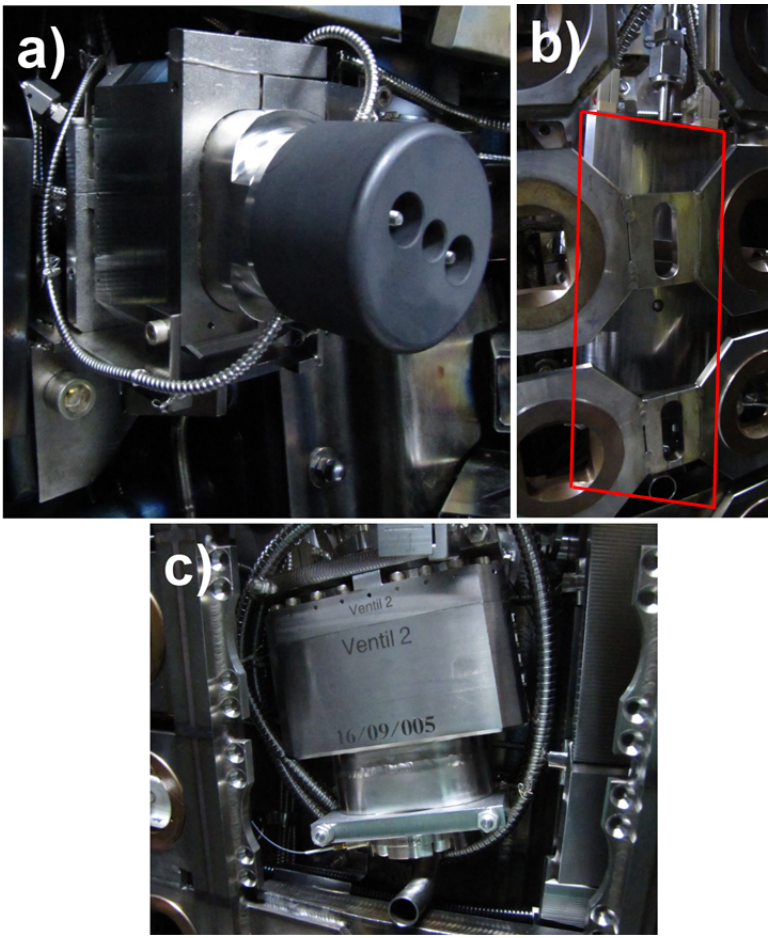

Figure 9.2: Installed valves in the vacuum vessel a) spring-driven valve Se6 LFS with carbon tile, b) piezo-driven valve Se13 HFS behind the heat shield suspension, c) spring-driven valve Se4 HFS in an opening of the heat shield suspension

9.3 Suspensions

A solid suspension is necessary for the valves because the in-vessel components are very closely together and movement of the valve could damage surrounding components or the valve itself. The main drivers for displacements are disruptions. The decaying plasma current leads to rapidly changing magnetic field which gives rise to eddy currents in the valves. These eddy currents cross the stationary toroidal magnetic field and cause Lorenz forces on the valve. The suspension must take up these forces while deformation must remain minimal. The dimensions and the orientation of the valve in respect to the magnetic field components play an important role. To simplify the problem, the valve will be assumed to be a solid stainless steel block (Fig. 9.3) and the skin time of the magnetic field will be neglected which results in the largest possible force. The calculation of the forces was performed according to the standard procedure for jxB forces at ASDEX Upgrade presented in Appendix E.

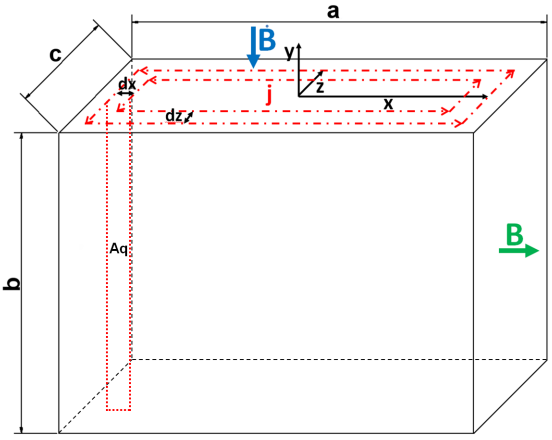

Figure 9.3: Simplified model of the valve for Lorenz force calculation

The induced eddy current density j is perpendicular to the changing magnetic field $\dot{B}$ and flows in the xz-plane with the corresponding valve dimensions a and c. The constant magnetic field B is perpendicular to the z-component of

the eddy current. Hence, only this component contributes to the Lorenz force. From the geometry one can derive a simple relation between the thickness of the current frame and the dimensions of the valve.

$$\frac{dz}{dx} = \frac{z}{x} = \frac{c}{a} \tag{9.1}$$

The area A_r in which the current is flowing and the length of the current loop l are defined by the lengths of x and z.

$$A_r = 4 * x * z = 4 * \frac{c}{a} * x^2 \tag{9.2}$$

$$l = 2 * (2z + 2x) = 4 * \frac{c}{a} \left(1 + \frac{a}{c}\right) * x \tag{9.3}$$

The electrical resistivity of the loop R_r depends on the specific electrical resistivity of the material η and the cross sectional area $A_q = b * dx$.

$$R_r = \frac{\eta * l}{A_q} = \frac{4 * \eta * c * x}{b * dx * a} * \left(1 + \frac{a}{c}\right) \tag{9.4}$$

The induced current dI_s is driven by the changing magnetic field.

$$dI_s = \frac{\dot{B} * A_r}{R_r} = \dot{B} * \frac{b * x * dx}{\eta * (1 + \frac{a}{c})} \tag{9.5}$$

The changing magnetic field is calculated from the plasma current I_p which decays within the CQ time Δt_{CQ} and the mean plasma radius $\sqrt{a_p * b_p}$.

$$\dot{B} = \frac{I_p * \mu_0}{\Delta t_{CQ} * 2 * \pi * \sqrt{a_p * b_p}} \tag{9.6}$$

Using the highest possible values for AUG (I_p = 1.6 MA, Δt_{CQ} = 0.005 s, a_p = 0.5 m, b_p = 0.8 m), the highest possible rate on which the magnetic field decays is 100 $\frac{\mathrm{T}}{\mathrm{s}}$. The resulting force on the differential element depends on the static magnetic field B_{stat} and the length of the perpendicular current

segment.

$$df = dI_s * B_{stat} * 2z = 2 * B_{stat} * \dot{B} * \frac{b}{\eta} * \frac{\frac{c}{a}}{1 + \frac{a}{c}} * x^2 dx \tag{9.7}$$

For the total force on the current segment, the force on the differential element is integrated.

$$F_{tot} = \int_0^{a/2} df dx = B_{stat} * \dot{B} * \frac{b}{\eta} * \frac{\frac{c}{a}}{1 + \frac{a}{c}} * \frac{a^3}{12} \tag{9.8}$$

Because the current is flowing in opposite directions on both sides of the valve, the force is also acting in opposite directions on the respective sides. This creates a torque which can be derived from Eq. 9.7.

$$M_{tot} = 2 * \int_0^{a/2} (x * df) dx = B_{stat} * \dot{B} * \frac{b}{\eta} * \frac{\frac{c}{a}}{1 + \frac{a}{c}} * \frac{a^4}{16} \tag{9.9}$$

The valves have different orientations with respect to the magnetic field components and different size depending on the location in the torus and the type of the valve.

	a [mm]	b [mm]	c [mm]	F_{tot} [N]	M_{tot} [Nm]
Spring valve Se6 LFS	66	135	170	2877	142
Spring valve Se4 HFS	135	170	66	2683	272
Piezo valve Se13 HFS	88	170	62	1348	89

Table 9.1: Dimensions of the valves with their orientation fitted to the model and the resulting forces and torques due to eddy currents

Table 9.1 shows how the valve dimensions are fitted into the dimensions of the model and which forces and torques are generated. For the calculation, a static magnetic field of 3.5 T, a decay rate of the poloidal magnetic field of 100 $\frac{\mathrm{T}}{\mathrm{s}}$ and a specific electrical resistivity of $0.73 \times 10^{-6}\,\Omega\,\mathrm{m}$ were assumed. The results were used to perform FEM simulations with the valves and their suspensions to evaluate the stress on the suspensions and the maximal displacements. Results are shown in figure 9.4. The spring-driven valve in Se6 LFS (Fig.

9.4a) is mounted on a plate with clamping plates around the gas reservoir and the rear dome to keep it in place. The bottom plate is fixed to the vessel wall using a M16 screw. The FEM simulation shows a Von-Mises stress of about 300 MPa at the head of the screw and the suspension plate. This stress poses no danger for the suspension. The maximal displacement is low with a value of 0.3 mm. The piezo-driven valve in Se13 HFS (Fig. 9.4b) is held by two clamps, one above the nozzle flange and one around the main body. Both clamps are screwed to the vessel wall using M6 bolts and nuts. The FEM simulation shows little stress near the base of the bolts (250 MPa), but the values are far below the acceptable safety limit. As for the displacement, a value of 0.9 mm poses no problem in the installation position. The spring-driven valve in Se4 HFS (Fig. 9.4c) is fixed by a lower clamp which is located right above the nozzle flange and an upper clamp which goes around the rear dome. Both clamps are screwed to the vessel wall using M6 bolts and nuts. From the FEM simulation it can be seen that stress occurs in the bolts, but it is below the acceptable safety limit. The maximal displacement is about 1.1 mm which is sufficiently low for the installation position.

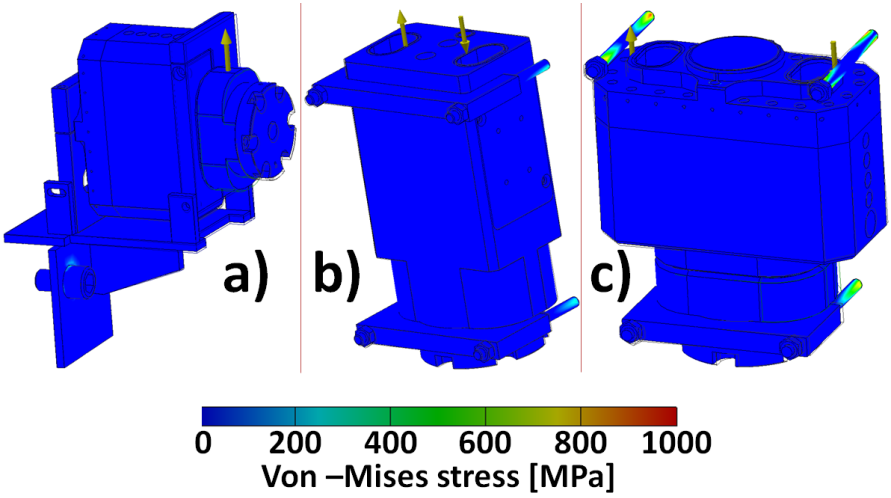

Figure 9.4: FEM stress analysis with the calculated force during disruptions a) spring-driven valve Se6 LFS, b) piezo-driven valve Se13 HFS, c) spring-driven valve Se4 HFS

9.4 Gas supply

The new gas supply is designed to support three in-vessel valves. Together with the supply for the old spring-driven valve it completes the gas handling system for the in-vessel valves (Fig. 9.5), although both supplies operate independently. The gas supply provides pressurized air and mitigation gas to four valves, even though the piezo-driven valve does not require pressurized air. The additional air line is foreseen as backup for a possible fourth spring-driven valve.

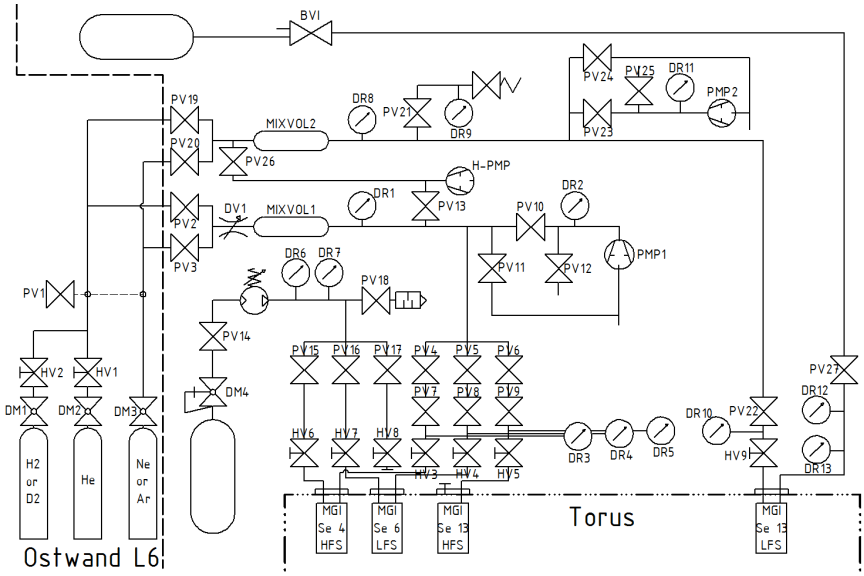

Figure 9.5: Scheme of the gas handling system for all in-vessel MGI valves in ASDEX Upgrade

The mitigation gas (H_2, D_2, He, Ar, Ne) is taken from three 10 l gas bottles outside of torus hall. Each bottle is equipped with its own pressure reducer (DM1, DM2, DM3). The gas lines run into the hall and through a valve that closes or opens both lines simultaneously (PV1). For the gas supply of the three new valves, the gas then flows through two pneumatic safety valves (PV2, PV3) and a pressure reduction valve (DV1) into a gas reservoir

(MIXVOL1), where the gases from both lines can be mixed. From this reservoir the gas line is probed by a pressure gauge (DR1) and afterwards split into three separate lines, each equipped with two pneumatic safety valves (PV4 - PV9), of which the second one is controlled by the ASDEX Upgrade shutter control, and a manual safety valve (HV3 - HV5). The gas lines then go through three CF63 flanges into the vacuum vessel and end at the MGI valves. Venting the gas from the reservoir is done by a bypass valve (PV11) which directs the gas into the exhaust line. A sliding vane rotary vacuum pump (PMP1) is used to evacuate the residual gas in the reservoir and a secondary valve (PV12) in the pumping line allows flooding of the system. For the use of flammable gases, a second hydrogen pump (H-PMP) must be used for evacuation. It can be accessed by opening valve PV13.

The pressurized for the new spring-driven valves air is taken from the 0.6 MPa air supply of the torus hall and routed into a pressure reducer. From there the air line runs into the pressure booster with a pneumatic valve (PV14) in between to cut off the air. The booster amplifies the pressure by a factor of 4, so the pressure reducer is used to tune the system pressure. Behind the booster, the air line is split into three separate lines, each holding a pneumatic (PV15 - PV17) and a manual safety valve (HV6 - HV8), before going through the CF63 flanges into the vacuum vessel, ending at the new spring-driven MGI valves. A separate pneumatic valve (PV18) after the pressure booster allows the venting of the air lines.

For the old spring driven valve, the mitigation gas runs through two pneumatic safety valves (PV19, PV20) into the mixing volume (MIXVOL2). Behind this reservoir, the gas is routed through a pneumatic valve (PV22), which is controlled by the ASDEX Upgrade shutter control, and a manual safety valve (HV9) into the torus and the old spring-driven MGI valve. The gas line can be vented by opening the bypass (PV24) and it can be evacuated using the membrane pump (PMP2). The pumping system can be flooded by opening a pneumatic valve (PV25). If flammable gases are used, the gas line has to be evacuated using the hydrogen pump must be used which can be accessed by opening a pneumatic valve (PV26).

The old spring-driven valve requires 0.6 MPa for closing the valve. Hence,

the pressurized air is taken from the supply of the torus hall and connected to a switching valve (BVI). This valve either routes the air to the MGI valve (through PV27) or allows the venting of the air from the MGI valve.
Gas lines and air lines are completely separated from one another. This is required to prevent explosive mixtures since flammable gases are used. Additionally, the entire system is built from full-metal components, the gas bottles are stored outside the torus hall and a separate pumping system (H-PMP) is attached. The document explaining the measures for preventing explosive mixtures is given in Appendix F.

9.5 Control system

The MGI valves can either be operated autonomously by the ASDEX Upgrade plasma control system or manually. For automated operation, the Interlock (plant safety), the TS06 (discharge onset) and the Locked mode (stationary neoclassical tearing mode) signals are received by waveguides and converted into digital signals. The TS06 signal is then forwarded into a delay module which postpones the transfer of the signal so the valve triggers after a defined time into the discharge. The delayed signal is then sent to an OR module together with the Interlock and Locked mode signals. There it is decided which signal shall be used to send out the trigger signal which is then sent to the trigger circuits (Appendix C.2 and C.4). For manual operation, the valves can either be triggered directly from the trigger circuits or by using the MGI S7 control system with the WinCC interface. The MGI valves are managed by a S7 CPU which is connected to the OR modules for the spring-driven valves by digital signal converters. An external ET200M exchanges signals with the OR module for the piezo-driven valve and receives the signals of the spring-driven valves position detectors. Finally, two ET200S with valve systems operate the two gas handling systems. CPU, ET200M and the ET200S communicate via waveguides between one another and with the terminal computer that runs the WinCC interface (Fig. 9.6). A complete signal plan of the control system for the new MGI valves is shown in Appendix G. The WinCC interface allows remote control of the MGI valves and the gas supply systems. From the screen

in Fig 9.6 the air and gas lines can be monitored and routed by opening the pneumatic valves. The MGI valves themselves can be triggered manually and the feedback signals are visualized.

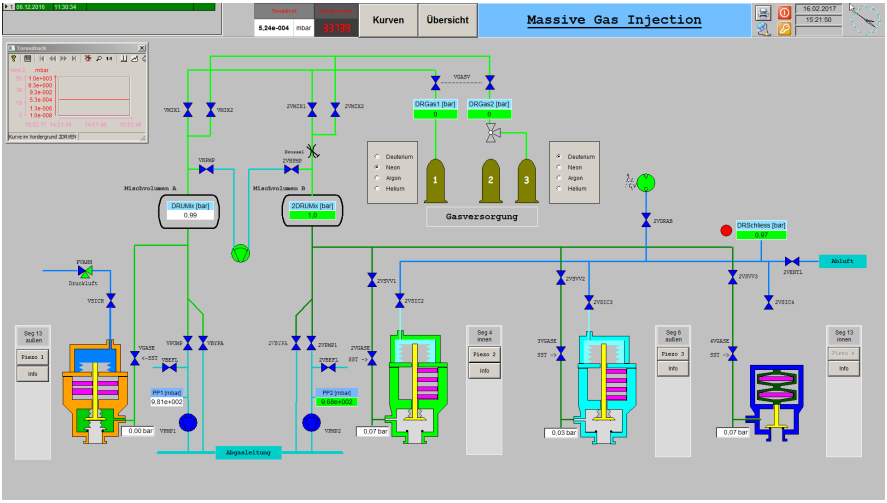

Figure 9.6: WinCC interface of the MGI control system

Chapter 10

Test results in ASDEX Upgrade

After the maintenance phase, in which the three new MGI valves were installed, was finished, the vacuum vessel was closed in February 2017. The baking of the vacuum vessel was started shortly after pumping had started. In March 2017, after 10 days of baking at 150 °C, ASDEX Upgrade was restarted. The new in-vessel MGI system was among the first systems to be tested. This chapter summarizes the results of the technical tests, the calibration tests for the delay times of the valves and the experiment on radiation asymmetry.

10.1 Technical tests

These tests were performed to check whether the valves were operational after baking. The measurements were done without plasma using only the manometers which has the advantage of not interrupting discharges. As the tests were carried out during the start-up phase of ASDEX Upgrade, only helium was allowed to be injected into the vessel to prevent contamination of the vessel walls with medium-Z impurities. The valves were triggered by the TS06 signal. This signal was routed through the delay modules so the valves would release the gas after the plasma discharge had finished and the

vessel was empty. The ensuing gas pulse was measured using seven in-vessel ionization manometers [102] which have a time resolution of 1 ms. These manometers ionize the gas at a heated filaments and apply an electric field. The ions and electrons are accelerated towards the anode or the cathode and thereby create ion and electron currents. These currents are measured and proportional to the gas pressure. The particle flux density Γ can be calculated from the currents (I^+, I^e) using the calibration factors for each gauge. The calibration factors are used to calculate a conversion factor S.

$$\Gamma = \frac{I^+}{I^e - I^+} * \frac{4 * 10^{29} * (I^e + 1)}{S} \tag{10.1}$$

$$S = aa - \begin{cases} ab - I^+ & ab > I^+ \\ 0 & ab \leq I^+ \end{cases} * ac + I^+ * bb - cc * \begin{cases} ee & ee > 0^+ \\ 0 & ee \leq 0 \end{cases} \tag{10.2}$$

The calibration factor ee is derived from the ion current and further factors.

$$ee = 1 - exp\left(\frac{-(I^+ * 10^7 - dd)}{ff}\right) \tag{10.3}$$

The calibration factors were determined in the gauge test bed before their installation in the vessel [102]. Table 10.1 summarizes all used calibration factors for each gauge. According to the kinetic gas theory, the gas pressure is calculated from the particle flux using a correction factor k^g for the gas species.

$$p = \Gamma * k^g * \sqrt{2 * \pi * k_B * T} \tag{10.4}$$

The ionization manometers are located at different toroidal (Fig. 10.1) and poloidal locations. Hence, each gauge has a different distance to the valves. This allows the observation of the gas expansion in the vessel.

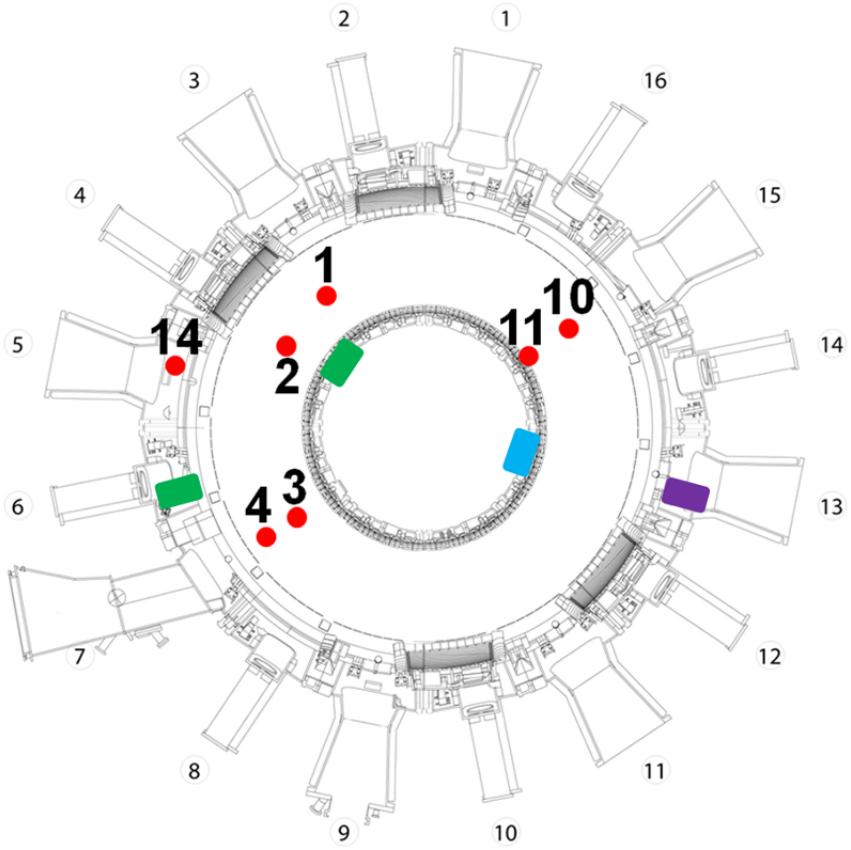

Figure 10.1: Toroidal locations of the manometers, new spring-driven valves (green), piezo-driven valve (blue) and old spring-driven valves (violet)

The measurement heads of the gauges have different orientations with respect to the plasma and are mounted behind divertor tiles and heat shields. This delays the time at which the gauges register the first gas particles. The locations are given in Table 10.1. However, the gauges allow a good detection of the gas cloud expansion in the torus and can be used for the technical tests of the valves.

	Se	aa	ab	ac	bb	cc	dd	ff
1	3	126.5	4×10^{-7}	6×10^{7}	4×10^{5}	54.4	15	26
2	4	150	4×10^{-7}	6.5×10^{7}	-5×10^{-5}	0	11	5
3	7	115	2×10^{-7}	2×10^{8}	1.5×10^{5}	48	10	15
4	7	92	4×10^{-7}	6.8×10^{7}	2.8×10^{5}	28.8	9.6	26
10	15	105.3	5.27×10^{-7}	11.2×10^{7}	-3×10^{5}	17.5	50	30
11	15	123	2×10^{-7}	5×10^{7}	2.2×10^{5}	58	5	5
14	5	140	7×10^{-7}	4×10^{7}	1×10^{6}	45	17	25

Table 10.1: Locations and calibration factors for each ionization manometer

The spring-driven valve in Se4 on the magnetic high field side was tested in shot 33752. The valve was prepared with 0.206 MPa of helium which corresponds to 26.4 Pa m^3 or 6.37×10^{21} particles. No leak could be observed. The delay module was set to trigger 6.5 s after the TS06 signal. The measured pressures are shown in fig. 10.2.

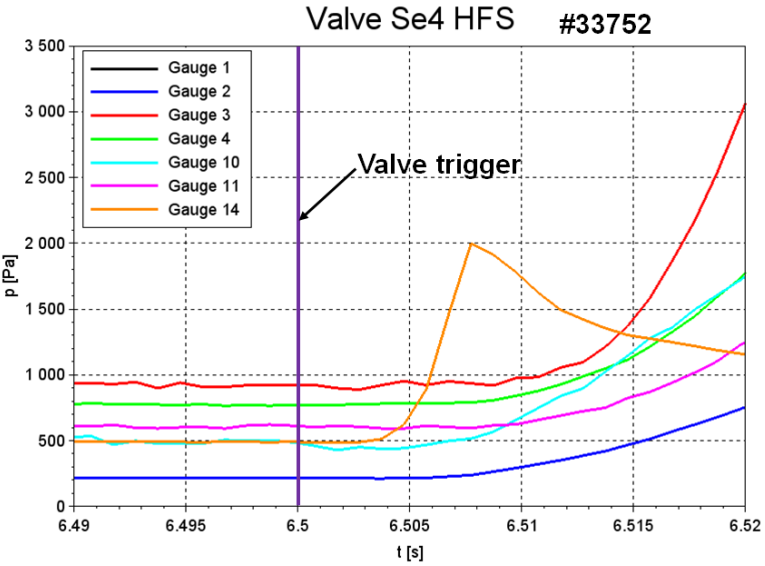

Figure 10.2: Pressure measurements after trigger in shot 33752

Gauge 14 is the first to react after 3 ms as it has the direct line of sight onto the valve. The pressure front has passed the gauge into the A-port 8 ms after the trigger. Gauges 2 and 10 react after 5 ms as they look towards the vessel through the divertor tiles. The manometers looking away from the vessel see the first gas particles about 10 ms after the trigger pulse. This proves, that the valve in Se4 triggers at the desired time and the gas is released from the reservoir.

The piezo-driven valve in Se13 on the magnetic high field side was the next to be investigated. The gas reservoir was filled with 0.213 MPa helium, corresponding to $9\,\mathrm{Pa\,m^3}$ or 2.16×10^{21} particles. The valve was filled 50 min prior to shot 33764 in which the valve was triggered. During this time, no leak could be detected. The delay module was set to trigger the valve 7.5 s after the TS06 signal. The pressure curves are shown in fig. 10.3.

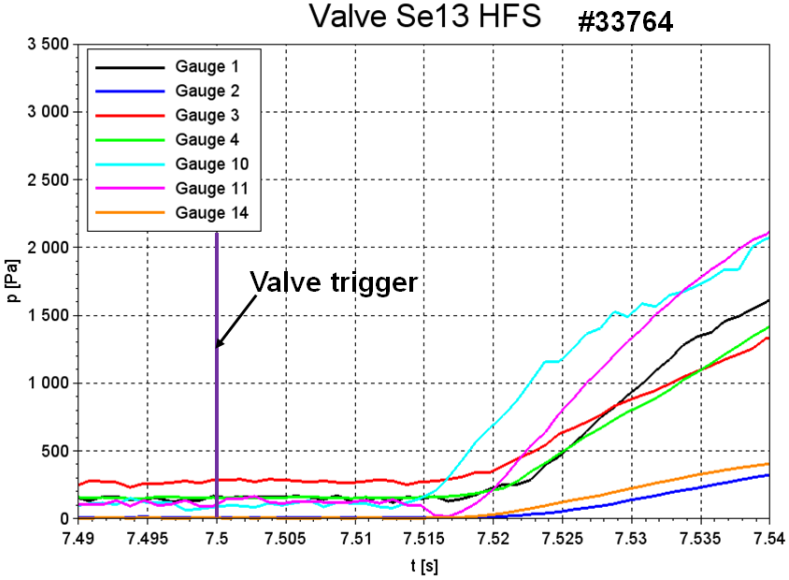

Figure 10.3: Pressure measurements after trigger in shot 33764

The first pressure increase is recorded by gauge 10 after 13 ms and gauge 11 reacts shortly after. These are the gauges which are installed in close proximity of the valve. The other gauges see the gas several milliseconds

later. Compared to the spring-driven valve, the time between trigger and first gas arrival is significantly longer. The time of flight of the gas between valve and first gauge is about 5 ms. This indicates that the piezo-driven valve has a longer delay time. However, the valve triggers and the gas is vented from the reservoir.

The spring-driven valve in Se6 on the magnetic low field side was tested in the following shot 33765. The reservoir was filled with 0.181 MPa of helium which corresponds to $23.2\,\mathrm{Pa\,m^3}$ or 5.6×10^{21} particles. No leakage was observed. The delay module was set to trigger 8.5 s after the TS06 signal. The time traces of the pressures are shown in fig. 10.4.

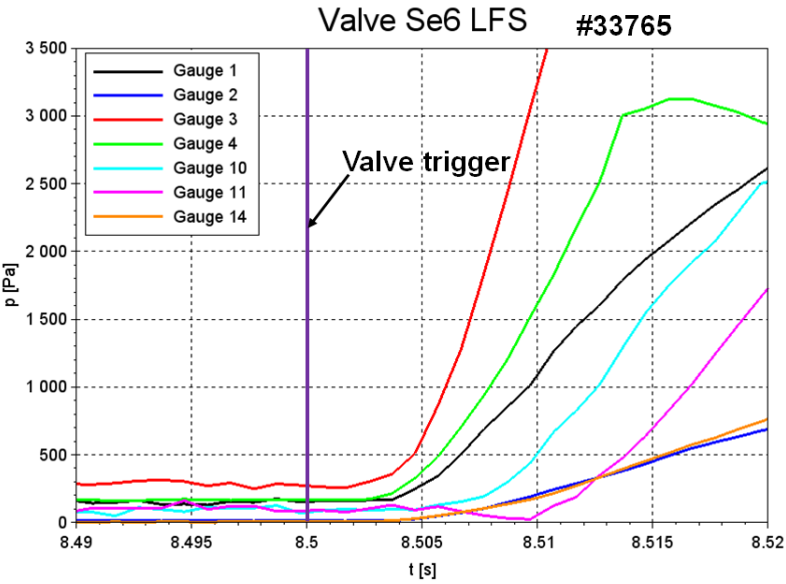

Figure 10.4: Pressure measurements after trigger in shot 33765

Gauge 3 and 4 are the first to record the gas pulse 2 ms after the trigger as they are closest to the valve. Gauge 1, 2 and 14 see the pressure increase 1 ms later because their distance to the valve is slightly larger. This shows that the delay times of the spring-driven valves are of the same order. The spring-driven valve in Se6 triggers reliably to the set time and releases its gas.

10.2 Delay time measurement

The delay time is defined here as the time between the trigger signal to the valve and the arrival of the gas at the plasma edge. It includes the response time of the valve and the time of flight of the gas from the nozzle exit to the plasma edge. This delay time is an important characteristic of each valve as it determines when the valve has to be triggered to inject into certain phases of disruptive plasmas. Additionally, the delay times have to be considered when synchronizing the the valves for simultaneous operation.

The experiments aimed to measure the delay time were performed using the diode bolometers in ASDEX Upgrade [103] which measure the radiated power along their lines of sight. During MGI, the electrons of the impurity atoms are excited when they undergo collisions with the plasma electrons. When the electrons return to their ground state, they emit photons with a certain energy. These photons produce electron-hole pairs in the semiconductors of the bolometer diodes, resulting in a photo-current. The photo-current is calibrated to be proportional to the radiated power over a wide range of photon energies. The high time resolution of 5 µs makes this diagnostic ideal for the delay time measurement. The diode bolometers cover a total of 256 lines located in the poloidal planes of Se5 and Se13. The lines closest to the nozzles of the MGI valves, which are shown in figure 10.5, were used for this measurement.

Conditioning plasmas were used for the measurements of the delay times. These plasmas are created to test the heating and diagnostic systems and hence have, among others, different properties concerning thermal energy, magnetic field strength and plasma density. Only the plasma current of 0.8 MA was the same for each plasma. However, the delays and opening times of the valves, as well as the expansion of the neutral gas from the valves are not influenced by the plasma parameters and therefore these plasmas are suited for the delay time measurement. For the evaluation of the delay time, the 5000 samples from the bolometer signals before the valve trigger were averaged. Gas arrival was assumed when the signals rose 10 % above their respective average value.

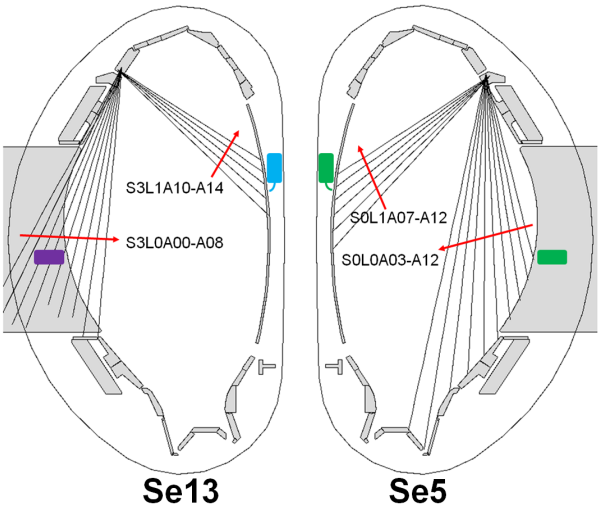

Figure 10.5: Used lines of sight of the bolometers, new spring-driven valves (green), piezo-driven valve (blue) and old spring-driven valves (violet)

The first test was performed with the spring-driven valve in Se6 on the magnetic low-field side in shot 33806. The reservoir of the valve was filled with 0.224 MPa of neon (28.7 Pa m^3 or 6.9×10^{21} particles) and was set to trigger 7.2 seconds into the discharge. The bolometer signals are shown in figure 10.6.

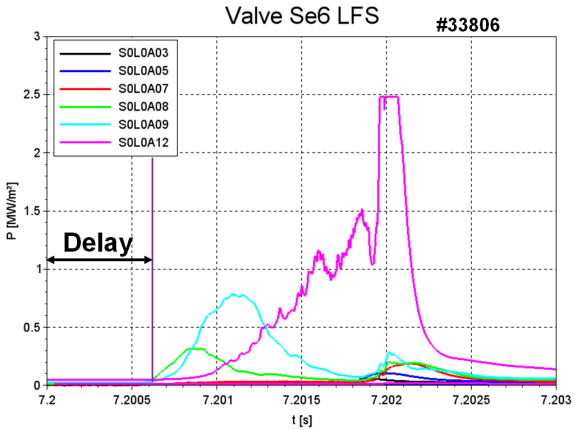

Figure 10.6: Calibrated bolometer signals Se5 LFS 7.2 s after trigger in shot 33806

The signal S0L0A08 is the first to show a significant increase in radiation 0.63 ms after the trigger. Although line S0L0A07 is closer to the valve, it is located outside the plasma and hence line A08 is the first to respond. This first response is taken as delay time of the valve in Se6. In this case the propagation of the gas into the plasma can be observed nicely as the neighboring lines of sight show increase of radiation one after another with a time difference of about 1 ms. The further the line of sight is located in the plasma, the higher is the peak radiated power. This is because the plasma density and temperature increase towards the plasma core and hence more neon atoms are ionized as they penetrate into the plasma. A second peak can be seen on all observed channels at 7.2019 s. The timing of this peak is coherent with the thermal quench of the plasma. Radiation levels are increasing the deeper the line of sight is located in the plasma during this phase and the two inner most lines go into saturation. This shows that strongest radiation during the thermal quench takes place in the plasma core. The cooling time in this case is 1.3 ms during which three small peaks can be seen on the signal S0L0A12. The values of these peaks are growing towards the thermal quench which could be due to growing MHD modes or filaments.

The next test was done with the valve located in Se4 on the magnetic high field side in shot 33807. The valve was prepared with 0.229 MPa of neon ($29.3\,\mathrm{Pa\,m^3}$ or 7×10^{21} particles) and was set to trigger 6.5 s into the discharge. The signals of the bolometers for this discharge are shown in figure 10.7.

The line S0L1A11 is the first to see increased radiation 0.82 ms after the trigger pulse. This is the line closest to the nozzle exit. The neighboring lines A10 and A12 show an increase 0.01 ms later. This is due to the fact that these lines of sight have a large angle with respect to the plasma edge and hence the gas atoms reach these lines almost at the same time. The propagation of the gas atoms into the plasma which could be seen in figure 10.6 is not visible also due to this configuration. The signals of the lines close to the nozzle go into saturation and the lines further away show a first peak 1 ms after the trigger. The radiation then drops again before rising into saturation on all lines. This rise and the current quench occur simultaneously, so for this

discharge, the cooling time is 1 ms. However, no growing radiation peaks can be seen. The signals remain saturated even after the thermal quench because of the sensitivity of these bolometer channels.

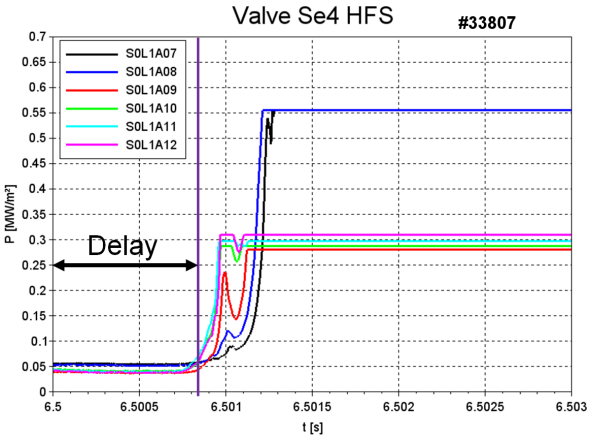

Figure 10.7: Calibrated bolometer signals Se5 HFS 6.5 s after trigger in shot 33807

The piezo-driven valve in Se13 on the magnetic high field side was investigated in shot 33818. The reservoir was filled with neon at a pressure of 0.44 MPa (18.5 Pa m^3 or 4.4×10^{21} particles) and the trigger was set to open the valve 7 s into the discharge. The resulting signals of the respective bolometer channels are shown in figure 10.8.

The first line of sight which sees increased radiation is S3L1A12 with a delay time of about 9.2 ms. The neighboring lines A11 and A13 follow about 0.01 ms later. This is the same effect that was observed with the valve in Se4 due to the similar configuration of the lines of sight with respect to the valve. The delay time is significantly larger compared to the spring driven valves which was already indicated during the technical tests. However, the average gradient of the radiated power on the first line of sight that sees the increase (1340 MW m^{-1} s^{-1}) is of the same order as the average gradient for the spring-driven valve ion Se4 (1260 MW m^{-1} s^{-1}). This suggests that the valves open on a similar time scale and the gas clouds expand in a comparable fashion. Hence it is likely that the main contributor to this long delay time is the

response time of the valve. The main reason for this response time is probably the 40 m cable that connects the valve with the power supply as this long response time was not observed during the laboratory tests using a short cable. When the valve is triggered, the PE actuators are charged from the capacitors causing a significant current (up to 70 A). Therefore the inductance of the cable becomes important factors and has to be taken into account. A solution to this problem could be the removal of the inductance that was built into the trigger card to limit the maximal current. A drop in radiation and a second increase can be seen on the channels S3L1A13 and A14 about 0.96 ms after the gas arrives at the plasma edge. This second increase coincides with the onset of the thermal quench. However, during the cooling time, no distinct radiation spikes like in figure 10.6 can be seen.

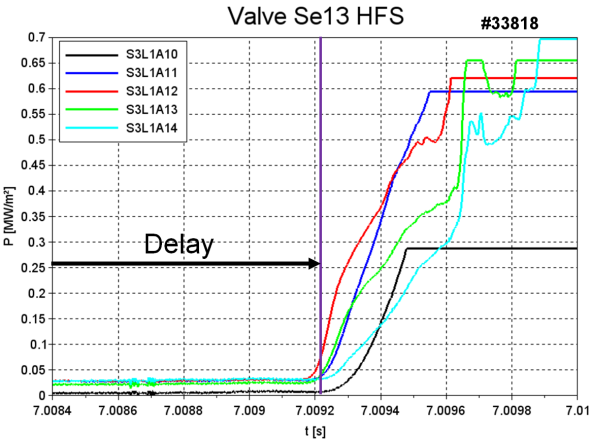

Figure 10.8: Calibrated bolometer signals Se13 HFS 7.0084 s after trigger in shot 33818

The old spring-driven valve in Se13 on the magnetic low field side was tested in shot 33819. Its reservoir was filled with 0.32 MPa of neon (25.6 Pa m^3 or 6.1×10^{21} particles) and was set to trigger 7 s into the discharge. The bolometry signals of the relevant lines of sight are shown in figure 10.9.
The delay time, as seen on line S3L0A04, is 0.4 ms, so of the same order as the delay time of the new spring-driven valves. The lines A03 and A05 which are next the first response line of sight follow about 0.01 s later. The

configuration of valve and lines of sight is similar to the configuration for the valve in Se6. The main difference is that the toroidal distance between the bolometers and the valve is a bit larger in Se6. This explains the slightly shorter delay time of the old spring-driven valve.

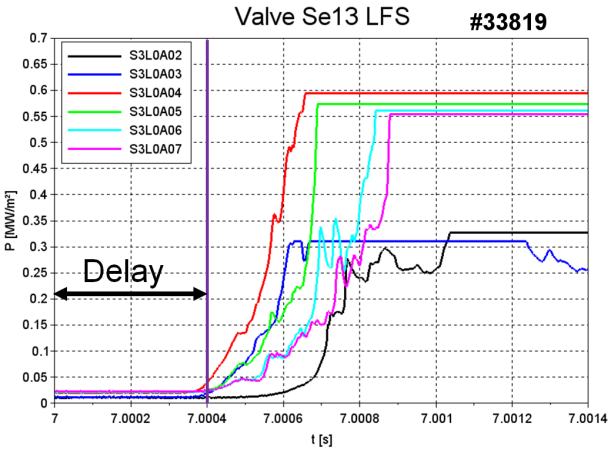

Figure 10.9: Calibrated bolometer signals Se13 LFS 7 s after trigger in shot 33819

10.3 Toroidal radiation asymmetry

During MGI, the radiated power increases first at the location where the gas interacts with the plasma. This leads to a toroidally asymmetric radiation distribution as shown at DIII-D [83] and AUG [84]. For this reason, the new MGI valves were installed at different toroidal locations to investigate whether this radiation asymmetry can be mitigated by injecting with two valves at different locations. For this experiment, the new spring-driven valve in Se6 and the old spring-driven valve in Se13 were used as they have the same poloidal position but are toroidally about 160° apart. The radiation is detected by the bolometer arrays in Se5 and Se13. These arrays are 180° apart from one another. From the radiated energy that these arrays detect, the

asymmetry factor is calculated which characterizes the radiation asymmetry.

$$ASF = \frac{W_{Se5} - W_{Se13}}{W_{Se5} + W_{Se13}} \tag{10.5}$$

Four very similar discharges were performed, three with the LFS valves and one with the valves Se4 HFS and Se6 LFS for comparison. These plasmas are characterized by a plasma current of 0.8 MA, a toroidal field strength of 2.5 T and an edge safety factor of about 5. The configuration was a lower single null H-mode plasma with an elongation of 1.75. As for the heating power, different heating systems were used in the discharges with total heating powers between 9.5 MW and 15 MW. Resulting electron densities are between 6.2×10^{19} and 6.6×10^{19} with temperatures between 2.1 keV and 2.4 keV. The poloidal magnetic energy was 333 kJ while the total thermal energies were between 400 kJ and 520 kJ. The valves were synchronized using the measured delay times described in section 10.2. However, the valves were triggered with varying delay times Δt with respect to one another as the gas requires some time to be carried around the plasma. The neon pressures in the valves were adjusted so both used valves injected roughly the same amount of particles. The parameters of the valves for these experiments are given in table 10.2.

Nr.	t_{trig} [s]	gas	m_{13} [Pam^3]	m_6 [Pam^3]	p_4 [Pam^3]	Δt [ms]
33832	6.5	Ne	24.56	23.68	-	0
33834	5.4	Ne	18.88	19.84	-	0.1
33836	5.7	Ne	14.24	16.26	-	-0.1
33842	6.5	Ne	-	19.33	19.46	0
33806	7.2	Ne	-	31.23	-	∞

Table 10.2: Valve parameters for the radiation asymmetry experiments and the reference shot with valve Se6

The results at DIII-D were obtained with similar plasma parameters and amounts of neon gas. They indicate that the asymmetry is different during the phases of the disruption. For this purpose, the asymmetry factor was calculated individually for each phase, taking the radiation level as indicator

when the pre-thermal quench begins and the plasma current for the onset of the thermal and current quench phases. The end of the current quench was defined at the time when 80 % of the plasma current had decayed. The radiated energies were calculated in each phase by integrating over the phase duration. Resulting asymmetry factors are shown in figure 10.10.

When comparing the asymmetry factors for the experiments done with the valves in Se6 and Se13, it is clearly visible that the asymmetry is small. During all three phases, the asymmetry is below 10 % regardless of the delay time. However, when the valve in Se13 is triggered first (Δt = -0.1 ms), a negative asymmetry occurs during the pre-TQ phase. This indicates that radiation is still higher close to the injection location even for short delay times. The results obtained with the valves in Se6 and Se4 show a significantly higher asymmetry during the pre-TQ phase (38 %) and the reference shot using only the valve in Se6 shows a similar result. In these two scenarios, the impurities were injected roughly at the same toroidal position. This suggests that the asymmetry can be reduced when injecting the gas from two locations which have a large toroidal distance to one another.

A comparison with the results from DIII-D shows a significant reduction of the radiation asymmetry during the pre-TQ phase. This is due to the shorter delay time used for the experiments in ASDEX Upgrade. When injecting from gas with a single valve or from locations close together, the asymmetry during the pre-TQ is of the same order as in DIII-D which used a $\Delta t > 0.5$ ms. This points out that injection from two locations which have a significant distance in toroidal direction can reduce the radiation asymmetry when the valves are triggered simultaneously or with a very short delay ($\Delta t < 0.1$ ms). However, radiation asymmetries are significantly higher when using MGI on plasmas with lower thermal energy as it was shown on AUG. Hence, it can be assumed that the asymmetry factor depends not only on the valve setup, but also on plasma parameters like thermal energy, electron temperature and the presence of MHD modes.

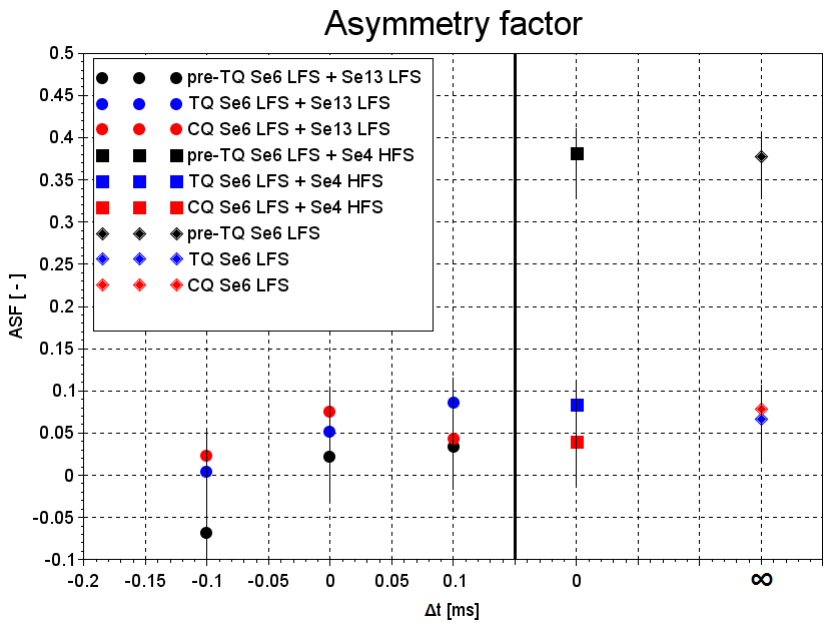

Figure 10.10: Asymmetry factors for different delay times, used valves and disruptive phases

Chapter 11

Summary and outlook

A new in-vessel MGI system for disruption mitigation experiments has been developed and implemented in the Tokamak ASDEX Upgrade. The new system consists of two spring-driven valves and a piezo-driven valve which operate alongside an older spring-driven valve. A new gas handling system has been built to supply the three new valves and the control system has been updated to allow simultaneous operation of all in-vessel valves. The valves were thoroughly tested in a laboratory environment and during plasma operation in the Tokamak.

Prior to the development process, a study of previous MGI experiments and valves from several different Tokamak experiments was performed to compile a list of requirements for the new MGI valves. It was found that gas amounts of $40\,\mathrm{Pa\,m^3}$ (1×10^{22} particles) of argon or neon are sufficient for an effective mitigation of electromagnetic forces, thermal loads and runaway electrons in medium-size Tokamaks. Increasing the amount of injected material had proven to reduce the fueling efficiency while increasing the load on the vacuum system. In-vessel valves had shown the highest fueling efficiencies and allowed the use of pure noble gas without the need of dilution with hydrogen for higher sound speeds. An analysis of the evolution of disruptions and the technology currently in use at other machines it was found that an opening time of the valves of a few milliseconds was required for medium-size

Tokamaks. Finally, an old version of a spring-driven valve was retrieved from ASDEX Upgrade and inspected to identify technical deficiencies that had to be improved for the new valves. Points for improvement were found in the cabling, the position detection, the stiffness of the clamping mechanism and the adjustability in the assembled state.

Based on these findings it was decided to develop two different in-vessel valve types to compare different technologies: an improved spring-driven valve and a new piezo-driven valve.

The spring-driven valve was constructed to incorporate a gas reservoir of $128\,\mathrm{cm}^3$ which can hold a gas pressure of up to 5 MPa, thereby allowing a maximal gas inventory of $640\,\mathrm{Pa\,m}^3$ (1.5×10^{23} particles). The spring-driven valve is normally open. Pressurized air pushes the ceramic valve stem forward, tensing the stack of disc springs and pressing the valve plate into the viton seal. Piezoelectric stack actuators clamp the valve stem and the gas reservoir can be filled. After the pressurized air is vented from the valve, it is ready to be triggered. When the valve is triggered, the piezoelectric stacks are discharged, releasing the stem and the disc springs accelerate the valve plate back to its initial position, opening the reservoir. An optical position detection system observes the movement of the valve plate. A new clamping mechanism was implemented to overcome the issues with stiffness and adjustability and a new type of cables was used for power supply.

The piezo-driven valve was designed to have a gas reservoir of $42\,\mathrm{cm}^3$ and for gas pressures up to 5 MPa. This leads to a maximal gas inventory of $210\,\mathrm{Pa\,m}^3$ (5×10^{22} particles). The valve is normally closed and the gas reservoir can be filled. When the valve is triggered, piezoelectric stack actuators are charged. A titanium frame which holds the stacks is deformed to translate the stroke and force of the stacks and pull back the valve plate, opening the reservoir. The titanium frame was specially designed for this valve using analytical and FEM methods, as well as prototype tests.

Both valve types were thoroughly tested. It was found that the spring-driven valve had an opening time of 1.5 ms with a total stroke of 4.5 mm and the piezo-driven valve an opening time of 3.5 ms with a total stroke of 2.1 mm. Outgassing, leak tightness and reliability were studied in a special test bed.

The results concerning outgassing behavior and leak rate allowed the installation of both valve types into ASDEX Upgrade. Reliability was proven by subjecting both valve types to 2000 operational cycles each including baking which they performed without failure. The flow properties were investigated using CFD simulations and the gas expansion cloud was examined in a helium glow discharge. Simulation and glow discharge experiment showed good agreement concerning the cloud geometry for both valve types.

Two new spring-driven valves were installed in ASDEX Upgrade in Se6 on the magnetic low field side and in Se4 on the magnetic high field side. The piezo-driven valve was placed in Se13 on the magnetic high field side. The gas handling system which supplies the new valves allows mixing of two different gases for mitigation experiments including flammable gases. Additionally, it supplies the pressurized air for the spring-driven valves. The updated control system grants access to the gas handling systems and the in-vessel MGI valves, allowing simultaneous operation of all four valves.

A first technical test in ASDEX Upgrade using the in-vessel manometers showed the leak tightness and operability of all valves. Measurements of the delay time of the valves were performed with plasma and the bolometers. It was shown that the old and new spring-driven valves have a delay shorter than 1 ms. The piezo-driven valve was measured with a delay time of 9.2 ms due to a long response time of the actuators. An experiment on radiation asymmetries during MGI revealed a significant reduction of the asymmetry when injecting gas from two toroidally separated locations and with a difference in the delay time shorter than 0.1 ms to one another.

Beyond the scope of this thesis, the piezo-driven valve will be developed further by optimizing the geometry of the titanium frame and by reducing the response time by adjusting the internal inductance in the trigger circuit. In the near future, the MGI valves will be used for experiments on the mitigation of runaway electrons and will possibly serve as safety valves for ASDEX Upgrade. Furthermore, it is under discussion to implement the valves the new Tokamak JT60-SA for disruption mitigation experiments. Since JT60-SA has a plasma volume about 8 times larger than ASDEX Upgrade, the gas amounts have to be adjusted accordingly. The spring-driven valve in its current design

fits to the requirements of JT60-SA concerning opening time and maximal gas inventory. The piezo-driven valve requires a larger gas reservoir, which is easy to implement. Additionally, it was brought up to install a MGI valve in the stellerator W7-X for the mitigation of runaway electrons which can occur when the superconducting coils quench. Both valve types are suitable for this purpose in their current design.

Bibliography

[1] J. Conti et al. *International Energy Outlook 2014*. U.S. Energy Information Adminstration, 2014.

[2] C. Wolfram et al. *How will energy demand develop in the developing world*. National Bureau of Economic Research, 2012.

[3] Y. Fan et al. Exploring energy consumption and demand in China. *Energy*, 40:23–30, 2012.

[4] A. Ezeh et al. Global population trends and policy options. *The Lancet*, 380(9837):142–148, 2012.

[5] J. Olivier et al. *Trends in Global CO2 Emissions: 2012 Report*. Netherlands Environmental Assessment Agency, 2012.

[6] M. Hook et al. Depletion of fossil fuels and anthropogenic climate change-a review. *Energy Policy*, 52:797–809, 2013.

[7] P. Milan et al. Turbulent character of wind energy. *Physics Review Letters*, 110(138701), 2013.

[8] M. Singh et al. *Oscillation Damping: A Comparison of Wind and Photovoltaic Power Plant Capabilities*. Verband der Netzbetreiber, 2007.

[9] H. Berndt et al. Transmission code 2007. In *IEEE Symposium*, 2014.

[10] J. Pedraza et al. The use of hydropower plants for electricity generation in the European region, 2014.

[11] J. Lilley. *Nuclear Physics, Principles and Applications.* John Wiley & Sons, 2001.

[12] J. Freidberg. *Plasma Physics and Fusion Energy.* Cambridge University Press, 2007.

[13] M. Keilhacker et al. High fusion performance from deuterium-tritium plasmas in JET. *Nuclear Fusion*, 39(209), 1999.

[14] J.D. Strachan et al. Fusion Power Production from TFTR Plasmas Fueled with Deuterium and Tritium. *Physics Review Letters*, 72(22), 1994.

[15] S. Pfalzer. *An Introduction to Inertial Confinement Fusion.* Taylor & Francis, 2006.

[16] S. Atzeni. *The Physics of Inertial Fusion.* Oxford Science Publications, 2009.

[17] K. Miyamoto. *Controlled Fusion and Plasma Physics.* Taylor & Francis, 2007.

[18] C.M. Braams. *Nuclear Fusion.* Taylor & Francis, 2002.

[19] S. Wu et al. An overview of the EAST project. *Fusion Engineering and Design*, 82:436–471, 2014.

[20] G.S. Lee et al. Design and construction of the KSTAR tokamak. *Nuclear Fusion*, 41(10), 2001.

[21] A.A. Harms. *Principles of Fusion Energy.* World Scientific Publishing, 2000.

[22] K. Miyamoto. *Plasma Physics for Controlled Fusion.* Science and Culture Publishing, 2014.

[23] A. Herrmann et al. Energy flux to the ASDEX-Upgrade diverter plates determined by thermography and calorimetry. *Plasma Physics Controlled Fusion*, 37(17), 1995.

[24] M. Lehnen et al. Disruption heat loads and their mitigation in JET with the ITER-like wall. *Journal of Nuclear Materials*, 438:102–107, 2012.

[25] G. Pautasso et al. Chapter 12: Study of disruptions in ASDEX Upgrade. *Fusion Science and Technology*, 44(3), 2003.

[26] P.C. de Vries et al. Survey of disruption causes at JET. *Nuclear Fusion*, 51(053018), 2011.

[27] G. Pautasso et al. Disruption causes in ASDEX-Upgrade. In *41st EPS Conference on Plasma Physics*, page P2.015, 2014.

[28] M. Greenwald et al. Density limits in toroidal plasmas. *Plasma Physics Controlled Fusion*, 44:27–80, 2002.

[29] P.T. Lang et al. High density operation at JET by pellet refuelling. *Plasma Physics Controlled Fusion*, 44:1919–1928, 2002.

[30] R. Fitzpatrick et al. Stability of coupled tearing modes in tokamaks. *Nuclear Fusion*, 33:1049, 1993.

[31] F. Troyon et al. MHD-Limits to Plasma Confinement. *Plasma Physics Controlled Fusion*, 26:209, 1984.

[32] M. Kikuchi et al. Advanced scenarios in JT-60U: integration towards a reactor relevant regime. *Plasma Physics Controlled Fusion*, 21(A217), 2001.

[33] T.S. Taylor et al. Proc. 13th int. conf. on plasma physics and controlled nuclear fusion research. In *Nuclear Fusion Research*, 1990.

[34] B. Lipschultz et al. Review of MARFE phenomena in tokamaks. *Journal of Nuclear Materials*, 145:15–25, 1987.

[35] H.R. Wilson. Neoclassical Tearing Modes. *Fusion Science and Technology*, 53(153), 2008.

[36] L.L. Lao et al. Magnetohydrodynamic equilibria of attached plasmas after loss of vertical stability in elongated tokamaks. *Nuclear Fusion*, 31(10), 1991.

[37] V. Riccardo et al. Analysis of JET halo currents. *Plasma Physics Controlled Fusion*, 46(6), 2004.

[38] I. Semenov et al. High precision pick-up (Mirnov) coils for disruption studies in the T-11M and TCABR tokamaks. *Review of Scientific Instruments*, 70(1), 1999.

[39] G. Pautasso et al. On-line prediction and mitigation of disruptions in ASDEX Upgrade. *Nuclear Fusion*, 42(100), 2002.

[40] W. A. Bongers et al. ECE system on ASDEX-Upgrade placed inline at the high power waveguide based transmission system. *2009 34th International Conference on Infrared, Millimeter, and Terahertz Waves*, 63:1–2, 2009.

[41] G. Pautasso et al. ICPP and 25th EPS Conf. on Control Fusion and Plasma Physics. In *ECA*, 1998.

[42] M. Takechi et al. MHD instabilities leading to disruptions in low beta JT-60U reversed shear plasmas. *Nuclear Fusion*, 45:1694–1699, 2005.

[43] A. V. Nedospasov. Thermal quench in tokamaks. *Nuclear Fusion*, 48(032002), 2008.

[44] L. Spitzer. *Physics of Fully Ionized Gases: Second Revised Edition.* Interscience Publishers, 1962.

[45] W. Kegel. *Plasmaphysik.* Springer Verlag, 1998.

[46] G. Pautasso et al. Assimilation of impurities during massive gas injection in ASDEX Upgrade. *Nuclear Fusion*, 55(033015), 2015.

[47] V. Riccardo et al. Characterization of plasma current quench at JET. *Plasma Physics Controlled Fusion*, 47(1), 2005.

[48] M. Sugihara et al. Disruption scenarios, their mitigation and operation window in ITER. *Nuclear Fusion*, 47:337–352, 2007.

[49] P.C. de Vries et al. The impact of the ITER-like wall at JET on disruptions. *Plasma Physics Controlled Fusion*, 54(124032), 2012.

[50] T. C. Hender et al. Chapter 3: MHD stability, operational limits and disruptions. *Nuclear Fusion*, 47:128–202, 2007.

[51] D. A. Humphreys et al. Analytic modeling of axisymmetric disruption halo currents. *Physics of Plasmas*, 6(7), 1999.

[52] A. Tanga et al. Study of plasma disruptions in JET and its implications on engineering requirements. In *The 14th IEEE/NPSS Symposium Fusion Engineering*, pages 201–204, 1999.

[53] A. Vannucci et al. Forecast of TEXT plasma disruptions using soft X rays as input signal in a neural network. *Nuclear Fusion*, 39(2), 1999.

[54] A. Sengupta et al. Forecasting disruptions in the ADITYA tokamak using neural networks. *Nuclear Fusion*, 40(12), 1993.

[55] D. Wroblewski et al. Tokamak disruption alarm based on a neural network model of the high- beta limit. *Nuclear Fusion*, 37(6), 1997.

[56] F. Milani. *Disruption prediction at JET*. PhD thesis, Aston Univ., Birmingham (United Kingdom), 1998.

[57] A. Murari et al. Prototype of an adaptive disruption predictor for JET based on fuzzy logic and regression trees. *Nuclear Fusion*, 48(3), 2008.

[58] A. Murari et al. Unbiased and non-supervised learning methods for disruption prediction at JET. *Nuclear Fusion*, 49(5), 2009.

[59] Y. Zhang et al. Prediction of disruptions on ASDEX Upgrade using discriminant analysis. *Nuclear Fusion*, 51(063039), 2011.

[60] B.V. Kuteev et al. Impurity pellet injection systems for tokamak diagnostics and burn control. *Fusion Technology*, 26(18), 1994.

[61] P.T. Lang et al. Compact gas gun injection system for variable sized solid pellets. *Review of Scientific Instruments*, 65:2316–2321, 1994.

[62] M. Onozuka et al. Pneumatic Pellet Injector for JT-60. *Journal of Nuclear Science and Technology*, 27:1050–1057, 1990.

[63] L.R. Baylor et al. Pellet fuelling, ELM pacing and disruption mitigation technology development for ITER. *Nuclear Fusion*, 49(085013), 2009.

[64] P. Parks et al. High velocity liquid jet injection into tokamak plasmas for disruption mitigation. *Fusion Technology*, 35, 1999.

[65] S. Combs et al. Fast-opening, high-throughput gas valve and application for inertial fusion energy R&D. *Review of Scientific Instruments*, 75:270–272, 2004.

[66] U. Kruezi et al. Massive Gas Injection Experiments at JET - Performance and Characterisation of the Disruption Mitigation Valve. *EFDA Report*, 2009.

[67] S. Combs et al. Alternative Techniques for Injecting Massive Quantities of Gas for Plasma-Disruption Mitigation. *IEEE Transactions on Plasma Science*, 38:400–405, 2010.

[68] G. Martin et al. Disruption Mitigation on Tore Supra. In *20th IAEA Int. Conf. on Fusion Energy*, page P2.015, 2004.

[69] A.J. Thornton et al. Plasma profile evolution during disruption mitigation via massive gas injection on MAST. *Nuclear Fusion*, 52(063018), 2012.

[70] S.A. Bozhenkov et al. Main characteristics of the fast disruption mitigation valve. *Review of Scientific Instruments*, 78(033503), 2007.

[71] D.G. Whyte et al. Disruption mitigation on Alcator C-Mod using high-pressure gas injection: Experiments and modeling towards ITER. *Nuclear Materials*, 363:1160–1167, 2007.

[72] S.L. Milora et al. Fast-opening magnetic valve for high pressure gas injection and applications to hydrogen pellet fuelling systems. *Review of Scientific Instruments*, 57(2356), 1986.

[73] G. Pautasso et al. Plasma shut-down with fast impurity puff on ASDEX Upgrade. *Nuclear Fusion*, 47:900–913, 2007.

[74] E.M. Hollmann et al. Measurement of impurity and heat dynamics during noble gas jet-initiated fast plasma shutdown for disruption mitigation in DIII-D. *Nuclear Fusion*, 45(1046), 2005.

[75] M. Lehnen et al. Disruption Mitigation by Massive Gas Injection in JET. *Nuclear Fusion*, 51(123010), 2011.

[76] A.J. Thornton et al. Characterization of disruption mitigation via massive gas injection on MAST. *Plasma Physics Controlled Fusion*, 54(125007), 2012.

[77] C. Reux et al. Experimental study of disruption mitigation using massive injection of noble gases on Tore Supra. *Nuclear Fusion*, 50(09006), 2010.

[78] R. Granez et al. Gas jet disruption mitigation studies on Alcator C-Mod. *Nuclear Fusion*, 46:1001–1008, 2006.

[79] G. Pautasso et al. Disruption studies in ASDEX Upgrade in view of ITER. *Plasma Physics Controlled Fusion*, 51(124056), 2009.

[80] G. Pautasso et al. Contribution of ASDEX Upgrade to disruption studies for ITER. *Nuclear Fusion*, 51(103009), 2011.

[81] E.M. Hollmann et al. Measurements of injected impurity assimilation during massive gas injection experiments in DIII-D. *Nuclear Fusion*, 48(115007), 2008.

[82] H. P. Summers. *ADAS User Manual*, 2004.

[83] N.Commaux et al. Radiation asymmetries during disruptions on DIII-D caused by massive gas injection. *Physics of Plasmas*, 21(10), 2014.

[84] G. Pautasso et al. Disruption mitigation by injection of small quantities of noble gas in ASDEX Upgrade. *Plasma Physics Controlled Fusion*, 59(014046), 2016.

[85] P.L. Taylor et al. Disruption mitigation studies in DIII-D. *Physics of Plasmas*, 6(1872), 1999.

[86] S.A. Bozhenkov et al. Generation and suppression of runaway electrons in disruption mitigation experiments in TEXTOR. *Plasma Physics Controlled Fusion*, 50(10), 2008.

[87] G. Pautasso et al. Generation and suppression of runaway electrons in ASDEX Upgrade disruptions. In *42nd EPS Conference on Plasma Physics*, page P1.134, 2015.

[88] R.D. Gill et al. Direct observations of runaway electrons during disruptions in the JET tokamak. *Nuclear Fusion*, 40(163), 2000.

[89] S.A. Bozhenkov et al. Fueling efficiency of massive gas injection in TEXTOR: mass scaling and importance of gas flow dynamics. *Nuclear Fusion*, 51(083033), 2011.

[90] Schnorr. Datenblatt Tellerfedern. `http://www.schnorr.de/fileadmin/downloads/de/schnorr_pb_de_s10-19.pdf`, 2012.

[91] Witzenmann GmbH. Metal Hose Manual. `http://www.witzenmann.de/repo/assets/1301uk_7_03_16_10Handbuchms96dpi.pdf`, 2014.

[92] Physik Instrumente GmbH. Picma stack multilayer piezo actuators. `https://www.piceramic.de/de/produkte/piezokeramische-aktoren/linearaktoren/p-882-p-888-picma-stack-multilayer-piezoaktoren-100810/`, 2016.

[93] U. Kruezi et al. Supersonic helium beam diagnostic for fluctuation measurements of electron temperature and density at the Tokamak TEXTOR. *Review of Scientific Instruments*, 83(065107), 2012.

[94] Piezosystem Jena. PX-500. `https://www.piezosystem.de/produkte/piezoaktoren/x-positionierer/px-500`, 2015.

[95] Noliac. NAC2023. http://www.noliac.com/products/actuators/plate-stacks/show/nac2023-hxx/, 2016.

[96] Thyssen-Krupp. Data sheet Ti gr.5. http://www.thyssenkrupp.ch/documents/Titan_Grade_5.pdf, 2016.

[97] L. S. Zolin et al. Forming and Trapping of gasious hydrogen jet in a vacuum. *Cryogenics*, 8:143–148, 1968.

[98] Vision Research. Phantom v711. https://www.phantomhighspeed.com/Products/v-Series-Cameras/v711, 2012.

[99] M. Reich et al. Lithium beam charge exchange diagnostic for edge ion temperature measurements at the ASDEX Upgrade tokamak. *Plasma Physics Controlled Fusion*, 46(797), 2004.

[100] A. Thoma et al. Spectroscopic measurements of tungsten erosion in the ASDEX Upgrade divertor. *Plasma Physics Controlled Fusion*, 39(9), 1997.

[101] I. Zammuto et al. Long term project in ASDEX Upgrade: Implementation of ferritic steel as in vessel wall. *Fusion Engineering and Design*, 98:1419–1422, 2015.

[102] G. Haas et al. In vessel pressure measurement in nuclear fusion experiments with ASDEX gauges. *Vacuum*, 51:39–46, 1998.

[103] M. Bernert et al. Application of axuv diode detectors at ASDEX Upgrade. *Review of Scientific Instruments*, 85(033503), 2014.

List of Requirements

This appendix contains the complete list of requirements for the new MGI valves in agreement with the VDE guidelines.

Max-Planck Institut for Plasmaphysics

List of Requirements

for

- MGI Gas Valve -

Team members:
Mathias Dibon
Gabriella Pautasso
Michael Beck

Organization		Process		Requirements	Valence			
Number	Name	Type	Phase		Minimum fulfillment	Target fulfillment	Ideal fulfillment	Unit of measure
				Physical-Technical Function				
F01	DI	R	P	No magnetic fields				
F02	DI	R	D	No magnetic components	μ<1,05			
F03	DI	R	C	Powersupply	400	200	120	V
F04	DI	R	D	Small size	150x150x150	120x120x120	100x100x100	mm
F05	DI	R	D	Small gas reservoir	80	50	30	cm^3
F06	DI	R	P	Opening time	4	3	2	ms
F07	DI	R	F	Fast gas evacuation	15	10	7	ms
F08	DI	R	C	Explosion prevention				
F09	DI	R	D	No materials that absorb D_2/ react with D_2				
F10	DI	R	D	Withstand certain temperatures	150	160	170	°C
F11	DI	R	F	Leaking rate	$>10^{-9}$	$>10^{-10}$	$<10^{-11}$	Pam^3/s
F12	DI	W	C	Withstand neutron irradiation				
F13	DI	R	D	Position control of the valve piston	Open-close		Movement recorder	
				Technology				
T01	EI	R	D	Manufacturing	Outside	On site (ITZ)	On site (E1)	
T02	DI,BE	R	D	Assembly	Outside	On site (E1)	On site (Pel)	
T03	DI	W	D	Quality control	Special equipme.	Standart equipme.		
T04	DI	W	D	Standardized parts	No	Yes (>50%)	Yes (>70%)	
T05	DI,BE	W	D	Kind of assembly	By additional device	By hand		

Types: R-Requirement; W-Wish; Phases: P - Principle; C - Concept; D - Design; F – Final design
Shortcuts of team members: DI = Mathias Dibon; BE = Michael Beck

Max-Planck Institut for Plasmaphysics

List of Requirements

for

- MGI Gas Valve -

Team members:
Mathias Dibon
Gabriella Pautasso
Michael Beck

Organization		Process		Requirements	Valence			
Number	Name	Type	Phase		Minimum fulfillment	Target fulfillment	Ideal fulfillment	Unit of measure
				Economics				
W01	DI	R	C	Lifetime of the valve	> 5	> 7	> 10	years
W02	DI	W	D	Total cost for materials	30.000	20.000	15.000	€
W03	DI	W	F	Decomissioning / Recycling				
W04	DI	R	D	Manufacturing time	10	5	2	months
W05	DI	R	D	Maintenance time	≤ 12	≤ 8	≤ 2	hours
				Man-Machine-Interaction				
M01	DI	R	C	Concealment of moving parts				
M02	DI,BE	W	K	Maintenance cycle	1	2	5	years
M03	DI,BE	W	P	Easy operation				
M04	DI,BE	R	F	Fast implementation in existing systems				
M05	DI	R	F	Documentation				
M06	DI	R	F	Type of interface	Analogue modules	S7	WinCC + S7	

Types: R-Requirement; W-Wish; Phases: P - Principle; C - Concept; D - Design; F – Final design
Shortcuts of team members: DI = Mathias Dibon; BE = Michael Beck

07.08.2014

Responsible: Dibon

Outgoing: Date

Version: 1 07.08.2014

S7 programs for the durability tests

This appendix contains the complete STEP7 programs for the durability tests of the spring-driven valve and the piezo-driven valve.

Prozesskette Dauertest Mankventil

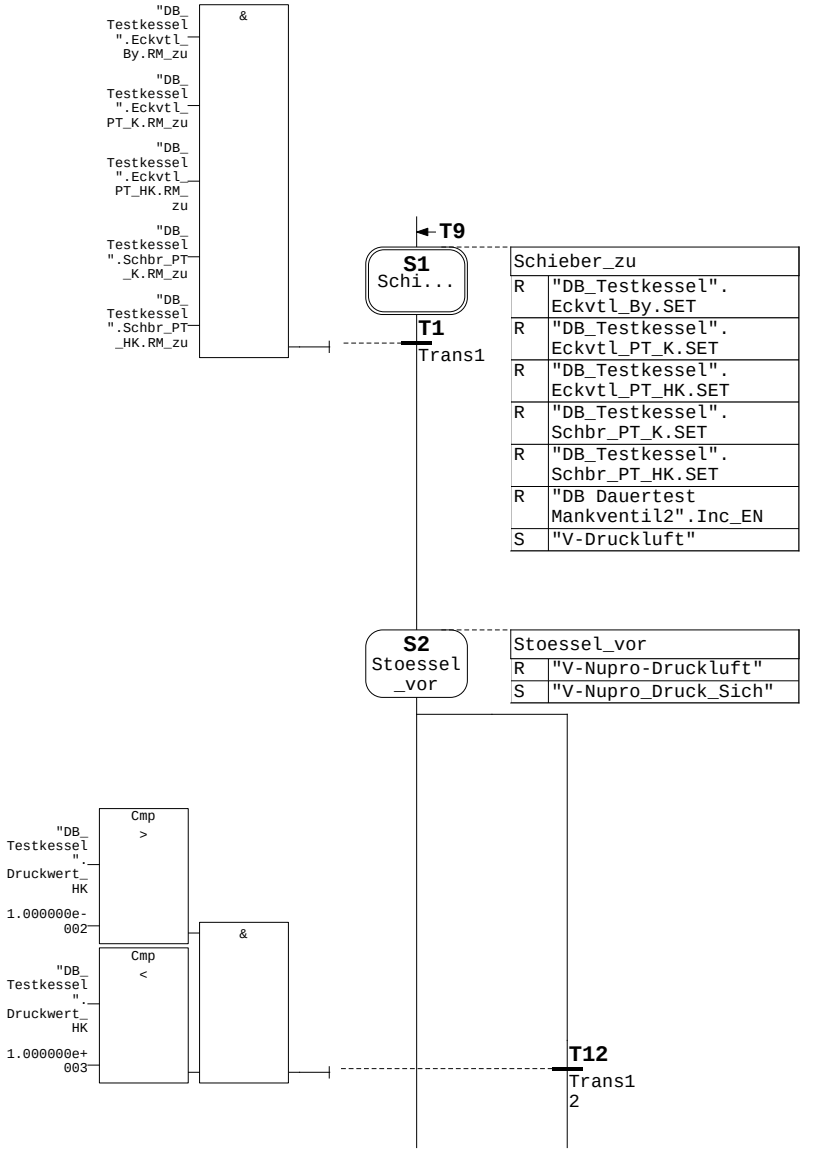

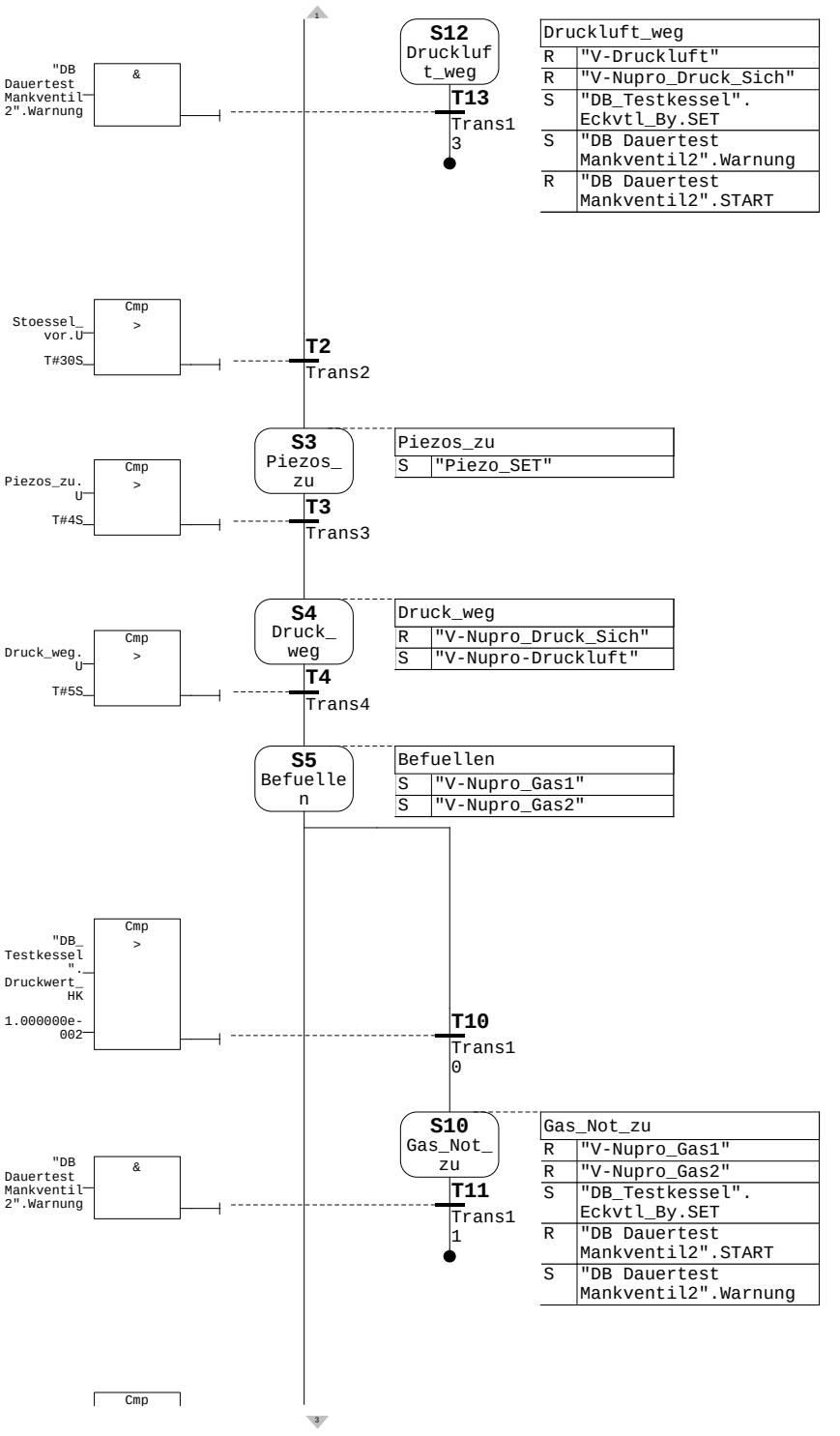
1
"DB Dauertest Mankventil 2".Warnung
&
S12
Druckluf t_weg
T13
Trans1 3
Druckluft_weg
R "V-Druckluft"
R "V-Nupro_Druck_Sich"
S "DB_Testkessel". Eckvtl_By.SET
S "DB Dauertest Mankventil2".Warnung
R "DB Dauertest Mankventil2".START
Stoessel_ vor.U
Cmp >
T#30S
T2
Trans2
S3
Piezos_ zu
Piezos_zu
S "Piezo_SET"
Piezos_zu. U
Cmp >
T#4S
T3
Trans3
S4
Druck_ weg
Druck_weg
R "V-Nupro_Druck_Sich"
S "V-Nupro-Druckluft"
Druck_weg. U
Cmp >
T#5S
T4
Trans4
S5
Befuelle n
Befuellen
S "V-Nupro_Gas1"
S "V-Nupro_Gas2"
"DB_ Testkessel ". Druckwert_ HK
Cmp >
1.000000e-002
T10
Trans1 0
S10
Gas_Not_ zu
Gas_Not_zu
R "V-Nupro_Gas1"
R "V-Nupro_Gas2"
S "DB_Testkessel". Eckvtl_By.SET
R "DB Dauertest Mankventil2".START
S "DB Dauertest Mankventil2".Warnung
"DB Dauertest Mankventil 2".Warnung
&
T11
Trans1 1
Cmp
3

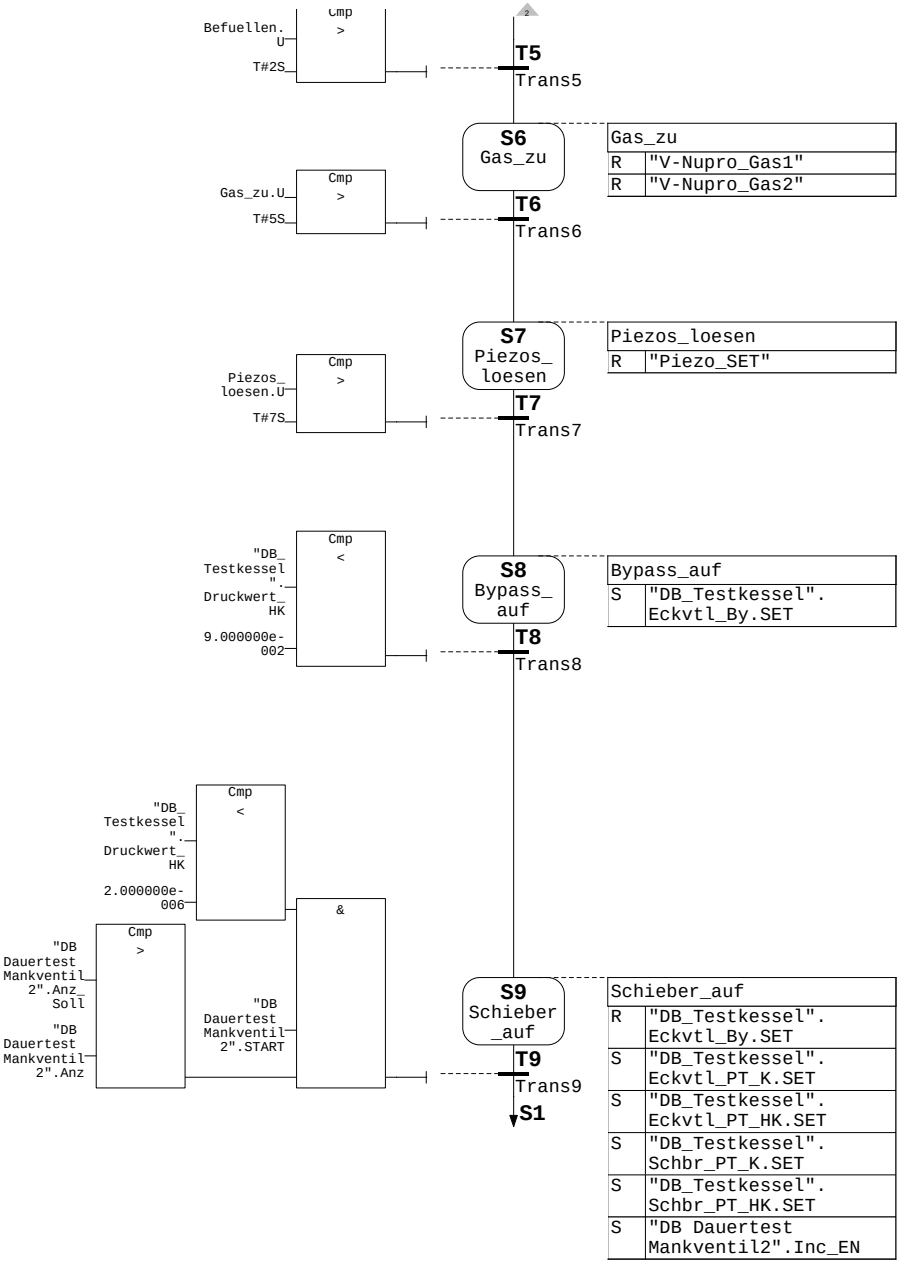
Cmp
>
Befuellen.
U
T#2S
T5
Trans5
S6
Gas_zu
Gas_zu
R "V-Nupro_Gas1"
R "V-Nupro_Gas2"
Cmp
>
Gas_zu.U
T#5S
T6
Trans6
S7
Piezos_
loesen
Piezos_loesen
R "Piezo_SET"
Cmp
>
Piezos_
loesen.U
T#7S
T7
Trans7
Cmp
<
"DB_
Testkessel
".
Druckwert_
HK
9.000000e-
002
S8
Bypass_
auf
Bypass_auf
S "DB_Testkessel".
Eckvtl_By.SET
T8
Trans8
Cmp
<
"DB_
Testkessel
".
Druckwert_
HK
2.000000e-
006
Cmp
>
"DB
Dauertest
Mankventil
2".Anz_
Soll
"DB
Dauertest
Mankventil
2".Anz
&
"DB
Dauertest
Mankventil
2".START
S9
Schieber
_auf
Schieber_auf
R "DB_Testkessel".
Eckvtl_By.SET
S "DB_Testkessel".
Eckvtl_PT_K.SET
S "DB_Testkessel".
Eckvtl_PT_HK.SET
S "DB_Testkessel".
Schbr_PT_K.SET
S "DB_Testkessel".
Schbr_PT_HK.SET
S "DB Dauertest
Mankventil2".Inc_EN
T9
Trans9
S1

Prozesskette Dauertest Piezoventil

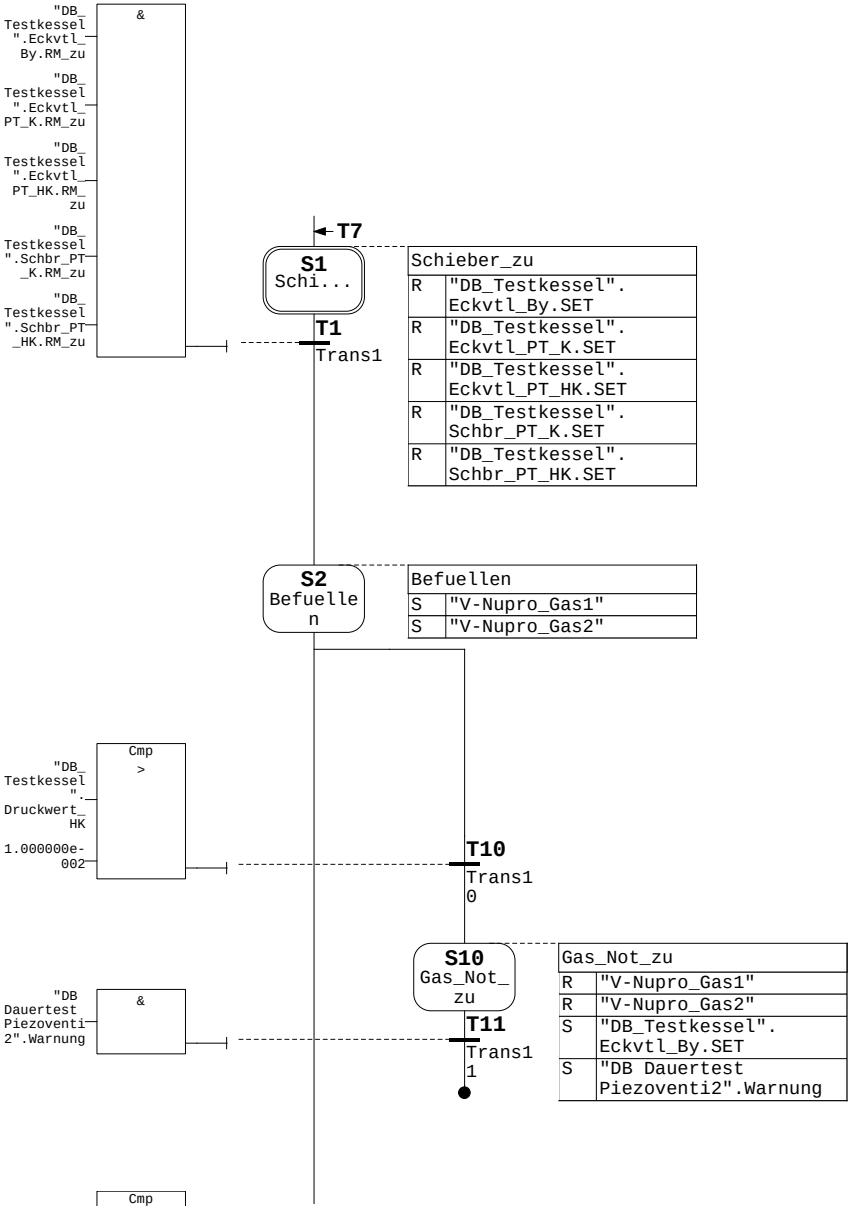

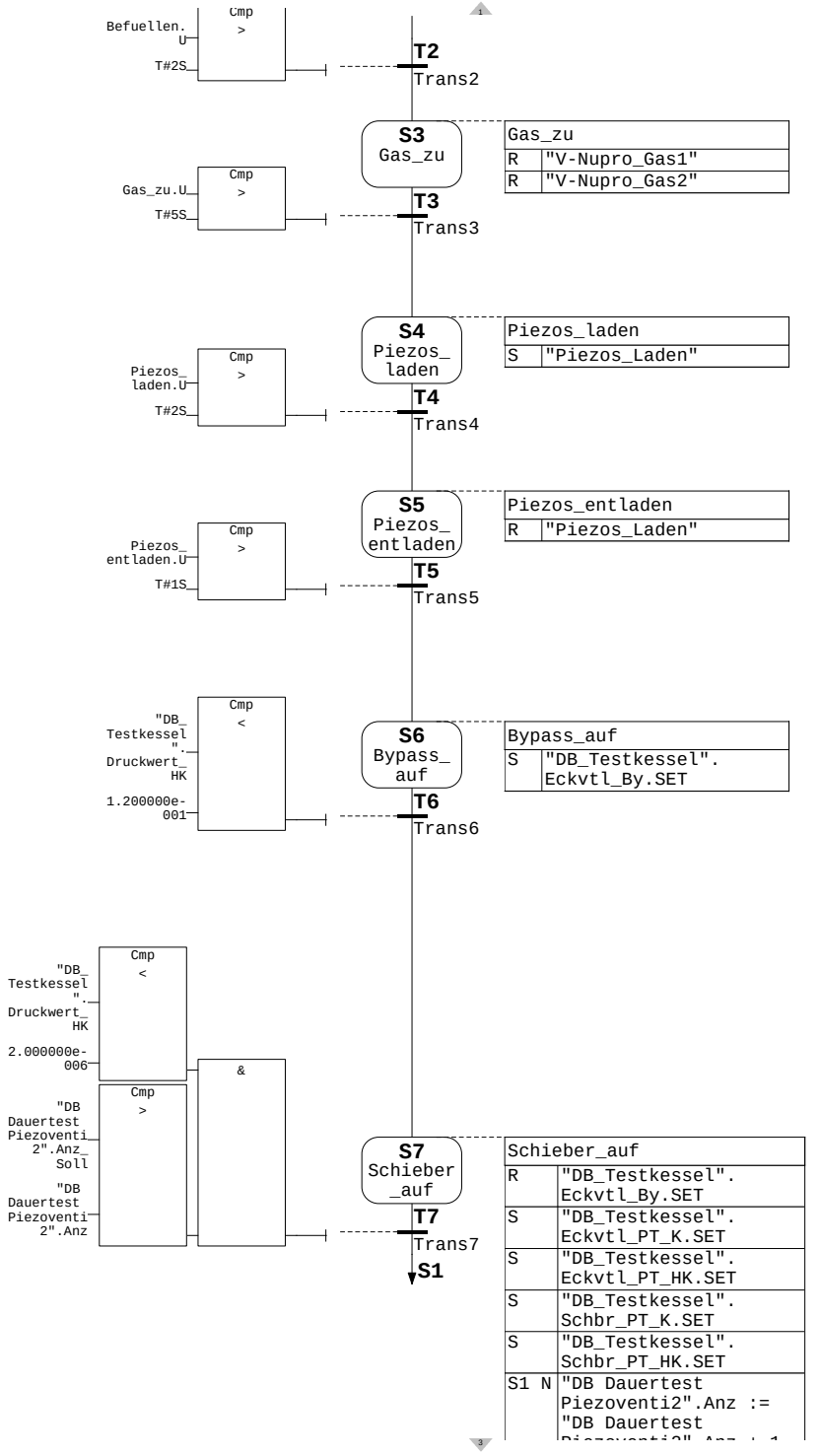
Cmp >
Befuellen.U
T#2S
T2
Trans2
S3
Gas_zu
Gas_zu
R "V-Nupro_Gas1"
R "V-Nupro_Gas2"
Cmp >
Gas_zu.U
T#5S
T3
Trans3
S4
Piezos_laden
Piezos_laden
S "Piezos_Laden"
Cmp >
Piezos_laden.U
T#2S
T4
Trans4
S5
Piezos_entladen
Piezos_entladen
R "Piezos_Laden"
Cmp >
Piezos_entladen.U
T#1S
T5
Trans5
S6
Bypass_auf
Bypass_auf
S "DB_Testkessel".Eckvtl_By.SET
Cmp <
"DB_Testkessel".Druckwert_HK
1.200000e-001
T6
Trans6
Cmp <
"DB_Testkessel".Druckwert_HK
2.000000e-006
Cmp >
"DB Dauertest Piezoventi 2".Anz_Soll
"DB Dauertest Piezoventi 2".Anz
&
S7
Schieber_auf
Schieber_auf
R "DB_Testkessel".Eckvtl_By.SET
S "DB_Testkessel".Eckvtl_PT_K.SET
S "DB_Testkessel".Eckvtl_PT_HK.SET
S "DB_Testkessel".Schbr_PT_K.SET
S "DB_Testkessel".Schbr_PT_HK.SET
S1 N "DB Dauertest Piezoventi2".Anz := "DB Dauertest
T7
Trans7
S1

Valve trigger circuits

.1 Manual operation circuit for spring-driven valves

This circuit was built for the first tests of the new spring-driven valve. The PE stacks are charged slowly when the switch "Piezo-Laden" is flipped. For this, the circuit uses an external power source that supplies the necessary 120 V. Once the stacks are charged, the switch "Piezo-Laden" is flipped back and the valve is armed. When the switch "Piezo-Entladen" is used, the stacks are discharged rapidly. This circuit also allows monitoring the voltage applied to each pair of PE stacks. Hence, one can observe when the stacks are charged completely and if they discharge abruptly. This allows checking whether all stacks operate normally or if they malfunction.

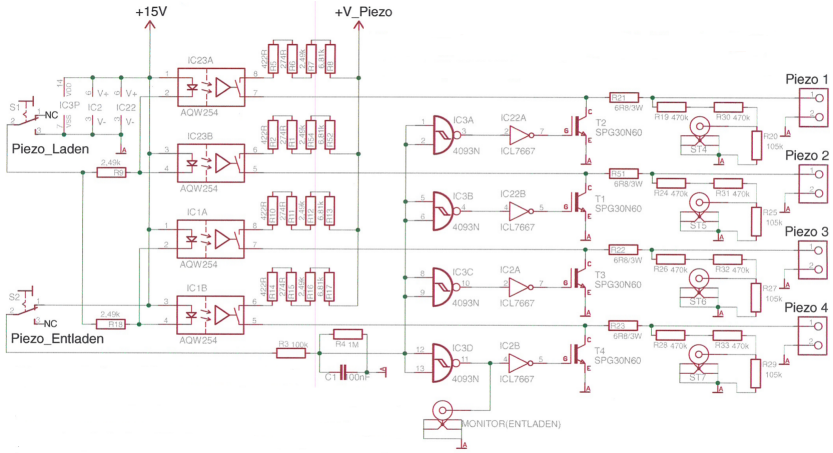

Figure 1: Scheme of the control circuit for manual operation of the spring-driven valves

.2 Circuit for automated control of spring-driven valves

To operate the valve using the SIMATIC S7 control system, the valve has to be triggered by a digital 24 V output signal. For this purpose, a trigger circuit was developed, that allows charging and rapid discharging of the PE stacks by supplying 24 V signals. The necessary 120 V for the PE stacks is generated by an integrated power module. Each pair of PE stacks is charged and discharged individually and the current to each pair is measured. If a significant current is flowing in one of the PE circuits after the stacks have been charged, the circuit gives out a signal to the control system that a pair of stacks is malfunctioning.

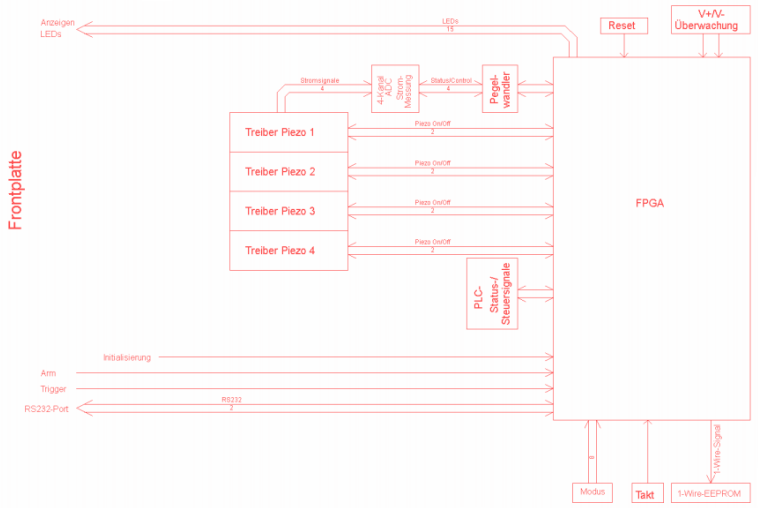

Figure 2: Scheme of the control circuit for automated operation of the spring-driven valves

.3 Manual operation circuit for piezo-driven valves

A simple capacitor circuit was built to allow instant charging of the piezo-electric stack actuators. In the idle state, two parallel capacitors with a total capacity of 4400 µF are charged and the PE stacks are short-circuited over a resistor with 7.5 kΩ. When the switch is turned, the capacitors are connected parallel to the PE stacks, sharing the charge immediately. The resulting voltage is calculated by Eq. C.1.

$$U_{out} = U_{in} * \frac{4400\mu F}{4400\mu F + C_{Piezo}} \tag{1}$$

Since the capacity of the PE stacks is much smaller than that of the capacitors, the external supply voltage only has to be a few volts above 200 V to achieve the necessary voltage of 200 V. This equation is also used to measure the total capacity of the PE stacks by fixing U_{in} and measuring $Uout$. The test actuator has a capacity of 120 µF and the valve actuator 180 µF. When the

switch is turned again, the capacitors are recharged and the PE stacks are discharged on a resistive time scale. The resistor prevents rapid discharging which could damage the ceramic.

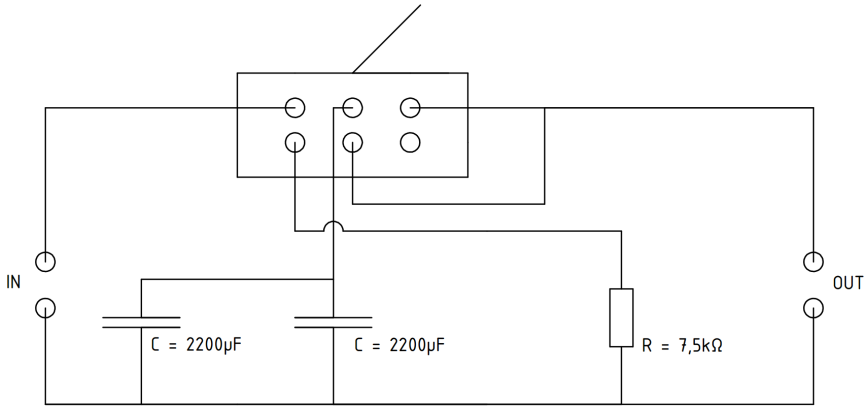

Figure 3: Scheme of the manual capacitor circuit used to charge PE stacks abruptly

.4 Circuit for automated control of piezo-driven valves

For the operation of the piezo-driven valve via the SIMATIC S7 control system, a circuit was developed which can rapidly charge the PE stacks when a digital 24 V input signal is applied. An integrated 200 V power supply charges a bank of parallel capacitors with a total capacity of 3120 µF. The 24 V signal is applied and a semiconductor relay switches the PE stacks parallel to the capacitors, charging the stacks. An internal inductance limits the current to protect the relay although the charging time is extended. When the trigger signal is not applied, the capacitors are recharged which can take up to 2 minutes due to the low current of the power supply and the PE stacks are discharged over 100 kΩ resistors.

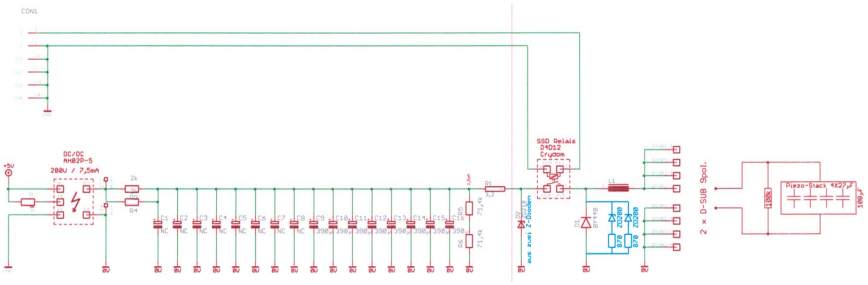

Figure 4: Scheme of the automated capacitor circuit used to charge PE stacks abruptly

Assembly for leak check of viton seal

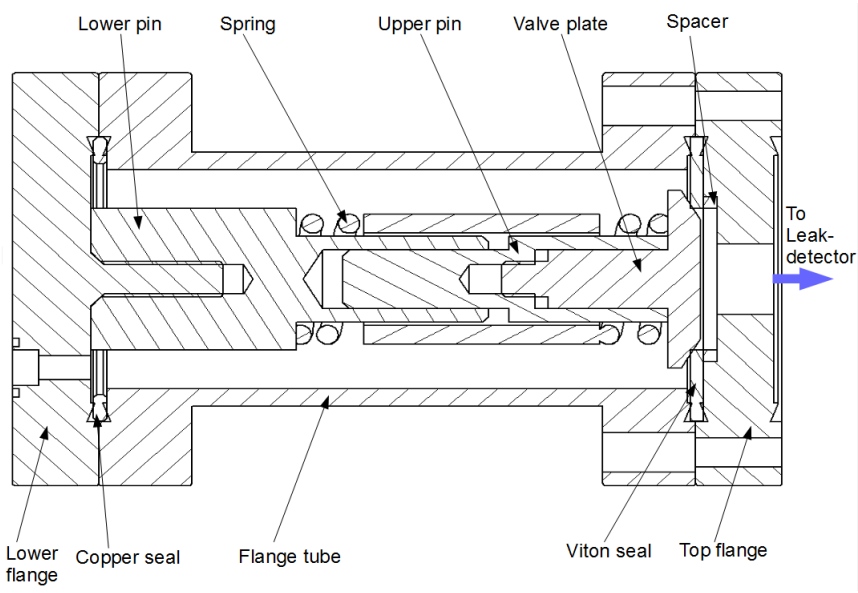

Figure 5: Cross-section of the assembly used for leak rate investigations of the viton seal

The leak check was conducted using the assembly displayed in figure D.1. The lower pin is screwed onto the lower CF40 flange, which is connected to the tube and sealed off by a copper seal. Valve plate and upper pin are also

connected. The upper pin is guided in a drilling in the lower pin. To reduce friction both pins are made of brass with a high surface quality. A spring with a spring rate of 21.5 $\frac{\mathrm{N}}{\mathrm{mm}}$ is placed between the valve plate and the lower pin. The viton seal is fastened between the top flange and the tube. A recess in the top flange allows the installation of additional parts in front of the seal. The length of the lower pin is chosen as such that the spring is almost completely relaxed and the conical edge of the valve plate rests with minimal force on the viton sealing edge. A drilling and a second CF40 sealing edge allow the attachment of a leak detector. The spring force and thus the force acting on the viton seal can be increased stepwise by adding thin steel discs between the lower pin and the spring. The discs have a thickness of 0.5 mm which corresponds to an additional force of 10.5 N. Gas can be injected into the tube by a VCR connector (not displayed) welded into the bottom flange.

Calculation procedure for jxB forces

This appendix contains the standard calculation procedure for jxB forces during disruptions at ASDEX Upgrade.

Kraft und Drehmoment auf eine leitfähige Platte infolge der Wechselwirkung induzierter Ströme mit einem statischen Magnetfeld.

- Die Berechnung basiert auf einem Vortrag von U. Seidel (AUG – Konstrukteurssitzung am 12. Februar 2007)
- 2016 – Korrektur bei der Kraftrechnung l=y auf l=2y

Allgemeines

Die Lorentzkraft bewirkt eine Kraft, die senkrecht auf der Ebene steht, die durch das wirkenden Magnetfeld und einem Strom aufgespannt wird.

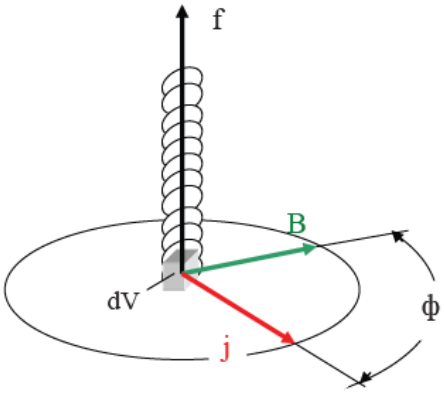

Fig. 1 Schematische Darstellung der Kraftwirkung.

$$\vec{f}_V = \vec{j} \times \vec{B} \qquad \text{(Gl. 1)}$$

$$f_V = j \cdot B \cdot \sin(\phi)$$

$$f_V / \frac{N}{m^3} = j / \frac{A}{m^2} \cdot B / T \cdot \sin(\phi) \cdot$$

Für linienhafte Ströme (Spulen etc.) gilt: $f_l / {}^{N}\!/_{m} = {}^{I}\!/_{A} \times {}^{B}\!/_{T}$ bzw. ${}^{F}\!/_{N} = {}^{I}\!/_{A} \cdot {}^{B}\!/_{T} \cdot \sin(\Phi) \cdot {}^{l}\!/_{m}$, wobei l die Länge des Strompfades ist.

Ein zeitlich veränderliches Magnetfeld induziert eine Spannung im durchdrungenen Körper mit der Fläche A_{ind} senkrecht zu dB_v/dt $U_{ind} = \frac{dB_v}{dt} \cdot A_{ind}$. Diese Spannung wiederum treibt einen Strom $I_s = \frac{U_{ind}}{R_r}$. Existiert jetzt noch ein externes Magnetfeld so wirkt auf die Platte die Lorentzkraft (Gl. 1, Fig. 1).

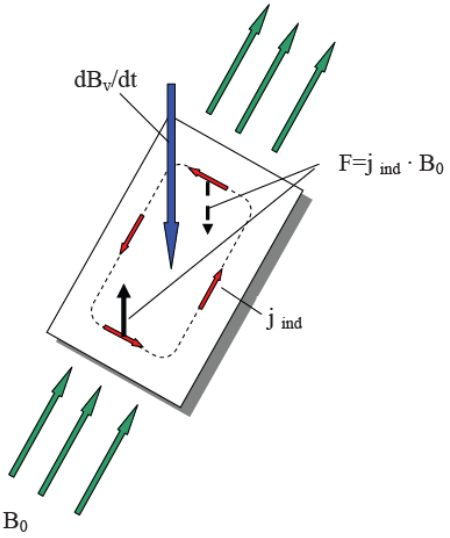

Fig. 2 Schematische Darstellung für das Induktionsgesetz und die Wirkung der Lorentzkraft.

Zeitverhalten

Das Anwachsen des induzierten Stromes geschieht nicht unendlich schnell sondern wird durch die Induktivität der Platte und ihrem Widerstand gebremst. $j_{ind} = j_{\max}\ (1 - e^{-t/\tau})$ mit $\tau = \frac{L}{R}$.

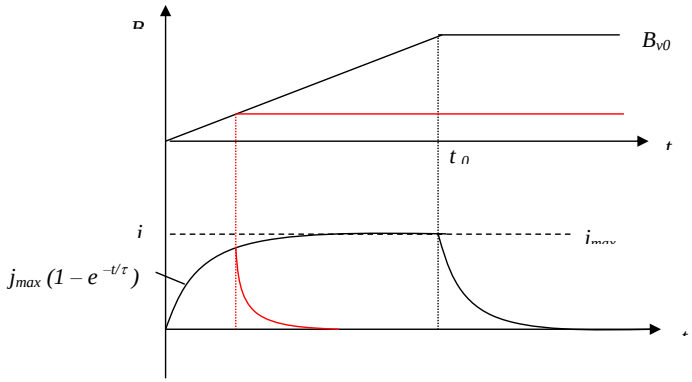

Fig. 3: Schematische Darstellung des Stromanstiegs.

Mit der Induktivität, $L = \frac{\mu_0 \mu_r n^2 A_q}{l}$ und dem elektrischen Widerstand, $R = \frac{\rho \cdot l}{A_q}$

Für eine unmagnetische Platte ($\mu_r = 1$, n=1) folgt mit $\mu_0 = 4\pi 10^{-7} \frac{Vs}{Am}$ für die Zeitkonstante, $\tau = \frac{\mu_0}{\rho}\left(\frac{A_q}{l}\right)^2$.

Berechnung von Kraft und Moment – stationär

Für die folgenden Abschätzungen wird angenommen, dass die Zeitkonstante τ hinreichend klein gegenüber der Dauer der Magnetfeldänderung ist ($\tau \leq 0.3 \cdot t_0$). Somit wird der maximal mögliche Strom getrieben. Eine kürzere Pulsdauer bzw. größere Zeitkonstante resultiert in einem geringeren induzierten Strom und demzufolge einer geringeren wirkenden Kraft/Drehmoment.

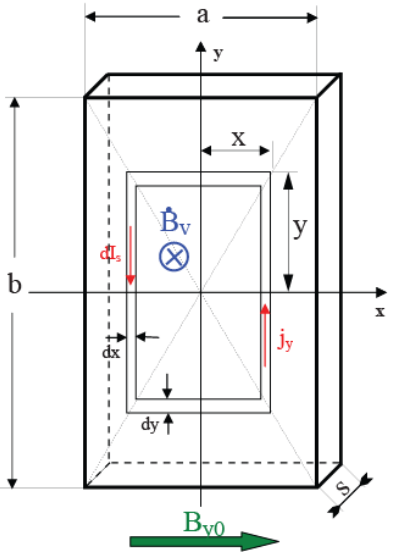

Fig. 4. Schematische Darstellung der Plattengeometrie und des Koordinatensystems.

Bei der Platte, auf die ein Drehmoment wirkt handelt es sich um einen Quader mit den Kantenlängen a, b und s. Das statische Magnetfeld wirkt entlang der x-Achse (Ausdehnung a). Das zeitlich veränderliche Magnetfeld wirkt entlang der Ausdehnung s. Die in y-Richtung fließende Komponente des induzierten Stromes trägt zur Kraftwirkung bei. Der Zusammenhang zwischen x und y ist gegeben durch: $\frac{dy}{dx} = \frac{y}{x} = \frac{b}{a}$.

Die Rahmenfläche, welche vom veränderlichen B-Feld durchdrungen ist, ergibt sich zu: $A_r = 4 \cdot x \cdot y$. Mit $y = \frac{b}{a} x$ folgt daraus: $A_r = 4 \cdot \frac{b}{a} x^2$. (Gl. 2)

Der zugehörige Rahmenwiderstand berechnet sich aus $R_r = \frac{\rho l}{A_q}$. Mit einer Gesamtlänge der Stromschleife von $l = 2(2x + 2y) = 4x\left(1 + \frac{b}{a}\right) = 4x\frac{b}{a}\left(1 + \frac{a}{b}\right)$ und der Querschnittsfläche $A_q = s\,dx$ folgt: $R_r = \frac{4\rho}{s}\frac{x}{dx}\frac{b}{a}\left(1 + \frac{a}{b}\right)$. (Gl. 3)

Hierbei ist ρ spezifische elektrische Widerstand.

Für den durch das veränderliche magnetische Feld getriebenen Strom $dI_s = \frac{U_{ind}}{R_r}$ ergibt sich mit $U_{ind} = \dot{B}_v \cdot A_r$: $dI_s = \frac{\dot{B}_v \cdot A_r}{R_r}$ bzw. unter Verwendung von Gl. 2 und Gl. 3 für Rahmenfläche und –widerstand:

$$dI_s = \frac{\dot{B}_v \cdot A_r}{R_r} = \dot{B}_v \cdot \frac{s}{\rho} \cdot \frac{1}{\left(1 + a/b\right)} \cdot x \cdot dx \qquad \text{(Gl. 4)}$$

Die Stromdichte in der für die Kraft wirksamen y-Richtung ist somit:

$$j_y = \frac{dI_s}{s \cdot dx} = \dot{B}_v \cdot \frac{1}{\rho} \cdot \frac{1}{\left(1 + a/b\right)} \cdot x$$

Die Kraftverteilung entlang x ist somit, $df = dI_y \cdot B_{y0} \cdot 2y = j_y \cdot s \cdot dx \cdot B_{y0} \cdot 2y$, bzw.:

$$df = 2 j_y \cdot B_{y0} \cdot s \cdot b/a \cdot x \cdot dx = 2 B_{y0} \cdot \dot{B}_v \cdot \frac{s}{\rho} \cdot \frac{b/a}{\left(1 + a/b\right)} \cdot x^2 \cdot dx$$

Die Gesamtkraft auf die halbe Platte ergibt sich durch Integration entlang x zu:

$$F_{tot} = \int_0^{a/2} df(x) = 2B_{y0} \cdot \dot{B}_v \cdot \frac{s}{\rho} \cdot \frac{b/a}{\left(1 + a/b\right)} \int_0^{a/2} x^2 dx = 2B_{y0} \cdot \dot{B}_v \cdot \frac{s}{\rho} \cdot \frac{b/a}{\left(1 + a/b\right)} \frac{x^3}{3}\Big|_0^{a/2}, \text{ bzw.:}$$

$$F_{tot} = B_{y0} \cdot \dot{B}_v \cdot \frac{s}{\rho} \cdot \frac{b/a}{\left(1 + a/b\right)} \cdot \frac{a^3}{12} \qquad \text{(Gl. 5)}$$

Das Moment, welches auf die halbe Platte wirkt ist das Integral über Kraft x Hebelarm und somit: $M_{halb} = \int_0^{a/2} x \cdot df(x) = B_{y0} \cdot \dot{B}_v \cdot \frac{s}{\rho} \cdot \frac{b/a}{\left(1 + a/b\right)} \cdot \frac{a^4}{32}$ bzw. $M_{halb} = \frac{3}{8} a \cdot F_{tot}$

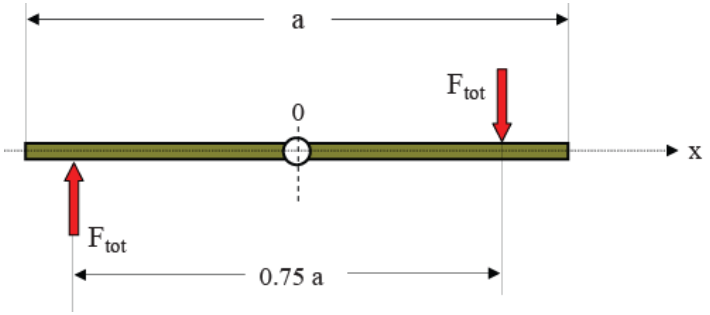

Fig. 5. Hebelverhältnisse zur Bestimmung von $M_{tot.}$

Da die Kraft wegen der unterschiedlichen Stromrichtung in den beiden Plattenhälften nach oben bzw. unten wirkt ist das resultierende Drehmoment: $M_{tot} = 2 \cdot M_{halb} = 3/4\, a\, F_{tot}$

bzw.: $M_{tot} = B_{y0} \cdot \dot{B}_v \cdot \frac{s}{\rho} \cdot \frac{b/a}{\left(1 + a/b\right)} \cdot \frac{a^4}{16}$ (Gl. 6)

Berechnung von Kraft und Moment – $t_{dur} << t_{skin}$

Wenn die Skinzeit groß gegen die Dauer der Disruption ist, kann/muss die auf eine Platte wirkende Kraft und das Moment auf eine andere Art abgeschätzt werden. Dieser liegt zugrunde, dass im Fall einer sehr schnellen Disruption das vor der Disruption anliegende B-Feld eingefroren ist (auf Skin-Zeitskalen).

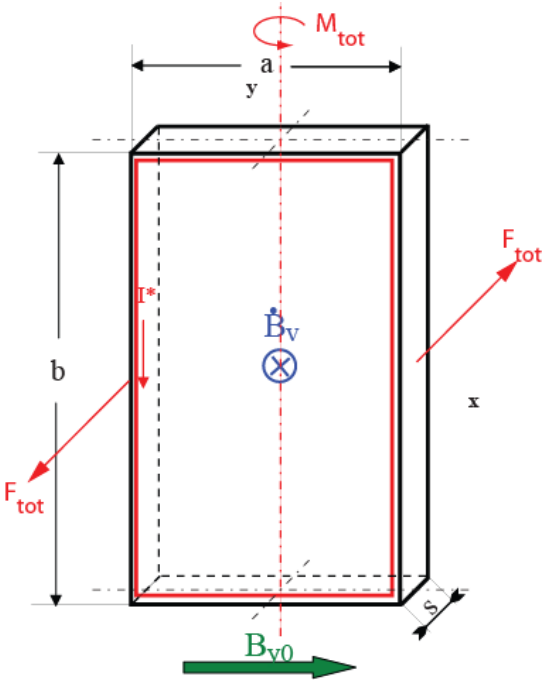

Fig. 6. Schematische Darstellung der Plattengeometrie und des Koordinatensystems für die Skinzeit dominierte Abschätzung.

Das anliegende Vertikalfeld vom Plasmastrom B_v wird in der Platte bei einer Disruption durch den induzierten Oberflächenstrom I* aufrechterhalten. $I^* = H = B_v / \mu_0$. Der Gesamtstrom ergibt sich durch die Überlagerung der Oberflächenströme entlang s zu: $I = I^* s$. Die Senkrecht zum Toroidalfeld B_{y0} und der Stromrichtung wirkenden Kraft beträgt: $F = I \cdot B_{y0} \cdot b$, bzw: $F = s \cdot b \cdot B_{y0} \cdot B_v / \mu_0$. Das zugehörige Moment beträgt: $M = a/2 * 2F = a \cdot F$

Explosion prevention document of the MGI system

This appendix contains the explosion prevention document for the ASDEX Upgrade in-vessel MGI system. This includes the primary document with descriptions and calculations, as well as the scheme of the system with names of all components.

Explosion prevention document
Massive Gas Injection (MGI) ASEDEX Upgrade

1. Risk assessment:

During evacuation of the MGI system, an explosive mixture can arise in the gas handling system. Additionally, an explosive mixture can occur in the spring-driven MGI valves.

2. Procedural issue:

The MGI system is used to abruptly inject gases (H_2, D_2, He, Ne, Ar) or mixtures of these gases into ASDEX Upgrade. For this purpose, four special MGI valves are used which are mounted in the vacuum vessel of ASDEX Upgrade: Two spring-driven valves in Se6 LFS and Se4 HFS, each with an internal gas reservoir of 128 cm³, a piezo-driven valve Se13 HFS with 42 cm³ and a spring-driven valve Se13 with 80 cm³. The valves can be filled separately with two gas handling stations. The valves can either be vented into the vacuum vessel or over the gas handling stations. The gas bottles (20 MPa, 0.01 m³), the respective pressure reducers, the manual valves HV1 and HV2 and the pneumatic valve PV1 are located at the east wall outside the torus hall in a lockable cell. The gas handling stations are located in the torus hall in Se10 and Se13. The MGI valves are mounted inside the torus. This document focuses on operation with H_2/D_2 only.

2.1. Technical procedure:

In the idle state, the valves are evacuated and at the pressure of the torus (10^{-5} Pa) and the gas handling stations are evacuated (~100 Pa). If one or more MGI valves are to be filled, the manual valves HV1 and HV2 are opened, as well as the manual valves to the MGI valves (HV1 – HV9). The spring-driven valves are closed by pressurized air. Therefore, the valve system (BVI) is switched and PV27 is opened (for MGI Se13) or PV14 is opened, as well as the respective pneumatic valves (PV15, PV16) (for MGI Se4, Se6). The piezoelectric stack actuators of the spring-driven valves are charged and the pressurized air is vented (switch BVI for MGI Se13) (close PV14 and open PV18 for MGI Se4, Se6). To let the mitigation gas into the MGI valves, valve PV1 is opened. Afterwards, PV22 and/or PV23 are opened (for MGI Se13) or PV2 and/or PV3 are opened (for MGI Se4, Se6, Se13). The mixing volumes MIXVOL1 and MIXVOL2 are filled. When the desired pressure is reached (max. 1 MPa H_2/D_2), the pneumatic valves PV1, PV2, PV3, PV22, PV23 are closed. The gas is let into the MGI valves by opening the respective pneumatic valves (PV22 for MGI Se13) (PV4 … PV9 for MGI Se4, Se6, Se13). When the MGI valves are filled, the pneumatic valves are closed again. Triggering the valves leads to evacuation into the torus. The gas handling stations are evacuated. The MGI valves can also be pumped over the gas handling stations. When flammable gases are used, the pneumatic valves (PV26 for Se13) (PV13 for Se10) to the hydrogen pump (H-PMP) are opened. Evacuation of noble gases is done by other pumps (PMP1, PMP2). Therefore, the bypass lines are opened (PV24 for Se13) (PV11 for Se10) to vent the gas and afterwards the residual gas is pumped (PV23 for Se13) (PV10 for Se10).

2.2. Cell:

The cell contains the gas bottles in which the gases are stored and the pressure reducers which connect the gas bottles to the system, as well as the ball valves and the pneumatic valve to cut off the gas lines. The components are connected by stainless steel tubes 6x1 mm and full-metal connectors (Swagelok). The cell is located outside torus hall. The gas bottles contain 0.01 m³ at 20 MPa. The pressure reducers allow a back pressure of 1 MPa for flammable gases and 10 MPa for noble gases.

2.3. Gas handling stations:

The gas handling stations for the MGI valve in Se13 LFS is located in the torus hall Se13 and serves as supplier for pressurized air (0.6 MPa) and mitigation gas. The lines for pressurized air and gas are composed of stainless steel tubes 6x1 mm and full-metal connectors (Swagelok). Both lines are completely separated.

The gas handling station for the MGI valves Se4, Se6, Se13 is located in the torus hall Se10 on top of the torus and serves as supplier for pressurized air (1.7 MPa) and mitigation gas. The lines for pressurized air and gas are composed of stainless steel tubes 6x1 mm and full-metal connectors (Swagelok). Both lines are completely separated.

2.4. Pumps:

The gas handling station and the MGI valve Se13 can either be evacuated using the hydrogen pump or a membrane pump. If flammable gases are used, the hydrogen pump must be used. For pure noble gases, the membrane pump is used.

The gas handling station Se10 and the respective MGI valves can either be evacuated using the hydrogen pump or a sliding vane rotary vacuum pump. If flammable gases are used, the hydrogen pump must be used. For pure noble gases, the sliding vane rotary vacuum pump is used.

- Hydrogen pump: Leybold DV 650 (ATEX Kategorie 2l)
- Membrane pump: Vacuubrand MD4CEX (ATEX Kategorie 3G)
- Sliding vane rotary vacuum pump: Leybold S16B

2.5. MGI valves:

Die spring-driven MGI valves have an internal gas reservoir of 128 cm^3 or 80 cm^3. These volumes are normally opened to the torus. Pressurized air is let into a sealed volume in the valves. This pushes the valve stem forward, compressing the disc springs and closing the gas reservoir. Piezoelectric stack actuators clamp the stem and the pressurized air is vented. The mitigation gas is let into the gas reservoir (max. 1 MPa H_2/D_2). When the valves are triggered, the piezoelectric stack actuators release the stem and the disc springs open the reservoir. The valves are made from stainless steel with full-metal connectors (VCR, gold wire) except one Viton seal between valve plate and nozzle.

The piezo-driven MGI valve has an internal gas reservoir of 42 cm^3 which is closed against the torus vacuum in its idle state. The mitigation gas is let into the reservoir (max. 1 MPa H_2/D_2). When the valve is triggered, the piezoelectric stack actuators are charged, which pull back the valve plate and open the gas reservoir. The valve is made from stainless steel and full metal connectors (VCR, copper) except one Viton seal between valve plate and nozzle.

3. Measures for explosion prevention:

3.1. Cell:

The formation of a dangerous explosive mixture is prevented by following circumstances and measures:

- Full-metal connectors, regular checks of technical tightness by pressure loss tests
- Change of gas bottles: Venting in open space.
- Storage in open space

3.2. Gas handling stations:

The formation of a dangerous explosive mixture is prevented by following circumstances and measures:

- Full-metal connectors, regular checks of technical tightness by pressure loss tests
- Complete separation of pressurized air lines and gas lines

3.3. Pumps

The use of separated pumping lines for noble gases and hydrogen/hydrogen mixtures guaranties, that explosive mixtures can only occur in pumps which are suited for such gases. When pure noble gas is used, the sliding vane rotary vacuum pump and the membrane pump are used to evacuate the gas handling stations. For hydrogen/hydrogen mixtures, the hydrogen pump is used. The bypass line and the pumping line are closed by pneumatic valves. Only one line can be opened (Locked in the SIMATIC). This prevents, that the pumping line to the membrane/ sliding vane rotary vacuum pump is connected to the pumping line to the hydrogen pump. This is also the case for the bypass lines.

3.4. Case of accident:

3.4.1 Outage of the vacuum pumps

In the case of outage of the vacuum pumps by damage or blackout, the gases remain in the gas lines of the gas handling system. The concentration of the H_2/D_2 is close to 100 % and therefore above the flammable concentration of (77 % for H_2 und 79.6 % for D_2). Air could enter into the pumping lines through the pumps. For the membrane/ sliding vane rotary vacuum pump, the pumping lines are filled with noble gas and sealed off by pneumatic valves which are normally closed. Should these valves jam in the opened position while the pumps are not operating, an explosive mixture can occur. The hydrogen pump is secured for this case.

3.4.2 Breach

Should a breach of the full-metal connectors or the stainless steel tubes occur in the evacuated state, the complete gas handling station and the MGI valves could be flooded with air in the worst case. The pressure in the evacuated state is about 100 Pa hydrogen. The volumes are:

- Mixing volume gas handling station 1: 500 cm^3
- Mixing volume gas handling station 2: 500 cm^3
- Volumes in the lines, valves and gauges of gas handling station Se10: 250 cm^3
- Volumes in the lines, valves and gauges of gas handling station Se13: 190 cm^3
- Volume in the gas line to MGI valve Se6 LFS: 1900 cm^3
- Volume in the gas line to MGI valve Se4 HFS: 1500 cm^3
- Volume in the gas line to MGI valve Se13 HFS: 1500 cm^3
- Volume in the gas line to MGI valve Se13 LFS: 750 cm^3
- Gas reservoir MGI valve Se6 LFS: 128 cm^3
- Gas reservoir MGI valve Se4 HFS: 128 cm^3
- Gas reservoir MGI valve Se13 HFS: 42 cm^3
- Gas reservoir MGI valve Se13 LFS: 80 cm^3
- Total volume: 7468 cm^3

With this, the equilibrium concentration is ((100 Pa * 0.007468 m^3) / (100000 Pa * 0.007468 m^3)) 0.1 % which is far below the explosive limit for H_2 (4 %) and D_2 (6.7 %). However, a pressure range in which an explosive concentration could be reached in case of a breach is crossed while evacuating. This range is crossed within seconds.

When the gas handling stations and the valves are filled with hydrogen, a pressure of 1 MPa can be present in the entire system. A breach outside the torus would cause the hydrogen to vent into the torus hall. If the entire inventory flows into the torus hall (assumed volume 4000 m^3), the resulting concentration would be ((1 MPa * 0.007468 m^3) / (0.1 MPa * 4000 m^3)) 0.002 % which is far below the flammable concentration. A breach within the torus (volume 13 m^3) while it is flooded with air would cause a concentration of ((1 MPa * 0.007468 m^3) / (0.1 MPa * 13 m^3)) 0.58 %. This is also below the flammable concentration.

A breach of the gold wire seal in one of the spring-driven valves would cause a flow of H_2/D_2 into the piezo-chamber which is filled with air. In the worst case a flammable equilibrium concentration is formed in the piezo-chamber and the smallest gas filled volume.

- Volume of the piezo-chamber spring-driven valve (new): 34 cm^3
- Volume of the piezo-chamber spring-driven valve (old): 45 cm^3
- Gas line Se6 LFS + gas reservoir: 910 cm^3
- Gas line Se4 HFS + gas reservoir: 760 cm^3
- Gas line Se13 LFS + gas reservoir: 830 cm^3

Flammable concentrations of the mixtures are reached at following H_2/D_2 pressures:

- MGI valve Se6 LFS und H_2: (0,77 * 34 cm^3 * 0.1 MPa)/(910 cm^3 * (1 – 0,77)) = 12.5 kPa
- MGI valve Se6 LFS und D_2: (0,796 * 34 cm^3 * 0.1 MPa)/(910 cm^3 * (1 – 0,796)) = 14.6 kPa
- MGI valve Se4 HFS und H_2: (0,77 * 34 cm^3 * 0.1 MPa)/(760 cm^3 * (1 – 0,77)) = 15 kPa
- MGI valve Se4 HFS und D_2: (0,796 * 34 cm^3 * 0.1 MPa)/(760 cm^3 * (1 – 0,796)) = 17.5 kPa
- MGI valve Se13 LFS und H_2: (0,77 * 45 cm^3 * 0.1 MPa)/(830 cm^3 * (1 – 0,77)) = 18.2 kPa
- MGI valve Se13 LFS und D_2: (0,796 * 45 cm^3 * 0.1 MPa)/(830 cm^3 * (1 – 0,796)) = 21.2 kPa

Above these critical pressures, the concentrations are above the flammable concentrations. It has to be noted, that a slow leak, which would allow a slow flooding, could create an explosive mixture even when the H_2/D_2 pressure is above the critical pressure. However, a defective gold wire seal would lead to the evacuation of the piezo-chamber into the torus. This would prevent the formation of an explosive mixture.

4. Classification into zones (acc. Anhang 3 BetrSichV):

a)	Cell:	No expl. zone (-> Below the flammable concentration)
b)	Gas handling stations:	No expl. zone (->Below/above the flammable concentration)
c)	Pumps:	Zone 2 (for membrane/sliding vane rotary vacuum pump)
d)	Hydrogen pump:	See explosion prevention document hydrogen pump
e)	MGI valves:	Zone 2

Definition Zone 2:

Zone, in which a dangerous explosive atmosphere from a mixture of air and flammable gases, vapors or fumes does usually not occur or only during short times.

5. Measures (acc. Anhang 4 BetrSichV)

5.1. Organizational measures:

- Instruction of workers by workspace specific instructions
- Written instructions in form of directives

5.2. Technical measures:

5.2.1 Pumps at the gas handling stations:

Feedback sensors monitor whether the membrane/sliding vane rotary vacuum pump are operating and the pressures in the pumping lines are measured. The signals of the sensors and the vacuum pressures are transferred to the SIMATIC. By an increasing pressure in the pumping lines, a defect of the pneumatic valves (PV10, PV12, PV23, PV25) can be detected. This would mean air and hydrogen are present in the pumping lines, which would then be evacuated over the hydrogen pump.

5.2.2 Pneumatic valves in the pumping lines:

Passive position detectors monitor the position of the pneumatic valves. The signals of the position detectors are transferred to the SIMATIC. This is to monitor especially the valves PV10, PV11, PV23, PV24 as they are the interface between the hydrogen zone and the inert pumping system. A defect can be determined and the system can be evacuated over the hydrogen pump.

6. Attachements:

- Scheme of the system
- Draft of a directive
- Detailed description of the MGI valves
- Technical description of the gases
- Detailed description of each component in the gas handling stations

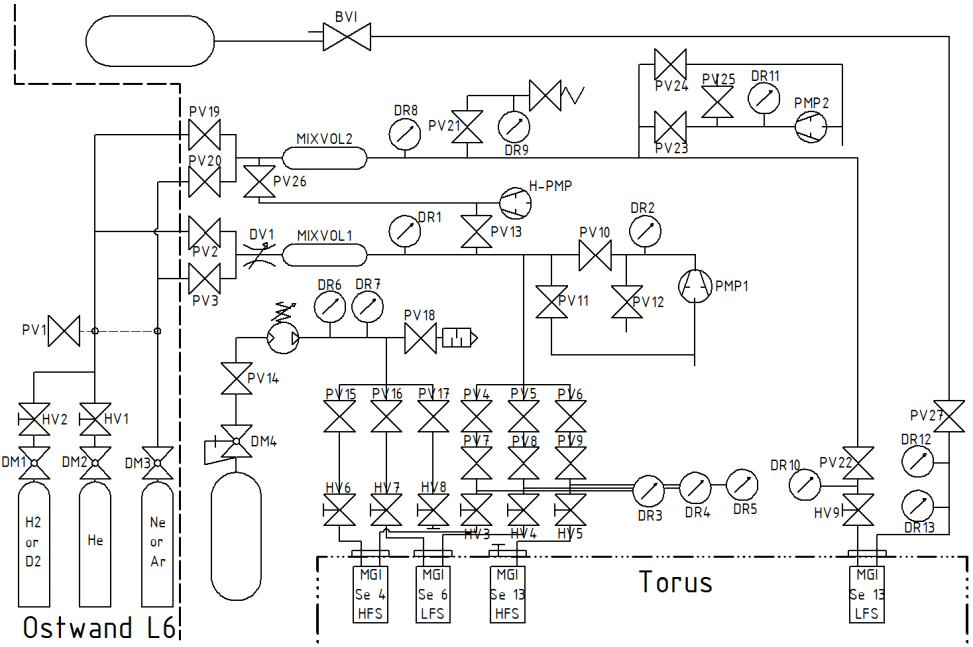

Scheme of the MGI system (PV = Pneumatic valve, DM = Pressure reducer, HV = Manual valve, MIXVOL = Mixing volume, DV = pressure reduction valve, DR = Pressure gauge, BVI = Bürkert valve assembly, PMP = Pump)

Bez.	Bez. SIMATIC	Bauteil
PV1	VGASV	Bellow sealed valve w. pneum. actuator, Connector: 1/4" VCR (SS-HBV51-CM)
PV2	2VMIX1	Bellow sealed valve w. pneum. actuator, Connector: 1/4" VCR (SS-HBV51-CM)
PV3	2VMIX2	Bellow sealed valve w. pneum. actuator, Connector: 1/4" VCR (SS-HBV51-CM)
PV4	2VSVV1	Bellow sealed valve w. pneum. actuator, Connector: 1/4" VCR (SS-HBV51-CM)
PV5	2VSVV2	Bellow sealed valve w. pneum. actuator, Connector: 1/4" VCR (SS-HBV51-CM)
PV6	2VSVV3	Bellow sealed valve w. pneum. actuator, Connector: 1/4" VCR (SS-HBV51-CM)
PV7	2VGASE	Bellow sealed valve w. pneum. actuator, Connector: 6mm tube fitting (SS-HBS6MM-C)
PV8	3VGASE	Bellow sealed valve w. pneum. actuator, Connector: 6mm tube fitting (SS-HBS6MM-C)
PV9	4VGASE	Bellow sealed valve w. pneum. actuator, Connector: 6mm tube fitting (SS-HBS6MM-C)
PV10	2VPMP1	Bellow sealed valve w. pneum. actuator, Connector: 1/4" VCR (SS-HBV51-CM)
PV11	2VBYPA	Bellow sealed valve w. pneum. actuator, Connector: 1/4" VCR (SS-HBV51-CM)
PV12	2VBEFL	Bellow sealed valve w. pneum. actuator, Connector: 1/4" VCR (SS-HBV51-CM)
PV13	MGI5	Membrane valve w. pneum. actuator, Connector: 1/2" VCR (Gemü 650)
PV14	2VDRAB	Bellow sealed valve w. pneum. actuator, Connector: 1/4" VCR (SS-HBV51-CM)
PV15	2VSIC2	Bellow sealed valve w. pneum. actuator, Connector: 1/4" VCR (SS-HBV51-CM)
PV16	2VSIC3	Bellow sealed valve w. pneum. actuator, Connector: 1/4" VCR (SS-HBV51-CM)
PV17	2VSIC4	Bellow sealed valve w. pneum. actuator, Connector: 1/4" VCR (SS-HBV51-CM)
PV18	2VENTL	Bellow sealed valve w. pneum. actuator, Connector: 1/4" VCR (SS-HBV51-CM)
PV19	VMIX1	Bellow sealed valve w. pneum. actuator, Connector: 6mm tube fitting (SS-HBS6MM-C)
PV20	VMIX2	Bellow sealed valve w. pneum. actuator, Connector: 6mm tube fitting (SS-HBS6MM-C)
PV21	----------	Bellow sealed valve w. pneum. actuator, Connector: 6mm tube fitting (SS-HBS6MM-C)
PV22	VGASE	Bellow sealed valve w. pneum. actuator, Connector: 6mm tube fitting (SS-HBS6MM-C)
PV23	VPUMP	Bellow sealed valve w. pneum. actuator, Connector: 6mm tube fitting (SS-HBS6MM-C)
PV24	VBYPA	Bellow sealed valve w. pneum. actuator, Connector: 6mm tube fitting (SS-HBS6MM-C)
PV25	VBEFL	Bellow sealed valve w. pneum. actuator, Connector: 6mm tube fitting (SS-HBS6MM-C)
PV26	MGI1	Membrane valve w. pneum. actuator, Connector: 1/2" VCR (Gemü 650)

PV27	VSICH	Bellow sealed valve w. pneum. actuator, Connector: 6mm tube fitting (SS-HBS6MM-C)
DM1	----------	Pressure reducer, DruVa FMD300-18, max. front 200 bar, max. back 10 bar
DM2	----------	Pressure reducer, Air Liquide BM350-1, max. front 300 bar, max. back 100 bar
DM3	----------	Pressure reducer, Air Liquide BM350-1, max. front 300 bar, max. back 100 bar
DM4	----------	Pressure reducer, Transair 6700 00 13 (max. 8 bar)
HV1	----------	Ball valve, Connector: 6mm tube fitting (SS-43GS6MM)
HV2	----------	Ball valve, Connector: 6mm tube fitting (SS-43GS6MM)
HV3	----------	Ball valve, Connector: 6mm tube fitting (SS-43GS6MM)
HV4	----------	Ball valve, Connector: 6mm tube fitting (SS-43GS6MM)
HV5	----------	Ball valve, Connector: 6mm tube fitting (SS-43GS6MM)
HV6	----------	Ball valve, Connector: 6mm tube fitting (SS-43GS6MM)
HV7	----------	Ball valve, Connector: 6mm tube fitting (SS-43GS6MM)
HV8	----------	Ball valve, Connector: 6mm tube fitting (SS-43GS6MM)
HV9	----------	Ball valve, Connector: 6mm tube fitting (SS-43GS6MM)
DV1	----------	Pressure reduction valve, series M, 1/4" VCR AG (SS-MGVR4-MH)
MIXVOL1	----------	Sample cylinder 500 cm^3, ¼ Zoll NPT thread, 124 bar (316L-HDF4-500)
MIXVOL2	----------	Sample cylinder 500 cm^3, ¼ Zoll NPT thread, 124 bar (316L-HDF4-500)
DR1	2DRUMIX	Piezo resistive pressure gauge, Keller PAA-21Y 70bar
DR2	PP2	Compact Pirani gauge, Pfeiffer Vacuum PCR 260
DR3	3DRVENT	Piezo resistive pressure gauge, Keller PAA-21Y 70bar
DR4	2DRVENT	Piezo resistive pressure gauge, Keller PAA-21Y 70bar
DR5	4DRVENT	Piezo resistive pressure gauge, Keller PAA-21Y 70bar
DR6	----------	Miniature Pressure Gauge 0-25bar Connector: 1/4" NPT (PGI-50M-BG25-LAOX)
DR7	DRVSCHLIESS	Piezo resistive pressure gauge, Keller PAA-21Y 20bar
DR8	DRUMIX	Piezo resistive pressure gauge, Keller PAA-21Y 70bar
DR9	----------	Piezo resistive pressure gauge, Keller PAA-21Y 20bar
DR10	DRVENT	Piezo resistive pressure gauge, Keller PAA-21Y 50bar
DR11	DRVOVA	Compact Pirani gauge, Pfeiffer Vacuum PCR 260
DR12	----------	Pressure gauge, Kuhnke 00.08.00.087.02 (max. 10 bar)
DR13	DRVENT	Digital pressure gauge, Keller Piccolo 80259 0-150 bar
BVI	PVANH	Bürkert valve system for 6 bar pressurized air
PMP1	VPMP2	Sliding vane rotary vacuum pump, Leybold Trivac S16B (only nobel gas)
PMP2	VPMP1	Membrane pump, Vacuubrand MD4CEX (all gases)
H-PMP		Hydrogen pump, Leybold DV 65

Signal plan for the new MGI valves

This appendix contains the signal plan for the new MGI valves.

New MGI control system